Silk fibroin nanoparticles: *in vitro* performance of a putative anticancer nanomedicine.

John D. Totten, BSc (hons)

Strathclyde Institute of Pharmacy and Biomedical Sciences

University of Strathclyde

Glasgow, UK

A thesis submitted in fulfilment of the requirements for the degree of Doctor of Philosophy.

April 2019

Declaration

This thesis is the result of the author's original research. It has been composed by the author and has not been previously submitted for examination which has led to the award of a degree.

Signed:

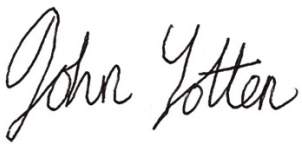

Date: 23/04/2019

Abstract

Despite the advantages of nanoparticle-based carriers for anticancer drug delivery, their translation into the clinic has been limited by factors including: (i) poor endocytic uptake and intracellular routing, (ii) macrophage clearance and (iii) a disregard of the tumour microenvironment governing nanoparticle uptake. As a result, there is a continued demand to explore the performance of polymer-based nanoparticles. The principle hypothesis of this thesis is that silk fibroin nanoparticles can be used as anticancer nanomedicines. To validate this, the mechanisms governing drug release from silk fibroin nanoparticles are explored in Chapter 3. Next, the immunogenicity of silk fibroin nanoparticles towards macrophages is assessed (Chapter 4). Finally, Chapter 5 investigates the endocytosis of silk fibroin nanoparticles in response to the cell cycle and culture substrate mechanics.

This thesis provided the first experimental proof of lysosomotropic anticancer drug delivery from silk fibroin nanoparticles in single human breast cancer cells (Totten *et al*. 2017. J. Drug Target. 25, pp 865–872) (Chapter 3). Drug loaded silk fibroin nanoparticles were endocytosed by MCF-7 cells and a combination of the acidic lysosomal pH and enzymatic degradation facilitated drug release and subsequent nuclear translocation of the payload within 5 hours of dosing. Next, nanoparticle-macrophage interactions were studied (Chapter 4). Silk fibroin nanoparticles exerted similar immunogenicity to silica and poly(lactic-*co*-glycolic acid) nanoparticles (Saborano, Wongpinyochit, Totten, Johnston, Seib and Duarte. 2017. Adv. Healthc. Mater. 6, 1601240). This indicated that silk fibroin nanoparticles can compete with leading healthcare materials in pre-clinical and clinical use. Further assessment into immunomodulatory potential of silk fibroin nanoparticles revealed that they drive macrophage polarisation towards a pro-inflammatory M1-like state (Totten *et al*. 2019. ACS Appl. Mater. Interfaces. *in press*). This effect could be fine-tuned with surface modification (i.e. PEGylation). This observation is important because silk fibroin nanoparticles could act both as carriers for chemotherapeutics and as synergistic attenuators of tumour-associated macrophages in the tumour site. Finally, advanced analysis of silk fibroin nanoparticle endocytosis was conducted (Chapter 5) by assessing intracellular trafficking in a time-dependent manner. Endocytosis of silk fibroin nanoparticles by breast cancer (MCF-7) cells was influenced by cell cycle progression, but not substrate mechanics. However, substrate mechanics were found to modulate the endocytic behaviour of healthy human (MCF-10A) breast epithelial cells. This relationship warrants further investigation with regard to the cellular response of nanomedicines.

Overall, this thesis accomplished *in vitro* analysis of silk fibroin nanoparticle drug delivery performance, macrophage interactions and endocytic uptake. These findings indicate that silk fibroin nanoparticles are emerging as an interesting biopolymer for anticancer applications. Work presented in this thesis provides a foundation to now move to pre-clinical *in vivo* studies.

Research Outputs

Publications:

1. **Totten, J. D.**, Wongpinyochit, T. & Seib, F. P. Silk nanoparticles: proof of lysosomotropic anticancer drug delivery at single-cell resolution. *J. Drug Target.* **25**, 865–872 (2017).
2. Saborano, R., Wongpinyochit, T., **Totten, J.D.**, Johnston, B.F., Seib F.P. & Duarte I.F. Metabolic Reprogramming of Macrophages Exposed to Silk, Poly(lactic-co-glycolic acid), and Silica Nanoparticles. *Adv. Healthc. Mater.* **6**, 1601240 (2017).
3. **Totten, J. D.**, Wongpinyochit, T., Carrola, J., Duarte, I. F. & Seib, F. P. PEGylation-Dependent Metabolic Rewiring of Macrophages with Silk Fibroin Nanoparticles. *ACS Appl. Mater. Interfaces* (2019). *In press.*
4. Wongpinyochit, T., **Totten, J. D.**, Johnston, B. F. & Seib, F. P. Microfluidic-assisted silk nanoparticle tuning. *Nanoscale Adv.* **1**, 873–883 (2019).

Conference contributions

Abstracts for conference contributions are included in Appendices A – C.

A. **Totten, J. D.**, Wongpinyochit, T., Johnston, B.F., & Seib, F. P. Silk nanoparticles are endocytosed by live breast cancer cells and facilitate lysosomotropic delivery of an anticancer drug. UKICRS symposium 2017. Glasgow, U.K.
Oral presentation.

B. **Totten J. D.**, Saborano, R., Wongpinyochit, T., Duarte I.F. & Seib F.P. Silk nanoparticles: lysosomotropic drug delivery and metabolic reprogramming at the tumour microenvironment.12th International Symposium on Polymer Therapeutics. Valencia, Spain.
Poster presentation.

C. **Totten J.D.**, Wongpinyochit, T., Carrola J., Duarte I.F. & Seib F.P. Attenuation of macrophage activation state with silk nanoparticles. Bioinspired nanomaterials. RSC Chemical Nanoscience and Nanotechnology Interest Group Early Career Researcher Meeting. Glasgow, U.K.
Poster presentation.

Acknowledgements

I would like to thank my supervisor, Dr. Philipp Seib, for his unwavering support and encouragement throughout the PhD project. My second supervisor, Dr. Blair Johnston was also very supportive of my endeavours and I am grateful for his assistance. As well as my supervisors, I would like to thank Dr. Owain Millington for training and support in the early days of flow cytometry, and Mr Graeme MacKenzie for training in confocal microscopy. In addition, I would like to thank Dr. Iola Duarte for her invaluable support and input as a collaborator on two manuscript submissions.

Many thanks as well to my colleagues in the Seib lab. Particularly to Tar, Osama, Frankie, and Natalie, who welcomed me into a new research environment and provided a wealth of experience when starting out in the PhD. Thanks to Georg, Jana, Maria and Refaya, who allowed me to share my own knowledge at the later stages of the PhD, and to Gemma and Jaa, who I hope to work with again on future projects.

I would also like to thank Prof. Arwyn Jones for devoting time and research resources during my attempts to inhibit endocytosis. His postdoctoral research associates (Dr. Jennifer Wymant and Dr Edward Sayers) were invaluable during my trip to Cardiff University and I want to thank them for their patience and support during this part of the project.

To Scott, Ivan, Natalie, Eleanor, Rachel, Lauren, Abdullah, Graeme, Abiy, David and Taufiq: thank you for the friendship and support during the good times and the struggles. Finally, I would like to thank my family and fiancé for their unwavering support and guidance over the years.

Table of Contents

Abbreviations

AF488	Alexa Fluor 488®
APC	Allophycocyanin
ARF-6	ADP-ribosylation factor-6
CDC-42	Cell division control protein 42
DMEM	Dulbecco's Modified Eagle Medium
ECM	Extracellular matrix
EMA	European medicines agency
EPR	Enhanced permeability and retention
FDA	Food and drug administration
FITC	DMEM - Dulbecco's Modified Eagle Medium
FSC-A	Forward scatter – area
HBSS	Hank’s balanced salt solution
LNP	Latex nanoparticle
PA	Poly(acrylamide)
PBS	Phosphate buffered saline
PBS-T	Phosphate buffered saline-tween
PEG	Poly(ethylene) glycol
PEG-SNP	PEGylated silk fibroin nanoparticle
PLA	Polylactic acid
PLGA	Poly lactic-co-glycolic acid
SEM	Scanning electron microscopy
SNP	silk fibroin nanoparticle
SSC-A	Side scatter – area
TNFα	Tumour necrosis factor alpha

List of Figures

Chapter 1: Introduction

This chapter introduces the topic of nanomedicine by providing an overview of the history of the field and a selection of nanomedicines that can be engineered. The bottlenecks of nanomedicine engineering are highlighted, and silk is suggested as a novel biomaterial to overcome biocompatibility challenges in the field. As anticancer nanomedicines depend on intracellular trafficking to deliver drugs, the process of endocytosis is defined and explained within the context of drug delivery. Barriers to anticancer drug delivery with nanomedicines are also examined and adapting to these barriers by exploring particle design is suggested as a method to improve tumour targeting with nanomedicines. Finally, the overall hypothesis of the thesis is introduced along with accompanying aims and objectives.

1.1. Nanomedicine

The term "nanomedicine" was coined in the early 2000s to consolidate research in nano-sized therapeutics under a new interdisciplinary field.[1] The objectives of this field are: the creation and application of nanotechnology to improve medical diagnostics and therapeutic treatments.[2] Whilst the terminology is fairly recent, research into nano-sized therapeutics has been underway since the early 1970s and several nanomedicines are clinically approved as imaging agents (e.g. superparamagnetic iron oxide nanoparticles, Lymphoseek) and drug delivery systems for treatment of solid tumours (e.g. Doxil,[3] Abraxane[4]), leukaemias (e.g. Oncaspar[5]), type II diabetes (e.g. Welchol[6]), electrolyte imbalance (e.g. Renagel[7], Veltassa[8]) and multiple sclerosis (e.g. Copaxone[9]).[10]

Many first generation nanomedicines were designed as anticancer drug delivery systems and they persist today as second line therapies in the treatment of breast, lung, liver, pancreatic and ovarian cancers.[11] Anticancer nanomedicines exert superior tumour targeting when compared to conventional drugs by using the process of enhanced permeability and retention (EPR).[12,13] This occurs as a result of tumour angiogenesis, which produces a leaky vasculature that nanomedicines exploit to gain access to the tumour site. The "enhanced permeability" of nanomedicines is coupled to poor tumour lymphatic drainage and this enables nanomedicine accumulation within the tumour site.[12,13] EPR forms the basis for development of many drug delivery systems with passive tumour targeting capabilities.[14–16] Nanomedicines are also engineered to overcome biological barriers and deliver therapeutic payloads to specific organs, cells or sub-cellular organelles.[17] The different levels of delivery are termed

first, second and third order targeting, respectively; and correct biological routing is essential for a nanomedicine to exert controlled drug release because the carrier is often designed to respond to microenvironmental cues (e.g. pH, enzymes).

1.1.1. Types of nanomedicine

Many therapeutic technologies exist within the nanoscale and are described as a nanomedicines. However, they often fall into one of three well-defined classes of delivery systems; namely liposomes, polymer therapeutics and nanoparticles.[10]

Liposomes are manufactured from phospholipids and can range in size from the nano- to micro- scale depending on the manufacturing method.[18] Liposomes were first discovered in 1965[19] and their structure consists of a hydrophobic lipid bilayer with a hydrophilic core. They are particularly versatile drug delivery systems because hydrophilic or hydrophobic drugs can be encapsulated within the appropriate liposomal structural compartment.[20,21] To date, liposomes are the most successful class of nanomedicine for anticancer delivery and have been clinically approved for human use since the 1990s.[3,22]

Polymer therapeutics are a diverse family of nanomedicines. One of the earliest members of this class have been polymer-drug conjugates based on the design of Helmut Ringsdorf.[23,24] In this model, therapeutic payloads are covalently linked to a water-soluble polymer to improve solubility and stability and reduce the immunogenicity in the circulation. Often, a labile linkage between the polymer and drug is employed to ensure that the payload is released at the target site in response to

environmental changes (e.g. pH or activating enzymes).[25] The polymer therapeutic family has been categorised into five distinct classes consisting: (i) polymeric drugs, (ii) polymer-drug conjugates, (iii) polymer-protein conjugates, (iv) polymeric micelles and (v) polymer-aptamers.[24] Of these classes, polymer-protein conjugates have had the most clinical success, with PEGylated cytokines being used routinely in the clinic for the treatment of immunological disorders such as Crohn's disease (e.g. Cimzia) and hepatitis B and C (e.g. Pegintron, Pegasys).[26] Less success has been noted in the translation of polymer drug conjugates, with only one polymer-based nanomedicine (styrene maleic anhydride-neocarzinostatin) approved for treatment of liver cancer in Japan.[27]

Research in the clinical use of nanoparticles dates back to the 1950s. However, it was not until 2005 that a nanoparticle was clinically approved as a drug delivery system.[28] Abraxane is a nanoparticle formulation of albumin-bound paclitaxel and is currently Food and Drug Administration (FDA) and European Medicines Agency (EMA) approved as a second line therapy for the treatment of breast tumours.[28] Nanoparticles are defined as 1 – 1,000 nm sized particles and can be manufactured from one or more materials. Importantly, this can include materials such as lipids or polymers. However, nanoparticles are distinct from liposomes and polymer-drug conjugates as they lack a lipid bilayer and are not manufactured according to the traditional Ringsdorf model (i.e. a water soluble polymer).[10] Nanoparticles are appealing drug delivery systems because they integrate many characteristics of liposomes and polymer therapeutics whilst retaining their own unique properties.[17] For example, like liposomes, the size of nanoparticles can be tailored to the target disease.[17] Nanoparticles can also transport hydrophilic, hydrophobic or multiple drug payloads with a range of physiochemical

properties because dedicated methods are available to achieve drug loading[29] and they can be covalently linked to water-soluble polymers such as polyethylene glycol (PEG) to improve particle stability and reduce immunogenicity during circulation.[30] In addition to their readily tuneable size, drug loading and surface characteristics, nanoparticles can be produced with different shapes (spheres, rods, cylinders, discs etc.) and can be used to modify their circulatory performance, biodistribution and cellular interactions.[17,31] Nanoparticles can also be manufactured from a range of different materials including synthetic polymers (e.g. poly(lactic-co-glycolic acid (PLGA), polycaprolactone, polylysine),[32–34] inorganic elements (e.g. silica),[35] metals (e.g. silver, gold, iron)[36–38] and biopolymers (albumin, chitosan, silk).[4,39,40] Many synthetic and inorganic nanomaterials are at various stages of clinical trials. However, a combination of the clinical success of Abraxane (essentially a protein biopolymer) and increasing concerns about the toxicity of non-biodegradable nanomaterials has catalysed an increase in demand for nanomedicines with inherent biocompatibility and biodegradability. This thesis addresses this demand by proposing the reverse engineering and nanoprecipitation of silk to yield a novel nanomaterial for potential anticancer drug delivery. Therefore, there is the need to have a background in silk to appreciate the scope of this thesis.

1.2. Silk

Silks are structural biopolymers that can be spun by various animals (e.g. spiders, silkworms, bees, ants) for use outside the body.[41] Silk has been valued by humans since ancient times as high-value luxury fabrics. In particular, silkworm silk has been subjected to human intervention due to selective breeding of the *Bombyx mori* silkworm. In addition to silk's status as a garment material, silkworm silk has a unique track record of medical use in humans dating back to the times of the ancient Romans. Silk is widely regarded as biocompatible in humans.[42] The medical applications of silkworm silk persist today in a clinical setting with the routine use of FDA/EMA approved silk surgical sutures for intricate ophthalmic surgeries due to their ease of use and production of flat knots on tissue surface.[41,43] In addition, silk surgical meshes are approved for use in soft tissue support and repair. These meshes demonstrated improved long-term biodegradability and bioreplaceability when compared to synthetic materials.[44,45] Most recently (November 2018), the FDA approved silk hydrogels for vocal fold paralysis repair.[46] The clinical applications of silk are expanding rapidly at a time when demand for natural biocompatible polymers is growing.[47,48] This demand is particularly high in the field of nanomedicine[49] and there is an interest in the structure-function relationships of silk, the biological performance of silk and the methods available to process silk into particles due to their potential for use as healthcare technologies.

1.2.1. Silk structure

Commercial silk is almost exclusively derived from the cocoon of the domestic silkworm *Bombyx mori* as they are abundantly produced and readily available due to a well-established sericulture and supply chain.[42] *Bombyx mori* silk fibres consist of a semi-crystalline silk fibroin core that is surrounded by a gumming agent called sericin that enables the silk fibres to stick together.[50] Silk fibroin is the material of interest when exploring silk for healthcare technologies because its unique chemical structure confers desirable mechanical properties and whilst lacking classical markers for immunogenicity or adjuvanticity.[42] Silk fibroin is a large macromolecule consisting of a light (approximately 26 kDa) and heavy (approximately 391 kDa) chain that is linked at the C-terminus by a single disulphide bond.[51] The silk fibroin light chain is made up of non-repeating amino acid sequences which are amorphous in structure, whilst the silk fibroin heavy chain is more complex, consisting of 12 hydrophobic blocks made up of repetitive glycine-rich amino acid sequences that are interspaced with 11 hydrophilic domains (Figure 1.1 A).[42] The hydrophobic blocks account for 94% of the overall heavy chain and influence the structure of silk fibroin depending on the combination of amino acid repeats in the primary structure. For example, glycine (G), alanine (A) and serine (S) rich repeating units such as the GAGAGS sequence contribute to the crystalline regions of the protein found at the beginning of each block, whilst glycine, tyrosine (Y) and valine (V) rich sequences (e.g. GAGAGY, GAGAGV, and GAGAGVGY) provide semi-crystalline regions.[51,52] The silk fibroin heavy chain is capped at the C- and N- terminus by non-repeating amino acid residues, which make the terminal ends of the heavy chain highly hydrophilic.[53] The primary structures of the silk fibroin heavy chain and light chain form an amphiphilic secondary structure

(Figure 1.1 B-i – ii) that assembles into 100 – 200 nm spherical silk fibroin micelles in water (Figure 1.1 B-iii).[54,55] These possess a hydrophobic core with a hydrophilic outer shell due to the influence of the hydrophobic blocks and hydrophilic terminal domains in the silk fibroin heavy chain.[56] Silk fibroin micelles are highly sensitive to external influences and can be chemically treated to yield silk fibroin nanoparticles with dense crystalline cores. Several methods exist to do this, and these are introduced in section 1.2.3.

In addition to imparting unique mechanical properties, the heavy and light chains of silk fibroin lack arginine-glycine-aspartic acid (RGD) motifs that are essential for cellular binding via the integrin receptor,[57] and so the primary structure reduces the available binding sites for silk fibroin to interact with cells. An assessment of primary structures of the heavy and light chains reveals that silk fibroin is also susceptible to degradation by several enzymes (e.g. protease XIV, α-chymotrypsin, papaïn, collagenase and matrix metalloproteinases)[58,59] and thus the inherent (long term) biodegradation of the material. Biodegradation is important for the design of healthcare materials and thus is discussed in the following section.

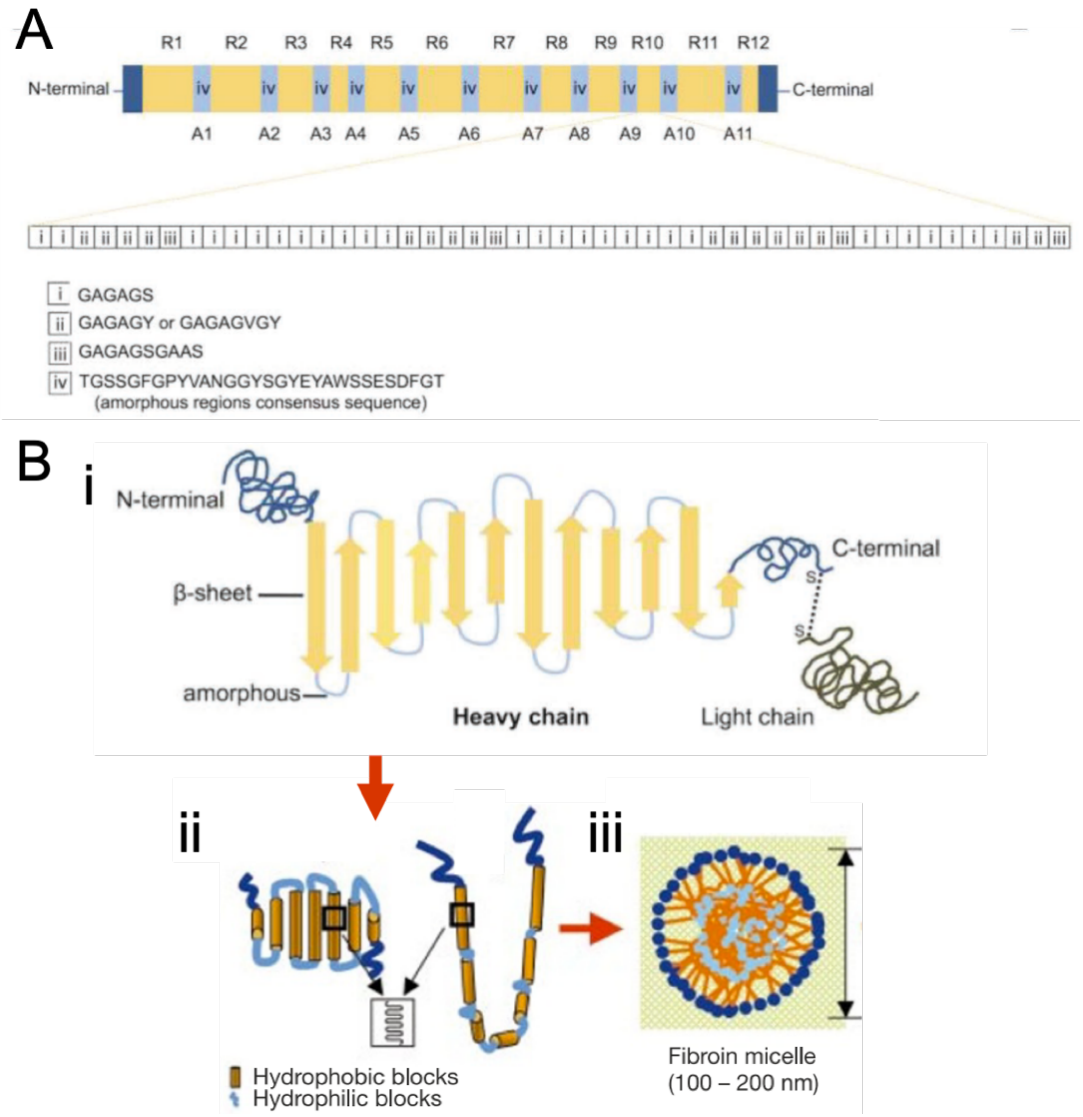

Figure 1.1. Schematic representation of silk fibroin primary, secondary and micellar structures. (A) Schematic depicting the primary structure of the silk fibroin heavy chain. (B) Schematic depicting the (i) amphiphilic secondary silk fibroin structure, (ii) conformation in water and (iii) resulting micellar assembly. A – C adapted from [42].

1.2.2. Biocompatibility and biodegradability

The clinical approval of first-generation silk fibroin surgical sutures (Ethicon Inc., Somerville, NJ, USA) and SERI® Surgical Scaffold (Sofregen Inc., Medford, MA, USA) meshes have demonstrated the biological performance of silk fibroin in humans.[41] In particular, SERI® surgical meshes have been used in two-stage breast reconstruction surgery, with a 2 year follow up of 153 histological samples revealing that the implants only caused minimal to mild inflammation.[60] Some macrophage and lymphocyte infiltration was detected in tissue samples, however 95.4% of samples displayed inflammatory profiles that were classed as normal under the circumstances of medical device implantation.

Under FDA guidelines a material can only be classed as biodegradable if it exerts substantial degradation within 60 days of implantation.[41,42] Based on this FDA definition silk fibroin cannot be classified as a biodegradable material as it retains its tensile strength for several months before displaying notable degradation.[41,61] The long term persistence of silk fibroin in humans was evidenced in the SERI® breast reconstruction clinical trials using 3D breast anatomy imaging and scaffold integration assessments. As an indication of degradation at this time point, a SERI® surgical scaffold implanted in a horse for hernia repair was found to have partial degradation with no relapse of hernia[44] 2 years after implantation and this supports the wider pre-clinical data demonstrating the long term biodegradability of silk fibroin.[61] The susceptibility of silk fibroin to degradation can be attributed in part to proteolytic enzyme-sensitive regions on the fibroin primary structure.[42] However, additional factors can affect the rate of material degradation including: (i) previous patient

exposure to silk fibroin, (ii) location in the body, (iii) size of implant, and (iv) mechanical stress on the implant and (v) secondary structure.[42] An appreciation of these contributing factors is particularly important when developing novel silk-based platforms, such as nanoparticles, as their biodistribution, particle size and physiological interactions are substantially different to implantable silk-based healthcare materials.

The safety and degradation profiles generated for current silk fibroin-based medical devices have provided a solid framework from which to design silk fibroin platforms for intravenous applications. For example, adverse hypersensitivity reactions to "virgin" (i.e. not degummed) silk surgical sutures were first attributed to the immune recognition of sericin,[41] and silk nanomedicine production benefits today from these findings as well refined degumming processes are already available to extract fibroin from the silk fibre.[62] Comprehensive reviews on silk fibroin biocompatibility reveal that the material has superior or comparable *in vivo* tolerability to many other synthetic (e.g. polycaprolactone) and natural (e.g. collagen) materials used in the healthcare setting.[61,63] The wider literature has firmly established the biocompatibility of silk fibroin in animals (e.g. mice,[64,65] rats,[63,66] sheep,[67] horses[44]) and humans.[45,60] However, the intravenous performance of silk fibroin cannot be assumed from this and so silk nanomedicines will ultimately have to undergo individual safety profiling to validate their suitability for use as an injectable anticancer nanomedicine.

1.2.3. Silk fibroin nanoparticles

The secondary structure of silk fibroin is responsible for its self-assembly into micelles in water (outlined in Figure 1.1 B-iii) and several strategies exist to exploit this to generate spherical silk fibroin particles within the micro- and nano- size range.[68] Processing conditions include, but are not limited to, salting out, capillary microdot printing, polyvinyl alcohol blending, ionic liquid utilisation, electrospraying, electric field application and organic solvent nanoprecipitation.[68] Solvent nanoprecipitation,[40,69,70] using either acetone or isopropanol, is one of the most robust methods available for generating spherical silk fibroin nanoparticles (approximately 40 – 200 nm) with exceptionally high uniformity (polydispersity index of approximately ≤0.1)[40,70] and stability.[56] Silk fibroin nanoparticles of this size are predicted to be ideally suited for use as anticancer nanomedicines as this size range is optimal for exploiting the EPR effect to passively target tumours.[71] They can also be readily surface modified with synthetic "stealth" polymers such as PEG[72,73] to reduce their interactions with mononuclear phagocytes in the circulatory system.[40] The principles of PEGylation, and the motivation for doing this, are outlined in more detail in section 1.4.1. In addition, they can be loaded with therapeutic payloads such as drugs by adsorption to the particle surface post-production.[40,69] Often, silk fibroin nanoparticles that are manufactured are 100 nm in size as these are also within the optimal size range for entrapment in intracellular vesicles following internalisation by endocytosis.[74] Endocytic uptake is the primary method used by nanomedicines to enter cells and deliver payloads intracellularly. The process of endocytosis and principles of intracellular drug delivery are outlined in the following section to provide insight into

their fundamental role dictating the success of anticancer drug delivery nanomedicines.

1.3. Endocytosis

Cellular internalisation was first documented in 1882 by Elie Metchnikoff and the process was subsequently named "phagocytosis" after the Greek "phagos" (to eat) and "cyte" (cell).[75] A restructuring of the terminology was necessary as the existence of different uptake pathways became more apparent, and "endocytosis" was coined in 1963[76] as an umbrella term describing the internalisation of material into the cell. Endocytosis is sub-divided into two categories: phagocytosis and pinocytosis. Today, phagocytosis is defined as a specialised form of endocytosis wherein pathogenic species or apoptotic debris are internalised by specialised immune cells; whilst pinocytosis refers to several homeostatic membrane recycling mechanisms that virtually all cells use to regulate the intracellular and extracellular environments (Figure 1.2).[77] Pinocytotic uptake pathways (e.g. clathrin-mediated endocytosis, caveolae mediated endocytosis, dynanmin independent processes and micropinocytosis)[78] are more specialised for non-immune related cargo such as growth factors, amino acids, vitamins and inorganic salts[78] and are implicated in the regulation of synaptic signalling and extracellular matrix remodelling.[79] However, they are also a primary target for targeting with nanomedicines and an understanding of the different endocytic mechanisms and downstream trafficking pathways is necessary to appreciate the exploitation of endocytosis for advanced drug delivery purposes.

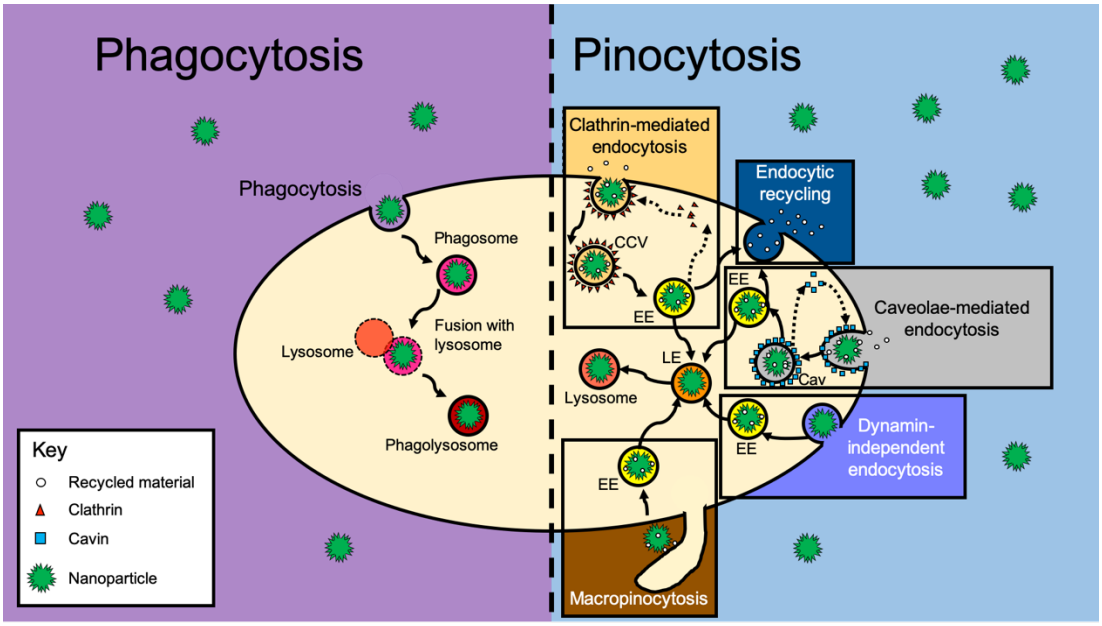

Figure 1.2. Schematic representation of endocytosis. Phagocytosis and the different pinocytotic internalisation pathways are represented. A nanoparticle is used to represent nanomedicine internalisation. EE = early endosome; LE = late endosome; Cav = caveosome, CCV = clathrin coated vesicle.

1.3.1.1. Phagocytosis

Phagocytosis is the primary mechanism used by professional phagocytes of the immune system (e.g. macrophages, neutrophils, dendritic cells) to internalise and destroy cargo that has been opsonised by antibodies or complement.[80] Opsonisation refers to the "coating" of cargo with antibodies or complement proteins and this allows specialised immune cells to recognise cargo using antibody (Fc receptor) or complement receptors.[81] Upon recognising opsonised material, phagocytosis begins with the remodelling of the actin cytoskeleton to promote engulfment into a phagosome.[82] Next, phagosome maturation occurs and it then fuses with the lysosome, forming a phagolysosome.[83] Phagolysosomes are characterised by a luminal pH of 4.5

and contain proteolytic (e.g. cathepsins) and hydrolytic (e.g. lysozyme) enzymes, antimicrobial proteins (e.g. defensins) and reactive oxygen (e.g. superoxide and nitrogen species (e.g. inducible nitrous oxide synthase).[83] These factors maintain a highly destructive environment that functions to degrade pathogens and dysfunctional cells into antigens that are then presented to adaptive immune cells on major histocompatibility complex molecules so that they can mount an appropriate immunogenic or tolerogenic response.[84]

1.3.2. Pinocytosis

Pinocytosis is used ubiquitously by all eukaryotic cells to sample the extracellular environment. This involves ingesting small volumes of fluid into vesicles and then trafficking internalised cargo to specific compartments within the cell.[77] Pinocytotic trafficking begins with the internalisation of cargo into an early endosomal compartment that possesses a slightly acidic luminal pH (pH 6.0).[85] The early endosome functions to mediate the dissociation of receptors from cargo and their subsequent sorting into recycling or degradative endosomal compartments.[85] Recycling back to the cell membrane is carried out by the recycling endosome, and this is the default endocytic fate for endocytosed receptors such as the transferrin receptor and epidermal growth factor receptor.[86] Non-receptor-based material is then trafficked to the Golgi body for intracellular processing, or to the late endosome (pH 5.0 – 6.0) and finally lysosomes for degradation. Unlike phagocytosis, which is restricted to immune cells, pinocytotic entry can occur by one of several distinct mechanisms and these are outlined below to highlight their importance in healthy cell function and homeostasis.[87]

1.3.2.1. Clathrin-mediated endocytosis

The most widely studied mechanism of non-phagocytic endocytosis is clathrin-mediated endocytosis due to its importance in the uptake and recycling of transferrin, epidermal growth factor and low-density lipoprotein.[88] Clathrin-mediated endocytosis is initiated when a ligand binds its receptor, causing the cell membrane to invaginate and recruit clathrin to the site of contact.[89] Next, clathrin polymerises into a clathrin-coat and surrounds the membrane invagination to provide structure and form an early clathrin-coated vesicle. Dynamin-dependent vesicle scission then occurs and clathrin rapidly disassembles to yield a 50 – 300 nm vesicle that traffics into early endosomes.[89] At this point the contents of the endocytic vesicle are sorted, with the internalised receptors being returned back to the cell surface via the recycling endosome,[85] ligands being shuttled to the golgi network, and non-specific bystander material entering the degradation pathway for destruction in lysosomes.

1.3.2.2. Caveolae-mediated endocytosis

Caveolae are cholesterol-enriched regions of the cell membrane that are predominantly expressed by fibroblasts, endothelial cells, adipocytes and smooth muscle cells.[90] These regions interact with the caveolin family of membrane proteins,[91] which induce membrane curvature. Then, cavin membrane proteins cause invagination into 60 – 80 nm flask shaped membrane pits,[90,92] and finally, dynamin acts to break the membrane and facilitate vesicle budding, yielding an early caveosome that traffics to the early endosome for cargo sorting.[93] As with clathrin-mediated endocytosis, internalised

material is sorted through either the recycling (recycling endosome), processing (Golgi complex) or degradation (late endosomes/lysosomes) pathways.

1.3.2.3. Dynamin independent endocytosis

Clathrin-mediated endocytosis and caveolae-mediated endocytosis represent only two types of endocytosis carried out by cells. These are both classed as "dynamin dependent" pathways, yet additional "dynamin independent" pathways also exist and these are essential for the internalisation of cholera toxin B, glycosylphosphatidylinositol (GPI)-linked proteins, cytokines and growth hormones.[94,95] These pathways are defined by the proteins that influence uptake into their respective pathways: ADP-ribosylation factor 6 (ARF-6), cell division cycle 42 (CDC42) and Ras homolog gene family, member A (RhoA).[74] As described below, the mechanism of uptake differs between these pathways due to the lack of dynamin-mediated vesicle scission. However, the mechanism of vesicle budding has still not been fully elucidated. Despite this, all pathways ultimately converge at the early endosome for cargo sorting and are therefore relevant routes for therapeutic targeting with nanomedicines.[77]

ARF-6 is a GTPase that regulates the endocytosis of ATP binding cassette transporter A-I, which in turn is used to carry out cholesterol efflux to maintain intracellular cholesterol homeostasis.[96] The pathway is also involved in major histocompatibility complex class I and glucose transport protein 1 recycling and helps maintain cell-cell and cell-extracellular matrix (ECM) interactions through recycling of adhesion

molecules (e.g. β1-integrin, CD44, ICAM-1).[86] ARF6 interacts with Rac and Rho GTPases to modulate the actin cytoskeleton leading to the initiation of membrane ruffling and subsequent membrane curvature.[97] Despite over 20 years of investigation the exact mechanisms coordinating ARF6 vesicle scission have not yet been elucidated.[86] The current consensus is that ARF6 vesicular budding interacts with Rabs, guanine nucleotide exchange factors, GTPase-activating proteins and other intracellular pathways such as clathrin-mediated endocytosis to facilitate intracellular trafficking and cargo sorting.[86]

Another two forms of dynamin independent uptake, namely CDC42 and RhoA mediated endocytosis, are also viable candidates for targeting with nanomedicines. However, the downstream mechanisms governing intracellular trafficking of their vesicles remain to be determined. CDC42 is a member of the Ras superfamily of GTP-binding proteins that carries out dynamin-independent formation of ~50 nm tubular invaginations of the cell membrane.[74] CDC42-mediated endocytosis is the principle mechanism used to internalise glycosphingolipids, as well as key probes used in the generic investigation of nanomedicine uptake such as cholera toxin B.[98] RhoA, another member of the Ras superfamily, regulates actin cytoskeletal rearrangement and is essential for maintaining cell shape and responding to the ECM by recycling signalling molecules for mechanotransduction.[99] During endocytosis, Rho-A-dependent mechanisms are understood to coordinate the internalisation of the β-chain of the IL-2 receptor in immune cells and fibroblasts.[100]

Macropinocytosis is perhaps the best studied method of dynamin independent endocytosis as this mechanism of uptake is characterised by membrane ruffling and

internalisation of large quantities of extracellular fluid into large (>200 nm) endocytic vesicles known as "macropinosomes".[74] The process of macropinocytosis is actin-dependent, and the indiscriminate and constant formation of membrane ruffles makes this method of internalisation appealing for nanomedicine delivery due to the lack of receptor targeting needed to gain access to the target cell.

1.3.3. Endocytosis – a primary drug delivery target

The discovery of the lysosome in 1955 by Christian de Duve[101] was quickly followed by the observation that endocytosis could be used as a drug targeting strategy.[76,102] "Lysosomotropic" drug delivery was proposed in 1974[103] as a mechanism to deliver payloads to specific intracellular compartments and this seminal piece continues to form the basis for nanomedicine design today. As de Duve also coined the term "endocytosis",[76] efforts to utilise endocytosis for drug delivery have been underway since the discovery of the system. Today, clinically approved anticancer nanomedicines such as Doxil[3] and Abraxane[4] are used as second-line therapies for treatment of chemotherapy resistant breast tumours as they utilise lysosomotropism to bypass drug efflux pumps,[104] limit the bioavailability of the free drug during transit, and thereby reduce some of the associated systemic toxicities.[105] Both Doxil and Abraxane exploit caveolae-mediated endocytosis to enter the degradation pathway.[87,106] To date this has been the most successful route of entry used by nanomedicines in a clinical setting.[106,107]

The design of nanomedicines is influenced by nature and exploits physiological processes. This is particularly evident when targeting endocytosis. Following the success of caveolae-mediated endocytic targeting there has been a surge in interest in the pathophysiology of endocytic pathways as they can be used to inform on nanomedicine design. Clathrin-coated vesicles have a size of 50 – 300 nm[74] and they are aptly suited for intracellular targeting with nanomedicines. Numerous attempts have been made to target these vesicles using nanoparticles constructed from a range of materials including PLGA, polylactic acid (PLA), chitosan and silica.[87] Often these particles possess a targeting moiety such as transferrin in order to force the nanomedicine into clathrin-coated vesicles by exploiting receptor-mediated endocytosis. However, to date a targeted nanomedicine has not successfully made it into routine clinic use because targeted nanomedicines have yet to demonstrate superior intracellular targeting when compared to passive nanomedicines in the clinical setting[108,109] due to issues relating to the underlying biology (e.g. heterogeneity in expression, receptor down regulation) and the intracellular fate (e.g. rapid endocytic recycling, poor localisation to degradative compartments) of drug-carriers following their internalisation.[1,26] Therefore, EPR utilisation and passive drug delivery using nanomedicines remains an essential method of targeting tumours even today. The reasons for this are explored in more detail in the following section.

1.4. Targeting cancer with nanomedicines

Cancer targeting was one of the main strategic themes identified in the nanomedicine policy briefing published by European Science Foundation.[2] The design of second generation nanomedicines for anticancer drug delivery has been underway since the official consolidation of the field. Nanomedicines typically target solid tumours by exploiting the EPR effect and use endocytosis and intracellular trafficking to control drug release in late endosomal and lysosomal compartments.[1] Efforts to yield a successful advanced anticancer drug delivery system have a sound foundation with the early the pre-clinical and clinical testing of Doxil and the polymer-drug conjugate PK1 (FCE28068) to improve the circulatory and intracellular pharmacokinetics of the anthracycline chemotherapeutic drug doxorubicin.[22,110] The successes (Doxil) and failures (PK1) of these first-generation nanomedicines catalysed a surge in development of pre-clinical and clinical products as anticancer nanomedicines. However, the translation of nanomedicines into routine clinical use has been severely hindered by limitations in nanomedicine design and the numerous biological barriers that are encountered in the body.[17,111] There is now extensive literature on nanomedicine performance and a demand for novel nanomedicines that have been optimised according to the lessons learned from first-generation products. Anticancer silk-based nanomedicines are interesting platforms to address this demand. However, there is the need to maximise and understand circulatory performance, intracellular trafficking and desirable interactions with the tumour microenvironment.

1.4.1. Physicochemical properties of nanoparticles

The physicochemical properties of nanomedicines play a fundamental role in both their circulatory and intracellular performance. Therefore these factors must be tuned accordingly to maximise the pharmacokinetic performance of injectable nanomedicines. One of the most important factors to consider is particle size, as this influences extravasation from the bloodstream, cellular interactions and the type of endocytic pathways that can be exploited for intracellular targeting.[112] Typically, nanoparticles that are between 50 – 100 nm are classed as optimal for intravenous administration as this is above the lower threshold for efflux out of the vessel between cell-cell junctions (<6 nm),[113] yet small enough not to become permanently trapped in the dense extracellular matrix (ECM) of the tumour microenvironment.[71] Particles smaller than 50 nm induce less membrane curvature when interacting with the plasma membrane of cells when compared to 50 – 100 nm sized nanoparticles.[114] However, plasma membrane interaction is necessary for subsequent invagination and internalisation into an endocytic vesicle. This was demonstrated by Chithrani *et al.* using gold nanoparticles to show that the particle-cell adhesion forces in human cervical adenocarcinoma (HeLa) cells driving membrane invagination are optimally induced by 50 nm particles when compared to smaller (14 nm) and larger (74 nm) nanoparticles.[114] As particle-cell interactions are ultimately responsible for successful internalisation of particles by endocytosis, this being the primary objective of an anticancer nanomedicine, the importance of correct nanoparticle size tuning during particle design cannot be understated. If nanomedicines are very large (>300 nm), the available pathways of uptake are restricted to phagocytosis or macropinocytosis and this is undesirable unless the nanomedicine is specifically intended for immune cell

targeting.[74] As described in section 1.3, the vesicular size range of most endocytic entry routes is between 50 nm to 300 nm in size, and so it is practical to adhere to the 50 – 100 nm limits required for optimal circulatory and particle-cell interactions to maintain the overall efficiency of the nanomedicine. Indeed, the success of clinically approved liposomal (e.g. Doxil, Caelyx) nanomedicines approximately 80 nm in size supports this design rationale. However, exceptions do exist such as Abraxane, which is ~ 130 nm in diameter. The performance of Abraxane highlights the complexity of tuning nanomedicine design, and additional physicochemical properties such as particle shape and surface chemistry contribute to the overall circulatory performance, cellular interactions and particle endocytosis to cumulatively influence the therapeutic outcome of the nanomedicine.

The shape of a nanomedicine can substantially influence its performance under the flow conditions experienced in the bloodstream and this can have knock-on effects on circulation times and cellular interactions.[115] Particulate nanomedicines are typically manufactured using processes that yield spherical shapes and this is advantageous as spheres are a thermodynamically favourable shape for targeting endocytosis.[71,114] However, developments over the past decade have introduced manufacturing techniques that can produce nanoparticles with a range of diverse shapes, including rods, worms, discs, ellipsoids and bullets.[116] The advent of Particle Replication in Non-Wetting Templates technology simplified the production of advanced nano-structures and this has enabled the effects of particle shape on nanomedicine performance to be explored more fully.[117,118] For example, Desimone *et al.* established the link between geometric shape and endocytosis and showed a causal link between increasing cylindrical nanostructure diameter and decreased endocytosis HeLa cells.[119] More

recently, 1 dimensional and 2 dimensional mathematical modelling of shapes including spheres, spheroids, capped cylinders and hourglasses predicted that capped cylinders are more readily internalised if they are more spherical in shape.[120] In addition, this study found that oblate spheroids can theoretically be internalised more readily than traditional spheres. However, this warrants experimental validation. The majority of studies investigating shape have concluded that shaped nanomedicines are not internalised as readily as spherical nanomedicines and this, along with manufacturing limitations, is possibly the reason that most particulate nanomedicines are spherical in shape. However, when designing anticancer nanomedicines, it is important to consider the overall performance of the carrier and shaped nanomedicines consistently outperform spherical ones in studies investigating circulatory half-life and clearance.[121] The superior circulatory performance of shaped nanomedicines has been pioneered by Discher *et al.* since 2007 showing that worm-like nanoparticles had 10 times higher circulatory times than spherical ones.[122] This was attributed reduced in interactions with macrophages of the mononuclear phagocytic system and a resulting reduction in clearance from the bloodstream.[122] Therefore, the effects of particle shape can significantly influence nanomedicine performance. However, these factors are complex and shape tuning should be considered in specific circumstances when the nanomedicine is designed for long term circulation.

The physical (e.g. size, shape) properties of nanomedicines are likely to work in a synergistic manner to influence overall performance at circulatory, cellular and intracellular levels. However, particle surface chemistry is equally important at each level of drug targeting and this must also be fine-tuned to ensure the nanomedicine can perform to optimal performance.[17] Hydrophobic and van der Waal's forces are

governed by factors within the extracellular environment such as pH, ionic strength and temperature, and act to form attractive or repulsive forces between the particles themselves, with serum or ECM proteins, or at the plasma membrane to induce membrane curvature and subsequent endocytosis.[123] Like the effects of particle shape, different particle surface charges can have variable effects on the different levels of drug targeting and so must be adjusted to the target disease state in order to fully optimise the nanomedicine for its purpose. For example, cationic nanomedicines have been shown to interact more readily with the negatively charged plasma membrane when compared to neutral or anionic nanomedicines.[124,125] This impacts the rate of particle internalisation in a charge dependent manner, with cationic nanomedicines being endocytosed at a faster rate than their neutral or anionic counterparts.[126] Whilst this is a desirable feature for a passively targeting lysosomotropic anticancer nanomedicine, cationic nanomedicines also interact avidly with serum and ECM proteins of the blood and circulation, respectively. This in turn can substantially impair their circulatory or intratumoural performance as these cationic carriers are opsonised, recognised by the MPS and cleared rapidly. [127,128] This is known as the "protein corona effect".[129] In contrast, anionic nanomedicines are therefore desirable as injectable anticancer nanomedicines as their improved circulatory performance (necessary to reach the tumour) takes priority over efficient intracellular targeting.

Importantly, particle surface chemistry can be tuned to suit the disease applications of the nanomedicine and the most common method of doing this is by coating the particle surface with synthetic polymers; a prime example is the use of the PEG polymer.[130] This process, called "PEGylation", involves conjugation of PEG to the surface of the nanomedicine, which acts as a "stealth" polymer to reduce particle-protein interactions

with opsonins in the blood and thereby enhance the circulatory performance of the nanomedicine.[131,132] PEGylation remains the gold standard of optimising nanomedicine surface chemistry for intravenous administration even 40 years after the technique was first demonstrated.[133] This highlights the effectiveness of the process at reducing clearance by cells of the mononuclear phagocytic system.

Clearly there are numerous particle-specific physicochemical factors that influence the overall performance of nanomedicines and these must each be considered with the target disease state in mind when designing a novel nanomedicine. In the case of anticancer targeting, spherical, PEGylated nanomedicines within the 50 – 100 nm size range are typically employed due to the overall desirable performance that this combination has on circulation, cell binding and intracellular trafficking. This rationale is evidenced by clinically approved nanomedicines and supported by unsuccessful models that have failed in the clinic. However, particle-specific factors are only one type of influence that can affect nanomedicine performance, and tumour-specific barriers also impact efficient nanomedicine performance at the cellular and microenvironmental level.

1.4.2. Tumour-specific influences

Particle-specific modulators of nanomedicine function can be easily circumvented by informed particle design. However, anticancer nanomedicines are faced with additional tumour-specific barriers to drug delivery including tumour cell heterogeneity, tumour associated cells and the physical tumour microenvironment.[134] Often these factors are highly variable between cancers and act to prevent effective chemotherapeutic treatment of tumours, including those treated with nanomedicines.

At present, tumour specific modulators of nanomedicine performance present a serious challenge to successful therapeutic outcomes and a more thorough understanding of these mechanisms is thought to be the key to adapting nanomedicine use to ultimately improve chemotherapeutic treatment of cancers.

1.4.3. Tumour cell heterogeneity

Part of the difficulty in treating cancers has been attributed to the heterogeneity of tumours with regard to individual tumour cells and the support network of "tumour-associated" stromal and immune cells that promote the metastatic tumour microenvironment.[135] Over the last decade it has become apparent that cancer stem cells give rise to genetically heterogeneous clonal populations that co-exist within the tumour site.[136–138] The diversity of these sub-clones makes using chemotherapeutic drugs (or the use of precision drugs) to treat tumours particularly difficult as drug-resistant sub-clones can expand following treatment, ultimately resulting in the recovery of the tumour in a more drug-resistant state.[104] This substantially impairs the effectiveness of conventional chemotherapeutic treatment and monoclonal antibodies (e.g. Herceptin) and is one of the reasons that combination therapy is necessary to treat many solid tumours.[138,139] Theoretically nanomedicines are well-positioned to revolutionise therapeutic targeting of tumours due to their ability to carry more than one payload and be surface modified with targeting ligands. However, efforts to produce a targeted nanomedicine have not yet been successful[109] and achieving this remains one of the major challenges within the field.

In addition to tumour cell heterogeneity, the tumour microenvironment is populated by a complex support network of immune cells (e.g. monocytes, macrophages) and stromal cells (e.g. fibroblasts, pericytes) that respectively drive a highly immunosuppressive environment and maintain a dense ECM to promote tumour growth and survival.[140,141] Whilst their pro-tumorigenic effects are well-established, tumour-associated populations are now being recognised as key regulators of nanomedicine efficacy as their effects on the tumour microenvironment restrict nanomedicine accessibility and tumour cell targeting. As the appreciation of the importance of microenvironmental influences has increased, so to have efforts to characterise nanoparticle-cell and nanoparticle-ECM interactions with the overall aim of better equipping nanomedicines to treat "off-target" cells and circumvent physical microenvironmental challenges that they encounter.[142] These factors and strategies to overcome them using nanomedicines are more fully explored in sections 1.4.4 and 1.4.5.

1.4.4. Tumour-associated macrophages

Tumour-associated macrophages are dysfunctional immune cells that maintain the highly immunosuppressive environment at the tumour site. They are recruited to the tumour as monocytes by cancer cells expressing colony stimulating factors 1 and 2[143,144] and then subsequently differentiate into M2-like "wound-healing" macrophages due to tumour microenvironmental influences including hypoxia,[145] abnormal ECM composition and tumour-derived inflammatory mediators (e.g. interleukin-6, high-mobility group protein 1).[142] Once differentiated, tumour-associated macrophages down-regulate the actions of tumoricidal cytotoxic T

lymphocytes and modulate T regulatory and T helper cell profiles to further the wound-healing environment, leading to enhanced recruitment and activation of fibroblasts and extensive deposition of ECM proteins.[146] In some tumours, macrophages can make up over 50% of infiltrating immune cells and there is a direct correlation with the proportion of intratumoral macrophages and poor prognosis in tumours of the breast, stomach and lung.[142] Tumour-associated macrophages have been shown to promote the growth of tumours by releasing vascular endothelial growth factor to drive angiogenesis and facilitate a route for metastasis.[147,148] In addition, tumour-associated macrophages are induced by tumour cell-derived colony stimulating factor 1 to express epidermal growth factor, which in turn increases cancer cell division and leads to more colony stimulating factor 1 secretion that forms a paracrine loop cycle.[149] An association between tumour-associated macrophages and cancer stem cells has also been demonstrated in breast cancer as a result of epidermal growth factor interactions,[150] and this is thought to support their self-renewal within the tumour site.

In the context of anticancer treatment, tumour-associated macrophages have been shown to impair the actions of some chemotherapeutic drugs including methotrexate, cyclophosphamide and 5-fluorouracil, thereby contributing to chemotherapeutic resistance.[151] Interestingly, tumour cell cytotoxicity of doxorubicin is also reduced in the presence of tumour-associated macrophages.[152] However, doxorubicin-killed tumour cells are highly immunogenic and have been shown to modulate the phenotype of tumour-associated macrophages back towards a tumoricidal state in a phenomenon called “immunogenic cell death”.[153] Nanomedicines are particularly well-suited to carry out macrophage reprogramming as tumour-associated macrophages have been

shown to limit the available therapeutic dose to tumour cells due to their phagocytic activity.[154] Rather than work to evade this bystander endocytosis, there has been a recent shift in interest within the field to exploit macrophage uptake to therapeutically attenuate their relationship with the tumour microenvironment.[142] By using this strategy, nanomedicines would therefore be equipped to deliver chemotherapeutic payloads to cancer cells whilst possessing the ability to polarise a key regulator of the tumour microenvironment to further contribute to a tumoricidal state.

1.4.5. Physical tumour microenvironment

Advancements in nanomedicine design may be able to overcome the problems of tumour cell and microenvironmental heterogeneity. However, the physical tumour microenvironment is another major regulator of nanomedicine performance at the tumour site and knowledge of these interactions can be used to further improve the development of nanomedicines. The influence of the physical tumour microenvironment on nanomedicine performance is not a recent revelation to the field. The principles of EPR govern tumour targeting with nanomedicines[16] and tumour interstitial pressure has long been understood to impair nanomedicine access to the tumour site.[155,156] However, over the past 15 years substantial attention has been given to the ability of cells to sense the elasticity of their surrounding ECM.[157–159] Many early studies investigating mechanosensing were conducted using mesenchymal stem cells, epithelial cells or fibroblasts cultured on natural (e.g. fibronectin, collagen) and synthetic (e.g. polyacrylamide, polydimethylsiloxane) hydrogel substrates to mimic the physiological stiffness of tissues *in vivo*.[160] Such studies have established a

functional relationship between substrate stiffness and cellular cytoskeletal rearrangement that has been linked to a range of cellular processes including gene expression,[161] differentiation[159] and epithelial-mesenchymal transition.[157,162] Today, substrate elasticity is widely understood to regulate healthy physiology of the heart,[163,164] lungs,[165] breast[166,167] and skeletal muscle,[168] and substrate stiffness has been shown to influence disease states in these tissues, including the development of cancer.

The tumour microenvironment becomes substantially more rigid during tumorigenesis and this is one of the diagnostic features of cancers.[169] As the role of substrate stiffness in healthy tissue function has become more apparent, so too has its role in tissue pathology and substrate stiffness is now understood to drive tumour progression in breast cancer.[167,170,171] Indeed, breast cells are highly mechanosensitive and respond to ECM cues during breast development and remodelling during pregnancy.[172] It is therefore not surprising that matrix stiffness is associated with epithelial-mesenchymal transition[157] in breast cancer progression and that the stiffest regions of breast tumours host the cells with the highest metastatic profiles.[167,173] Substrate stiffness is often linked to a poorer prognosis in patients suffering tumours of the breast,[174] brain[175] or colon[176] cancers. Cell-ECM interactions are heavily implicated in cancer progression, yet the effects of substrate stiffness on endocytosis is not fully understood. In the context of nanomedicine, the effects of substrate stiffness on endocytosis are of particular interest as this relationship may influence the cellular response to nanomedicines in a tumour microenvironment dependent manner.[177]

Endocytosis is heavily dependent on actomyosin assembly and disassembly and so differences in ECM elasticity have been proposed as a tumour microenvironmental factor that could influence the uptake efficiency and success of anticancer nanomedicines.[178] Huang *et al.*[179] were the first to demonstrate a stiffness-dependent relationship between substrate stiffness and endocytosis by using a stiffness-tuneable poly(acrylamide) (PA) hydrogel model to measure the endocytosis of 100 nm nanoparticles by bovine aortic endothelial cells cultured on substrates of varying elasticity (1.61 kPa – 5.71 kPa).[179] This study found that endocytosis of nanoparticles increased with increasing substrate stiffness, and this was supported by an independent study using REF52 fibroblasts the following year.[177] Importantly, the second study was unable to reproduce the results in HeLa cells and this could indicate that the observed stiffness-dependent relationship was cell-type dependent. Despite this, these studies were effective in establishing a potential relationship between the ECM stiffness the endocytosis of nanoparticles. However, the relevance of this in a physiological (*in vivo*) environment has yet to be assessed in the context of tumour targeting.

1.5. Hypothesis, Aims & Objectives

The principle hypothesis of this thesis is that silk fibroin nanoparticles can be used as anticancer nanomedicines to deliver chemotherapeutic payloads and carry out immunomodulation of the tumour microenvironment. This overall hypothesis has been broken down into specific aims and objectives, these are:

Chapter 3 will examine the mechanisms of drug release from silk fibroin nanoparticles *in vitro* in relation to lysosomal function. First, the effects of lysosomal acidity and proteolytic activity on drug release will be determined using a combination of simulated lysosomal buffer solutions. Next, lysosomal conditions will be manipulated in live human breast cancer cells to assess the impact of pH and proteolytic enzymes on lysosomotropic drug release from silk fibroin nanoparticles.

Chapter 4 will assess the impact of silk fibroin nanoparticles on macrophage function *in vitro* to determine silk fibroin nanoparticle immunogenicity and their potential to exert immunomodulatory effects. The first objective will be to compare silk fibroin nanoparticle-mediated macrophage activation to leading inorganic and synthetic nanoparticles to provide a benchmark for silk fibroin nanoparticles. Then, the effects of silk fibroin nanoparticle PEGylation on immunomodulatory effects will be explored to investigate their ability to carry out macrophage reprogramming.

Chapter 5 will investigate the endocytic and intracellular trafficking pathways of silk fibroin nanoparticles especially in response to the cell cycle and culture substrate mechanics. Specific endocytic pathways used by silk fibroin nanoparticles will be identified and time-dependent intracellular trafficking profiles will be produced. Next,

the influence of cell cycle progression on silk fibroin nanoparticle endocytosis will be examined. The effects of substrate mechanics on endocytosis will also be determined by culturing human breast cancer cells on hydrogels to elucidate the extent of these effects on silk fibroin nanoparticle uptake.

Chapter 2: Materials and Methods

Chapter summary:

This chapter outlined the materials and general methods used in all experimental thesis chapters. This included: (i) silk fibroin nanoparticle production, modification and characterisation, (ii) cell culture and cell-based assays, (iv) flow cytometric analyses, (v) confocal microscopy, and (vi) stiffness-tuneable hydrogel production and functionalisation.

In this chapter, all chemicals and reagents were procured from Sigma-Aldrich (Sigma-Aldrich, St. Louis, MO, U.S.A.) unless otherwise stated and were of a minimum purity of ≥ 90%.

2.1. Production of aqueous silk fibroin solution

Bombyx mori silk was extracted from cocoons (Tajima Shoji, Kanagawa, Japan) using a three-step protocol. First, cocoons were cut into 5 × 5 mm pieces and boiled in 0.02 M Na_2CO_3 for 60 min. The fibres were rinsed in double-distilled water (ddH_2O) and air-dried for 24 h. Next, fibres were dissolved in 9.3 M LiBr (Acros Organics, Geel, Belgium) solution at 60°C for 4 h to yield a 5 wt % solution that was then dialysed (Slide-A-Lyzer Dialysis cassette, 3.5 kDa molecular weight cut-off, Thermo Fisher Scientific, Waltham, MA, USA) against ddH_2O for 72 h. Finally, impurities in the aqueous silk solution were removed conducting by two 20-minute centrifugations at 8600 x g and collecting the supernatant each time. The silk solution was stored for up to 4 weeks at 4 °C.

2.2. Production of unmodified silk fibroin nanoparticles

Silk fibroin nanoparticles were produced using a nanoprecipitation method in which aqueous silk fibroin solution was added dropwise (20 µL/drop) to acetone, maintaining >75% v/v acetone volume.[40] Precipitated silk was then centrifuged at 48,400 × g for 2 hours, the supernatant was aspirated, and the pellet was resuspended in ddH_2O and

sonicated twice for 30 seconds at 30% amplitude with a Sonoplus HD 2070 sonicator (ultrasonic homogenizer, Bandelin, Berlin, Germany). The centrifugation, washing and resuspension steps for the silk fibroin nanoparticle preparation were repeated at least twice more. Silk fibroin nanoparticles were stored at 4 °C until use. A visual format of this procedure is available elsewhere.[70]

2.3. Production of PEGylated silk fibroin nanoparticles

PEGylation was performed as detailed previously.[40] Briefly, unmodified silk fibroin nanoparticles were surface decorated with PEG by reacting a 1:1 w/w ratio of unmodified silk fibroin nanoparticles with methoxypolyethylene glycol activated with cyanuric chloride (TST-activated mPEG, 5000 g/mol, Sigma-Aldrich) overnight in 2 mL $Na_2B_4O_7$ (50 mM, pH 9.4), with constant stirring at 4 °C (Figure 2.1).

PEGylated silk fibroin nanoparticles were then centrifuged at 48,400 × g for 2 h, the supernatant was aspirated, and the pellet was resuspended in ddH_2O and sonicated twice for 30 seconds at 30% amplitude. The centrifugation, washing and resuspension steps for the silk fibroin nanoparticle preparation were repeated at least twice more. PEGylated silk fibroin nanoparticles were stored at 4 °C until use.

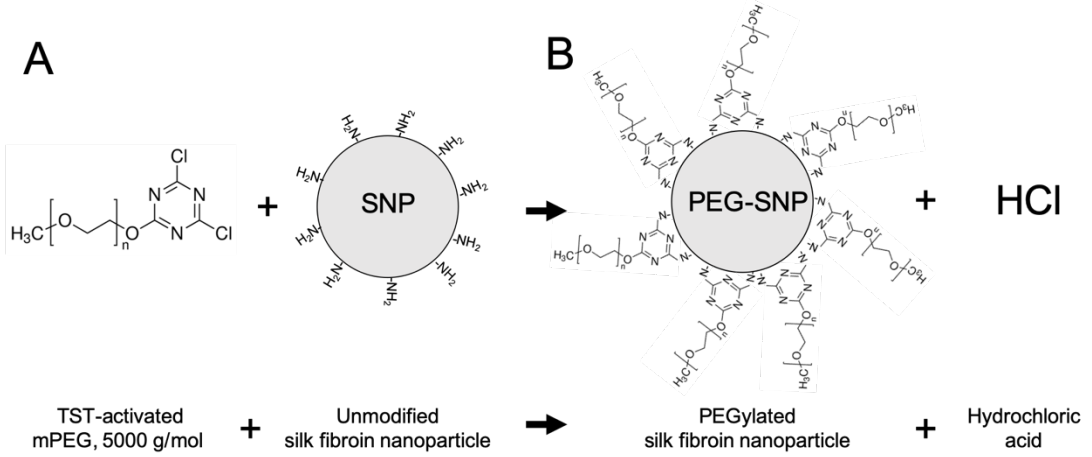

Figure 2.1. Schematic representation of silk fibroin nanoparticle PEGylation. (A) TST-activated mPEG 5000 is reacted overnight with unmodified silk fibroin nanoparticles (SNP). (B) TST-activated mPEG 5000 reacts with primary amines on unmodified silk fibroin nanoparticles, forming PEGylated silk fibroin nanoparticles (PEG-SNP) and HCl.

2.4. Characterisation of unmodified and PEGylated silk fibroin nanoparticles

Dynamic light scattering was used to determine the particle size distribution and polydispersity of unmodified and PEGylated silk fibroin nanoparticle in water using a Zetasizer Nano-ZS (Malvern Instrument, Worcestershire, U.K.). A refractive index of 1.33 was used for water to compute the particle size. Zeta potential was also determined with this instrument using laser doppler electrophoresis.

2.5. Labelling unmodified and PEGylated silk fibroin nanoparticles with Alexa Fluor®488

Unmodified and PEGylated silk fibroin nanoparticles were labelled with Alexa Fluor® 488 (AF488) to enable their identification in flow cytometry and confocal microscopy stuties. Fluorescent labelling was based on a previously published method [40]. Briefly, 1 mL of unmodified or PEGylated silk fibroin nanoparticles (10 mg/mL) were resuspended in 1 mL $NaHCO_3$ (0.1 M, pH 8.3). Next, 100 μL Alexa Fluor® 488 succinimidyl ester (Life Technologies, Carlsbad, CA, U.S.A.) (1 mg/mL) was dissolved in anhydrous dimethyl sulfoxide (DMSO), added to the nanoparticles and allowed to react overnight at 20 °C in the dark with stirring. The labelled nanoparticles were then centrifuged and washed four times with acidified water (pH 4.6) to remove unbound dye. This was followed by three washes with ultrapure water and the samples were stored at 4 °C in the dark until use.

2.6. Cell Culture

2.6.1. MCF-7

The human breast cancer cell line MCF-7 was purchased from ATCC (Manassas, VA, U.S.A.). This cell line was extracted from a pleural effusion and is representative of a metastatic, oestrogen-responsive breast epithelial cell.[180] Cells were cultured in DMEM (4.5 g glucose, 110 mg sodium pyruvate, 10%v/v FBS, and 10 μg/ mL insulin) in a humidified 5% CO_2 atmosphere at 37°C. Routine subculture was conducted every

2–3 days (when the cells had reached 80% confluence) by trypsinisation and re-plating the cells at a ratio of 1:4–1:3.

2.6.2. MCF-10A

The human non-tumorigenic breast epithelial cell line MCF-10A was purchased from ATCC (Manassas, VA, U.S.A.). This cell line was extracted from a patient with fibrocystic disease and is representative of healthy breast epithelial cell function.[181] Cells were cultured in DMEM/F-12 (4.5 g glucose, 110 mg sodium pyruvate, 5%v/v horse serum, 100 ng/mL cholera toxin, and 10 μg/mL insulin, 10 ng/mL epidermal growth factor, 0.5 μg/mL hydrocortisone) in a humidified 5% CO_2 atmosphere at 37°C. Routine subculture was conducted every 2–3 days (when the cells had reached 80% confluence) by trypsinisation and re-plating the cells at a ratio of 1:5 – 1:10.

2.6.3. MDA-MB-231

The human breast cancer cell line MDA-MB-231 was purchased from ATCC (Manassas, VA, U.S.A.). This cell line was extracted from a pleural effusion and is representative of a metastatic, triple-negative breast epithelial cell.[182] Cells were cultured in DMEM (4.5 g glucose, 110 mg sodium pyruvate, 10%v/v FBS, and 10 μg/mL insulin) in a humidified 5% CO_2 atmosphere at 37°C. Routine subculture was conducted every 2–3 days (when the cells had reached 80% confluence) by trypsinisation and re-plating the cells at a ratio of 1:4–1:3.

2.6.4. RAW 264.7

The mouse macrophage RAW 264.7 cell line was purchased from ATCC (Manassas, VA, USA). This cell line was extracted from an ascites of an Abelson murine leukaemia virus-induced tumour and is thought to be derived from peritoneal monocytes.[183] Cells were cultured in fully supplemented Dulbecco's Modified Eagle's medium (DMEM 4.5 g glucose, 110 mg sodium pyruvate, 10%v/v foetal bovine serum, and supplemented with 50 U/mL penicillin and 50 μg/mL streptomycin) in a humidified 5% CO_2 atmosphere at 37ºC. The culture of RAW 264.7 cells has been described previously.[184] Routine subculture was conducted every 2–3 days (when the cells had reached 80% confluence) by scraping cells, centrifuging at 380 × g for 4 minutes and re-plating them at a ratio of 1:5–1:10 onto plasma-treated tissue culture polystyrene. Cell passage number was controlled during all studies with these cells as they are susceptible to genetic drift. All experiments were conducted using cells under passage 20. Seeding for polarisation experiments was conducted at a density of 1.5 × 10^4 cells/cm^2 and cells were allowed to recover for 24 hours prior to conducting the *in vitro* experiments.

2.7. MTT Assay

The cytotoxicity of nanoparticles was verified using a 3-(4,5-dimethylthiazol-2-yl)-2,5-diphenyltetrazolium bromide (MTT) assay.[185] This assay measures cell viability as a measure of the total metabolism of MTT into an insoluble formazan salt. Depending on the experimental chapter, this assay was conducted on breast epithelial

cells (MCF-10A, MCF-7, MDA-MB-231) or mouse macrophages (RAW 264.7). The cell lines assessed are identified in the relevant chapters.

The general protocol used for the MTT assay was as follows. First, cells were seeded at 2×10^4 cells/cm^2 and allowed to recover overnight. Next, cells were either left untreated or were incubated in a humidified 5% CO_2 atmosphere at 37°C for the appropriate time point (24 – 72 hours) in complete DMEM supplemented with nanoparticles across a concentration range. Then, MTT (5 mg/mL in 1 × PBS) was added at 10% of the volume of cell culture media and cells were returned to the 37 °C incubator for 5 hours. The medium was then aspirated, the formazan product was solubilised with DMSO (100 μL), and the absorbance was measured at 570 nm. Data sets were then normalised to 1% Triton X-100 positive controls or negative controls containing untreated cells to determine the percentage of cell viability as a result of nanoparticle treatment.

2.8. Other assays

2.8.1. ELISA

Tumor necrosis factor-alpha (TNF-α) levels were measured with a mouse TNF-α DuoSet ELISA kit (R&D Systems, Minneapolis, MN, U.S.A.). In brief, RAW 264.7 cells were treated with unmodified and PEGylated silk fibroin nanoparticles as outlined in chapter 4 (section 4.2.8). Growth medium was removed and collected, clarified by centrifugation (2000 × g for 10 minutes), transferred to 2 ml low-protein-

binding Eppendorf tubes, and stored at -80 °C. TNF-α expression was analysed by quantifying the concentration of TNF-α in each of the supernatant samples using a mouse TNF-α ELISA kit as follows.

First, the supplied ELISA plate was prepared by diluting the capture antibody (R&D Systems, Catalogue #840143) in 1× PBS and coating with 100 µL per well. The plate was sealed and incubated overnight at 20 °C. The following morning, wells were aspirated and washed three times with 1× PBS-tween (0.05% Tween®). Plates were blocked with blocking buffer (1% BSA in 1× PBS) for 1 hour at room temperature and finally washed three times with 1× PBS-tween to finish plate preparation.

To run the ELISA, mouse TNF-α standard (R&D Systems, Catalogue #840145) was serial diluted, producing concentrations ranging from 31.3 – 2000 pg/mL. Then, 100 µL of supernatant samples or TNF-α standards were plated in triplicate into the plate and incubated for 2 hours at room temperature. Wells were then washed three times with 1× PBS-tween. The detection antibody (R&D Systems, Catalogue #840144) diluted, 100 µL was added to each well and the plate was incubated for 2 hours at room temperature. Wells were then washed three times with 1× PBS-tween. Streptavidin-horseradish peroxidase (R&D Systems, Catalogue #893975) was diluted, 100 µL was added to each well and incubated in the dark for 20 minutes at room temperature. Wells were then washed three times with 1 × PBS-tween. A 1:1 mixture of hydrogen peroxide and tetramethylbenzidine (R&D Systems, Catalogue #DY999) was prepared and 100 µL was added to each well and incubated in the dark for 20 minutes at room temperature. Finally, 50 µL 2 N H2SO4 (R&D Systems, Catalog # DY994) was added

as stop solution and the plate was read at 450 nm, with a 570 nm reading also being taken to allow for wavelength correction.

2.8.2. Griess assay

Nitric oxide was measured with the Griess assay as detailed elsewhere.[186,187] In brief, RAW 264.7 cells were treated with unmodified and PEGylated silk fibroin nanoparticles as outlined in chapter 4 (section 4.2.8). Growth medium was removed and collected, clarified by centrifugation (2000 × g for 10 minutes), transferred to 2 ml low-protein-binding microcentrifuge tubes, and stored at -80 °C. Nitric oxide expression was analysed by quantifying the concentration of nitrite in each of the supernatant samples using a Griess assay as follows.

First, a sulphanilamide (2% w/v) solution was prepared in 5% phosphoric acid. Next, N-1-napthylethylenediamine dihydrochloride (0.2%) (NED) was prepared in deionized water. A solution of sodium nitrite (10 mM) was used to produce a NO_2 standard by diluting 1:100 in fully supplemented DMEM to yield the highest standard concentration (100 μM). This was serial diluted (1:1) and 50 μL was added to triplicate rows, producing 12 standards ranging from 0 – 100 μM. 50 μL of control, nanoparticle treated or LPS treated supernatant samples were added in triplicate to remaining wells. Then, 50 μL sulphanilamide was added to all wells and incubated for 10 minutes at room temperature. After this, 50 μL NED was added to all wells and incubated for a further 10 minutes. Absorbance was measured at 540 nm and nitrite levels from samples were interpolated from the standard curve (Figure 4.3 B).

2.8.3. Lactate dehydrogenase assay

The lactate dehydrogenase assay was performed with a Pierce LDH Cytotoxicity Assay Kit (Thermo Fisher Scientific, Waltham, MA, USA) to assess membrane integrity in RAW 264.7 macrophages as follows. RAW 264.7 cells (2×10^4 cells/cm^2) were seeded into a 96 well plate and treated with unmodified and PEGylated silk fibroin nanoparticles as outlined in chapter 4 (section 4.2.8). Negative (untreated) and positive (1% v/v Triton X-100) controls were included in the plate layout. Next, 50 μL of each well was transferred to another 96 well plate in triplicate and 50 μL lactate dehydrogenase detection reagent (Thermo Fisher Scientific, Catalog # 88953) was added to each well. The plate was incubated for 30 minutes in the dark at room temperature and 50 μL stop solution (reductase inhibitor) was added to end the reaction. Absorbance at 490nm and 680nm was measured (POLARstar Omega, BMG Labtech GmbH, Germany)to allow for wavelength correction.

2.8.4. Antioxidant assay

An antioxidant assay kit was used to assess total antioxidant capacity in RAW 264.7 macrophages. In brief, RAW 264.7 cells were treated with unmodified and PEGylated silk fibroin nanoparticles as outlined in chapter 4 (section 4.2.8). Growth medium was removed, cells were washed three times with 1 × Hank's balanced salt solution (HBSS) (Thermo Fisher Scientific, Waltham, MA, U.S.A.), scraped and collected into falcon tubes, and centrifuged at 2000 × g for 10 minutes at 4°C. Supernatant was decanted, the pellet was resuspended in 1 mL HBSS and sonicated on ice. Lysates were then centrifuged at 10,000 × g for 15 minutes at 4°C and the supernatant was collected and

stored at -80°C. Total antioxidant capacity was quantified by analysing supernatant samples with an antioxidant assay kit (Cayman Chemical, MI, USA) as follows.

First, antioxidant assay Trolox (6-hydroxy-2,5,7,8-tetramethylchroman-2-carboxylic acid) was reconstituted in 1 mL ddH_2O and serial diluted to produce a standard (0 – 0.33 mM Trolox). Next, 10 µL of lysate samples or Trolox standards were added to triplicate wells along with 10 µL metmyoglobin and 150 µL chromogen. The reaction was started by adding 40 µL hydrogen peroxide (441 µM) to all wells and incubating in the dark for five minutes at room temperature. Absorbance was read at 405 nm using the POLARStar Omega and antioxidant concentration was extrapolated from the standard curve (Figure 4.3 D).

2.8.5. Reactive oxygen species assay

A reactive oxygen species assay was performed with a CellROX® Deep Red Reagent (Thermo Fisher Scientific, Waltham, MA, U.S.A.) to assess oxidative stress in RAW 264.7 macrophages as follows. RAW 264.7 cells (2×10^4 cells/cm^2) were seeded into 6 well plates and treated with unmodified and PEGylated silk fibroin nanoparticles as outlined in chapter 4 (section 4.2.8). Next, cells were washed three times with 1 × HBSS, stained for 1 hour with CellROX® Deep Red Reagent, scraped into 3 ml Falcon tubes and stained with SYTOX Green® as an exclusion dye. Cells were analysed immediately by flow cytometry (section 2.10), with 20,000 live events being recorded per sample.

2.9. Confocal microscopy

Confocal imaging was conducted on live cells immediately after dosing using a Leica TCS-SP5 confocal laser scanning microscope (Leica Microsystems GmbH, Wetzlar, Germany) equipped with a 40× magnification water objective with a numerical aperture of 1.25. Single confocal sections were acquired at an airy disc of 1. Subsequent image analysis was conducted using ImageJ v1.51k 1 (National Institutes of Health, Bethesda, MD, USA).[188] Specific experimental details for confocal imaging are outlined in the appropriate chapters.

2.10. Flow cytometry

Flow cytometry was used to measure cell-associated fluorescence of: (i) breast epithelial cells following exposure to fluorescently labelled nanoparticles (Chapters 3 & 5), (ii) macrophages following immunostaining for specific surface markers (Chapter 4), or (iii) breast epithelial cells following cell cycle staining (Chapter 5). For studies using breast epithelial cells, cells were washed three times with 1 × PBS, detached with trypsin (≤5 min), and collected into 5 ml Falcon tubes equipped with a 40 μm filter mesh (Becton Dickinson, San Jose, CA, USA) on ice. Cells were centrifuged at 4°C for 5 minutes and the supernatant was discarded and replaced with 1 × PBS. This process was repeated twice more to ensure full removal of trypsin. Cells were then stained appropriately using fluorescently labelled antibodies (chapter 4.2.6) or dyes (chapter 3.2.7 & 5.2.12). For studies using RAW 264.7 macrophages, cells

were washed three times with 1 × PBS, detached by scraping into 5 ml Falcon tubes, and then prepared for flow cytometry analyses using the same method above.

Flow cytometry data acquisition was conducted on a BD FACSCanto instrument (Becton Dickinson, San Jose, CA, USA) using BD FACSDiva software v6.3.1 (Becton Dickinson, San Jose, CA, USA). A minimum of 10,000 events were recorded within a gate that was either verified to contain a high proportion of live singlets (chapter 3.2.7); or live cells were specifically selected for during acquisition with the use of an exclusion dye (chapters 4 & 5). Subsequent data analysis was conducted using FlowJo v10.1 (TreeStar, San Carlos, CA, USA).

2.11. Production of stiffness-tuneable poly(acrylamide) hydrogels

PA hydrogels were produced by adapting a standard protocol from Tse *et al.*[189] The methods used to produce PA hydrogels with tuneable elasticity are detailed below.

2.11.1. Preparation of coverslips

First, 35 mm or 32 mm borosilicate glass coverslips (VWR International, USA) were subjected to two 30 minute washes (first wash: ddH_2O, second wash: ethanol) in an ultrasonic bath. Next, an organic cleaning solution was prepared that consisted of ddH_2O, ammonium hydroxide (NH_4OH) and hydrogen peroxide (H_2O_2) at a ratio of

5:1:1. The solution was heated to 70ºC and were cleaned by submerging them for 10 minutes, rinsing twice with ddH_2O, and drying with nitrogen.

Cleaned 35 mm coverslips were then passivated by submerging them in Sigmacote® siliconising solution for 5 – 10 seconds, allowing them to air dry and then washing in ethanol for 15 minutes in an ultrasonic bath. Coverslips were dried with nitrogen and stored at 4ºC for up to one month prior to use.

Cleaned 32 mm coverslips were silanised by submersion for 2 hours in a solution of acrylsilane (94.8% EtOH, 4.74% H2O, 0.44% ACS). Coverslips were then rinsed twice with ethanol, dried with nitrogen and tempered for 1 hour at 120ºC in a drying oven. They were then stored at 4ºC for up to one month prior to use.

2.11.2. Assembly of poly(acrylamide) hydrogels

Solutions of ddH_2O, acrylamide (40% w/v), bis-acrylamide (2% w/v), tetramethylethylenediamine (1.5% w/v) and ammonium persulfate (5% w/v) were used in the formation of polyacrylamide gels. Mixing of the solutions was conducted according to established ratios to produce hydrogels that were 0.5 – 20 kPa in elasticity. To produce the hydrogels: acrylamide, bis-acrylamide, TEMED and ddH_2O were mixed accordingly and vortexed briefly. Ammonium persulfate was then added to the wall of the centrifuge tube and vortexed to initiate the reaction. Next, 100 µL of the polyacrylamide solution was pipetted onto a 35 mm sigmacote coverslip and a 32 mm acrylsilanised coverslip was placed on top. The coverslips were left for 20 min to allow the gels to polymerise and then sigmacote coverslips were removed. The

remaining coverslips with the polyacrylamide gels attached were submerged in ddH_2O and stored at 4ºC for up to one week prior to use.

2.11.3. Functionalisation of poly(acrylamide) hydrogels

PA hydrogels were removed from the fridge and ddH_2O was aspirated and replaced with sulfo-SANPAH (0.2 mg/mL, in ddH_2O) to a volume sufficient to cover the entire gel. The gel was then placed in a UV chamber (5000-EC Series Modular UV Curing Flood Lamp, Dymax Corporation, Torrington, CT, U.S.A) and exposed to high intensity long wave (>300 nm) UV light for 1 minute. The hydrogels were then rinsed three times with HEPES buffer (50 mM in ddH_2O, pH 8.5) to remove unbound sulfo-SANPAH and incubated overnight at 37ºC with type I rat tail collagen (Corning Inc., Corning, NY, U.S.A.) (0.1 mg/mL, in HEPES buffer). The following morning the wells were aspirated and washed three times to remove unbound collagen prior to cell seeding.

2.12. Statistical analysis

All statistical analyses were plotted using GraphPad Prism 7 (GraphPad Software, La Jolla, CA, U.S.A.). Details of specific statistical tests are outlined in experimental sections of each chapter (chapters 3 – 5) Asterisks denote statistical significance, as follows: *p< 0.05, **p< 0.01, ***p< 0.001. Unless otherwise stated, data are presented

as mean values ± standard deviation (SD) and refer to the number of independent biological experiments.

Chapter 3: Silk fibroin nanoparticles – Proof of Lysosomotropic Anticancer Drug Delivery at Single Cell Resolution

Chapter summary:

This chapter assessed the potential of the silk fibroin nanoparticle to serve as a lysosomotropic anticancer drug delivery system. MCF-7 cells were exposed to doxorubicin loaded silk fibroin nanoparticles to monitor endocytic uptake and trafficking. The role of the lysosomal microenvironment in live MCF-7 cells was monitored by assessing the impact of lysosomal pH and enzymes on lysosomotropic drug release.

This chapter was published as an original article (Totten *et al.* 2017. J. Drug Target. 25, pp 865–872)[190] and has been adapted accordingly for this thesis. Data acquision and analysis for Figures 3.1, 3.3 – 3.7, and 3.9 was conducted by myself. This included silk fibroin nanoparticle preparation and characterisation, cell culture, flow cytometric analyses, confocal microscopy and cell-based lysosomal drug release studies. Data acquisition and analysis for Figures 3.2 and 3.8 was conducted in collaboration with Dr Thidarat Wongpinyochit. This included silk fibroin nanoparticle drug loading and fluorescent labelling, as well as buffer-based drug release studies. As the first author of the study, I wrote the manuscript with input from the other authors.

3.1. Introduction

The design of anticancer nanomedicines for solid tumour targeting typically exploits the enhanced permeability and retention (EPR) effect, where the leaky vasculature and poor lymphatic drainage at the tumour site promotes (passive) nanomedicine accumulation.[12,16] Often, the nanomedicines are designed for intracellular activation (e.g. exposure to enzymes, low pH) that triggers drug release. Therefore, endocytic uptake and correct intracellular routing (i.e. third order targeting)[1,191] is critical for achieving the desired pharmacological effect. This type of targeting has the potential to overcome drug resistance mechanisms (e.g. plasma membrane drug efflux pumps) by changing the mechanism of cellular entry of small molecular weight payload(s) from a physico-chemically driven partitioning process to an energy-dependent endocytic uptake mechanism. The subsequent accumulation of nanomedicines in lysosomes, the triggered payload release from the carrier and the ensuing movement

of the liberated drug from the lysosomes to its pharmacological site of action inside the cell is a process known as lysosomotropic drug delivery,[103] a term first proposed and demonstrated by Christian de Duve.[191,192]

The approval of nanoparticles for drug delivery to solid tumours, such as albumin-based paclitaxel nanoparticles (e.g. Abraxane, ABI-009) in 2005, has catalysed the field to develop second generation nanoparticles for this purpose.[193] Biopolymer-based constructs (e.g. cyclodextrin CRLX-101),[194] mannose and diethylenetriamine pentaacetic acid ^{99m}Tc-functionlised dextran[195] and proteins[4,196] are especially appealing because their inherent biodegradability renders them less likely to disrupt lysosomal function.[10] Silk is also especially appealing in this respect, and there is currently a growing movement proposing the use of silk in drug delivery applications.[68,197] Silk has been used for centuries as a suture material, confirming its biological safety,[42] and it can be fully reverse engineered to create novel material formats, including silk fibroin nanoparticles (reviewed in [68]). As a natural biopolymer, silk has remarkable capabilities to stabilise and protect therapeutic payloads (e.g. proteins, peptides and drugs).[198] The silk protein is biocompatible and biodegradable[66] and silk fibres and surgical meshes are approved for use in humans.[68] Most processes begin with *Bombyx mori* silk, reverse engineer the cocoon, and use an aqueous silk fibroin solution to manufacture (nano)particles.[68] The overall particle characteristics can be fine-tuned though the selection of various processing conditions, including capillary microdot printing,[199] salting out,[200] polyvinyl alcohol blending,[201] electrospraying,[202] electric field application,[203] supercritical fluid technologies,[204] ionic liquid utilisation[205] and organic solvent desolvation.[69,206,207] For this study, I opted for an organic desolvation method as it is a robust and reproducible method for

producing silk fibroin nanoparticles of uniform size (approximately 100 nm, see Figure 3.7 B) and with long-term stability.[40,68,70] The 100 nm size range is well-suited for exploitation of the steps required for lysosomotropic drug delivery, including the EPR effect[12] for solid tumour accumulation, subsequent endocytic uptake[74] and trafficking through the endocytic machinery of the cell to the lysosomes.[1] Silk fibroin nanoparticles can also be surface decorated with polyethylene glycol (PEG) to reduce particle-protein interactions,[208] thereby reducing clearance by the reticular endothelial system and improving (passive) tumour targeting.

To date, attempts to characterise lysosomotropic drug release from silk fibroin nanoparticles have been conducted by measuring drug release in buffer solutions that mimic the pH of the lysosome (pH 4.5 – 5.5) (reviewed in [68]). Whilst these studies provide a useful indication of the role of pH on drug release, they fail to consider the influence of lysosomal enzymatic activity on drug release, as well as the barrier to drug release created by the lysosomal vesicle. Overall, drug release studies in solution cannot faithfully recapitulate the lysosomal microenvironment; thus, they represent a gross oversimplification of lysosomotropic payload delivery. The aim of this chapter was therefore to address these limitations and to assess the roles of lysosomal pH and enzymatic degradation, both individually and in combination, on (i) drug release from unmodified and PEGylated silk fibroin nanoparticles, and (ii) lysosomotropic drug delivery, by studying doxorubicin delivery to human breast cancer cells at single cell resolution.

3.2. Experimental procedures

3.2.1. Production and characterisation of unmodified and PEGylated silk fibroin nanoparticles

Methods for the production of unmodified and PEGylated silk fibroin nanoparticles and their characterisation using DLS and laser doppler electrophoresis analyses are provided in chapter 2 (sections 2.1 – 2.4).

Nanoparticles were also visualised by SEM to qualitatively measure particle size and verify spherical shape. Unmodified and PEGylated silk fibroin nanoparticles were diluted with ultrapure water to a concentration of 1 mg/mL. The samples were then pipetted onto a silicon wafer and lyophilised overnight. The specimens were sputter-coated with carbon using a vacuum coater (Polaron Division E6100, Bio-Rad, Birmingham, UK) and viewed with a FE-SEM SU6600 (Hitachi High Technologies, Krefeld, Germany) at 5 kV and a 40,000-fold magnification.

3.2.2. Fluorescent labelling of unmodified and PEGylated silk fibroin nanoparticles

The standard method for labelling unmodified silk fibroin nanoparticles with AF488® was covered in section 2.5. In this chapter, PEGylated silk fibroin nanoparticles were labelled using the same protocol.

The mean fluorescence intensities of AF488-conjugated PEGylated and unmodified silk fibroin nanoparticles were measured with a POLARStar Omega microplate reader to produce a standard curve (Figure 3.1), which was used to normalise nanoparticle-associated fluorescence during the cell studies.

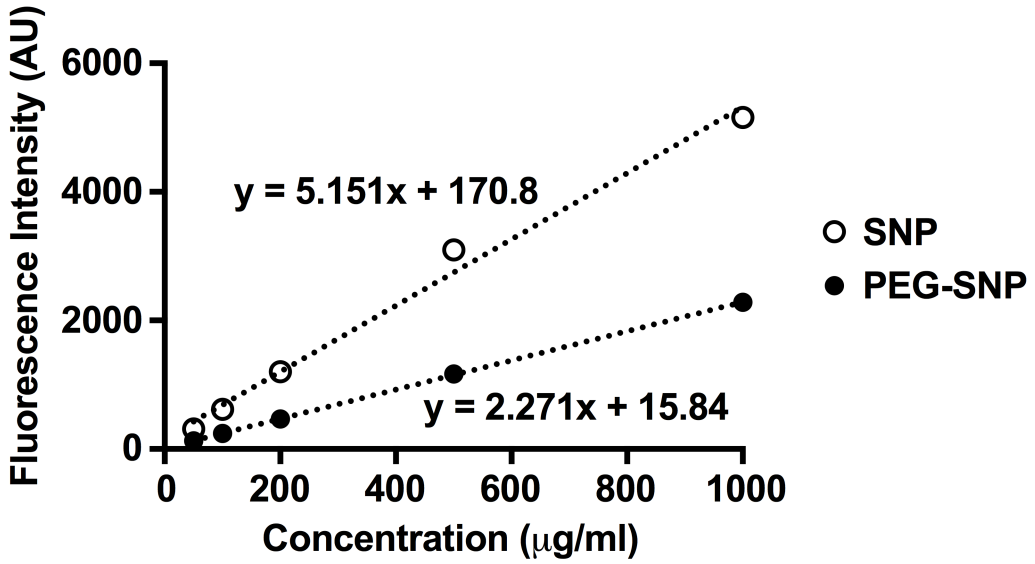

Figure 3.1. Fluorescent standard used to normalise AF488-conjugated unmodified (SNP) and PEGylated (PEG-SNP) silk fibroin nanoparticles. Fluorescence intensities of 50 – 1000 μg/mL unmodified or PEGylated silk fibroin nanoparticles. Equations of lines used to normalise fluorescence values for cell-based studies. (n = 1)

3.2.3. Cell culture

The human breast epithelial cell line MCF-7 was used in this chapter to assess nanoparticle-cell interactions with metastatic cells. Acquisition, culture and maintenance of this cell line has been described in section 2.6.1. In this study, all cells were seeded at a density of 2×10^4 cells/cm^2 and allowed to recover overnight.

3.2.4. Doxorubicin loading of PEGylated and unmodified silk fibroin nanoparticles

Doxorubicin solution (0.2 µmol/mL) was prepared by dissolving 116 µg doxorubicin HCl (LC Laboratories, Boston, MA, U.S.A.) in 1 mL of ultrapure water. Next, 200 µL of 10 mg of unmodified or PEGylated silk fibroin nanoparticles was mixed with 2 mL of 232 µg doxorubicin. After a 24-hour incubation at room temperature, the samples were centrifuged for 30 minutes at 194,000 × g using a fixed-angel rotor (Beckman Coulter 50.2 Ti, Brea, CA, USA). Doxorubicin-associated fluorescence (excitation/emission: 480 nm/590 nm) in the supernatant was measured using the POLARStar Omega and used to determine the residual drug concentration remaining in solution with the aid of a doxorubicin calibration curve (Figure 3.2).

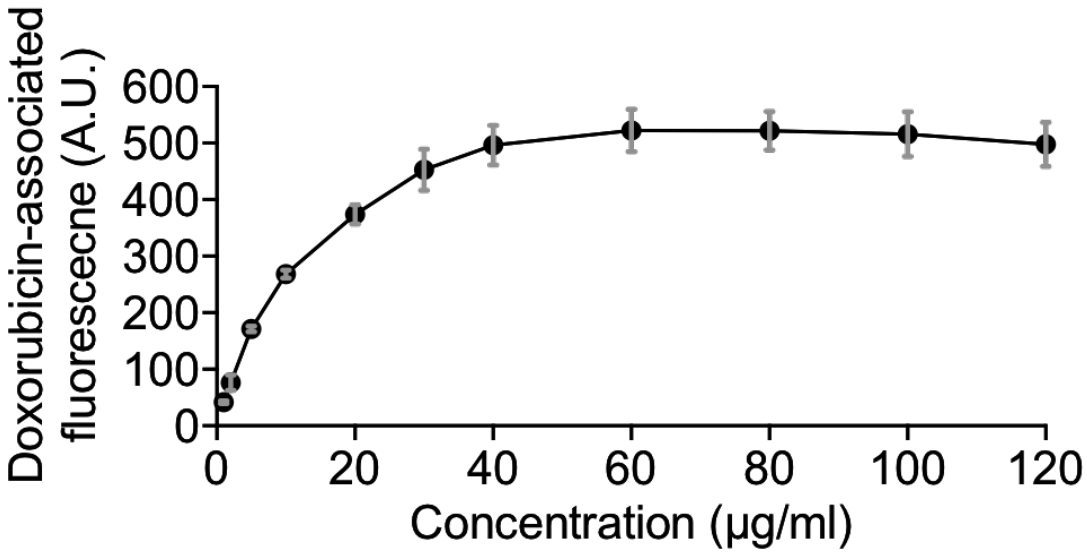

Figure 3.2 Doxorubicin calibration curve. Calibration curve used to determine the residual drug concentration remaining in solution during doxorubicin-loading of unmodified and PEGylated silk fibroin nanoparticles. (n = 3).

3.2.5. Doxorubicin release from unmodified and PEGylated silk fibroin nanoparticles in artificial lysosomal conditions

To measure specific lysosomal effects on drug release from silk fibroin nanoparticles, buffer solutions were used to mimic either the acidity (1 × PBS, pH 5), or the combined acidity and enzymatic activity (1 mg/mL papaïn in 1 × PBS, pH 5) of the lysosome. Papaïn was used in the enzymatic buffer as it is a cysteine protease enzyme which mimics the broad proteolytic activity of lysosomal enzymes.[209,210] Doxorubicin-loaded silk fibroin nanoparticles (unmodified or PEGylated) and unloaded control

nanoparticles were washed twice with ultrapure water and re-suspended in each buffer. The samples were loaded into a 0.1ml Slide-A-Lyzer Mini dialysis device, which was then inserted into a 1.5 mL receiver chamber containing 1.05 mL of buffer at the indicated conditions, followed by incubation at 37°C. At the indicated time points, doxorubicin-associated fluorescence in the receiving chamber was monitored. Fresh buffer was added at each time point to ensure that sink conditions were maintained throughout the study. A calibration curve of doxorubicin in 1 × PBS at pH 5 was used to quantify drug release (Figure 3.3). The percentage of cumulative drug release was determined as a function of the incubation time.

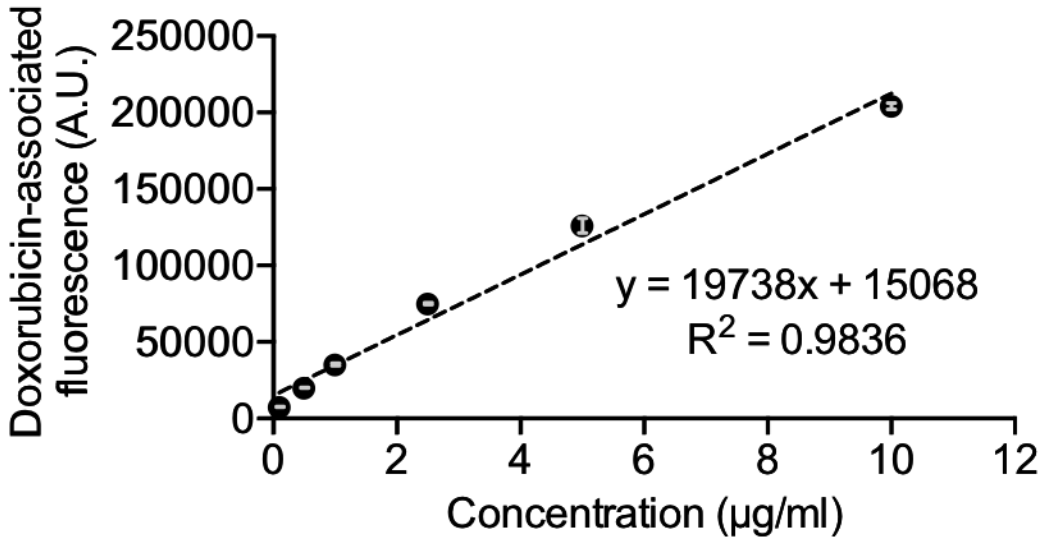

Figure 3.3 Doxorubicin release standard. Standard used to determine the release of doxorubicin from unmodified and PEGylated silk fibroin nanoparticles at pH 5. (n = 3).

3.2.6. Dosing strategy used to analyse uptake and trafficking of AF488 labelled unmodified and PEGylated silk fibroin nanoparticles in MCF-7 cells

For flow cytometry and microscopy analyses, the cells were cultured using complete culture medium but without phenol red. Cells were seeded at 2×10^4 cells/cm^2 and allowed to recover overnight. The cells were then washed three times with 1 × PBS and medium was replaced with either (i) control DMEM or (ii) DMEM supplemented with 0.5 mg/mL unmodified or PEGylated silk fibroin nanoparticles. The cells were incubated for 5 hours in the absence and presence of 50 nM LysoTracker® Red. (Thermo Scientific, Waltham, MA, USA). The incubation was stopped by placing cells on ice, aspirating all the medium and washing three times with ice cold 1 × PBS to remove unbound nanoparticles from the wells. Live cells were then either: (i) trypsinised and collected into 5 ml Falcon tubes for analysis by flow cytometry, or (ii) washed three times with ice cold 1 × PBS and imaged immediately by live confocal microscopy (detailed below).

3.2.7. Flow cytometry

Flow cytometry equipment, data acquisition and data analysis software has been described in section 2.10. The trypsinisation of epithelial cells (such as MCF-7) for flow cytometry has also been described (section 2.10).

In this chapter, all experiments were conducted by recording a minimum of 10,000 events within a gate that was verified to contain live singlets by combining the live cell indicator calcein-AM (Thermo Fisher Scientific, Waltham, MA, U.S.A.) with the exclusion dye propidium iodide (Thermo Fisher Scientific, Waltham, MA, U.S.A.) (Figure 3.4). This was achieved by incubating the cells for 30 minutes with calcein-AM (2 μM), harvesting cells by trypsinisation, washing them three times in 1 × PBS and resuspending them in 1 × PBS containing propidium iodide (3 μM). The geometric mean fluorescence intensities of the cells were measured using the instrument's FITC (530/30 nm) and APC filters (660/20 nm) to identify live cells and cells with membrane damage, respectively. Figure 3.4 shows how the live singlet gate was identified for use in subsequent analyses on cells dosed with unmodified and PEGylated silk fibroin nanoparticles. First, 10,000 ungated events were measured and shown in a traditional FSC-A vs SSC-A flow cytometry dot plot (Figure 3.4 A). Next the cells were plotted based on their FITC-A vs APC-A readings and gated based on their location within the plot (Figure 3.4 B). This revealed 4 gates: (i) FITC-, APC- unstained events (debris), (ii) FITC+, APC- events (live cells), (iii) FITC+, APC+ early apoptotic events (dying cells), (iv) FITC-, APC+ events (dead cells). Finally, events from the live gate were re-plotted as a FCS-A vs SSC-A plot and the singlets were identified within the population (Figure 3.4 C).

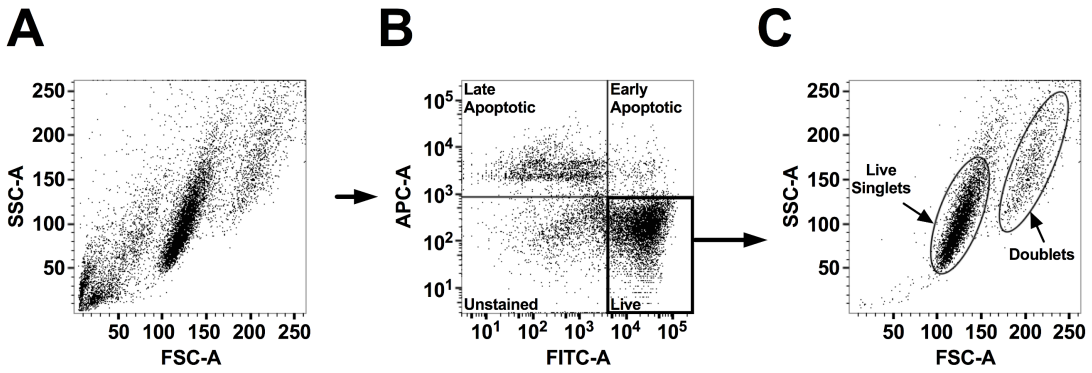

Figure 3.4. Identification of live singlets for flow cytometric analyses. Viability of calcein-AM and propidium iodide stained MCF-7 cells following trypsinisation for flow cytometry. (A) All recorded events plotted on a classical FSC-A vs SSC-A flow cytometry dot plot. (B) Same data with a quadrant gate applied to separate debris, calcein-AM positive live cells, and propidium iodide positive early and late apoptotic cells. (C) All live events plotted on a classical FSC-A vs SSC-A flow cytometry dot plot. Two populations identified as: (i) live singlets, or (ii) doublets.

During data acquisition for nanoparticle treated MCF-7 cells 10,000 gated events were recorded within the live singlet gate identified above. Cell-associated fluorescence was measured using the FITC channel of the instrument to measure changes following interactions with AF488 conjugated unmodified or PEGylated silk fibroin nanoparticles. The differences in raw fluorescence of the particles were accounted for by normalising the data using the fluorescent standard (Figure 3.1).

3.2.8. Inhibition of lysosomal function in live MCF-7 cells

Lysosomal conditions of MCF-7 cells were modulated using chemical inhibitors of lysosomal enzymes (leupeptin) or acidification (ammonium chloride, (NH_4Cl)). Leupeptin and NH_4Cl are well-documented to inhibit lysosomal enzymes and acidification, and they were used in this chapter either separately or in combination to measure the dependence of healthy lysosomal conditions on drug delivery from silk fibroin nanoparticles.

The inhibitory effects of NH_4Cl on lysosomal acidification were verified by adapting the colocalization study (section 2.3.6) to assess signal intensity of LysoTracker® Red, which localises to acidic vesicles (Figure 3.5). This setup enabled differences in the staining of acidic vesicles to be observed in the absence and presence of NH_4Cl.

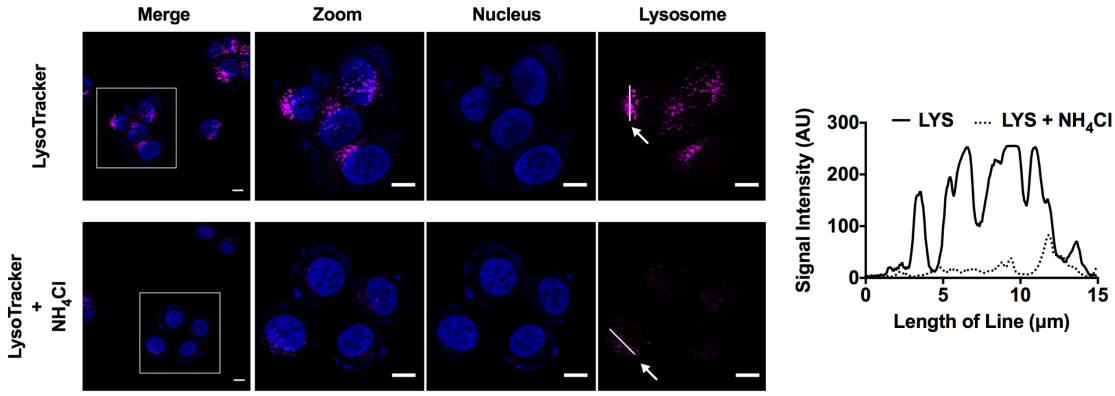

Figure 3.5. NH_4Cl substantially reduces lysosomal acidification in MCF-7 human breast cancer cells. Control MCF-7 cells (top) or MCF-7 cells pre-treated with NH_4Cl for 1 h and then dosed for 5 h with LysoTracker® Red in the absence or presence of NH_4Cl. Profile plot of 15 µm line on lysosomal signal (right) revealed substantial decrease in signal intensity. Scale bars = 10 µm.

3.2.9. Dosing strategy to analyse nuclear localisation of doxorubicin in MCF-7 cells

The effect of lysosomal activity on drug delivery from silk fibroin nanoparticles was determined by measuring the delivery of doxorubicin to the nucleus of MCF-7 cells in the absence and presence of leupeptin and NH_4Cl. MCF-7 cells were seeded at 2×10^4 cells/cm^2 and allowed to recover overnight. Next, cells were washed three times with 1 × PBS and the medium was replaced with either (i) control DMEM or (ii) DMEM supplemented with leupeptin (10 mM) (Sigma-Aldrich, St. Louis, MO, U.S.A), ammonium chloride (NH_4Cl) (10 mM) (Sigma-Aldrich, St. Louis, MO, U.S.A) or a combination of both. Cells were returned to the incubator for 1 hour to allow the inhibitors to take effect.[211] The media were then aspirated and replaced with the same respective inhibitors, together with either (i) 0.3 μg/mL doxorubicin or (ii) 0.5 mg/mL unmodified or PEGylated silk fibroin nanoparticles loaded with an equivalent drug concentration. Cells were incubated at 37 °C for 5 h to allow sufficient time for nuclear delivery of doxorubicin by each formulation, as determined from a previous study.[40] The cells were then placed on ice, washed three times with 1 × PBS, and stained with Hoechst 33342 (1 μg/mL) (Thermo Fisher Scientific, Waltham, MA, USA) for 10 minutes and imaged by confocal microscopy.

3.2.10. Confocal microscopy

Confocal microscopy equipment, data acquisition and data analysis software are detailed in section 2.9.

Localisation of AF488-conjugated unmodified and PEGylated silk fibroin nanoparticles to lysosomes was determined by drawing a 15 μm line through individual cells in multicolour images and plotting the signal intensity of AF488 and LysoTracker® Red along the line. Regions of co-localisation were then identified as peaks on a profile plot.

Lysosomotropic drug delivery was assessed by measuring the association of doxorubicin with nuclei in MCF-7 cells. To achieve this, nuclear (Hoechst) and doxorubicin channels of each image were separated. The individual nuclei were identified (Figure 3.6A, centre) as regions of interest and then applied to the doxorubicin channel (Supplementary Figure 4 A, right). A minimum of six background regions of interest were also identified and the mean fluorescence of background readings, along with selected nuclear areas and integrated densities, were used to determine the nuclear associated fluorescence for individual cells using the equation in Figure 3.6 B.

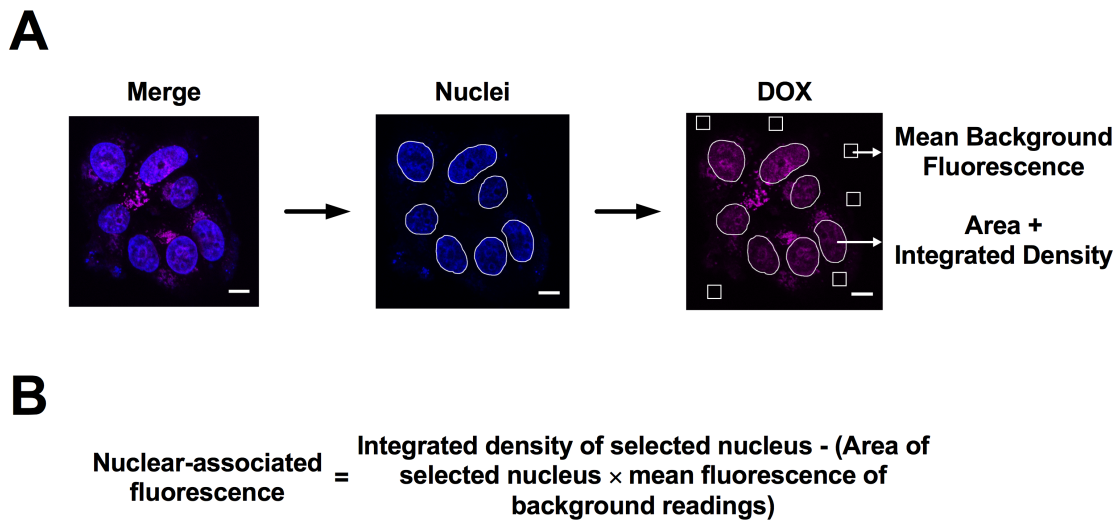

Figure 3.6. Selection of nuclei and analysis of nuclear-associated doxorubicin fluorescence. (A) Nuclear and doxorubicin channels of a multicolour image (left) were split and nuclei identified in the nuclear channel (centre). Regions of interest were applied to the doxorubicin channel and background fluorescence readings were taken. Scale bars = 10 µm. (B) Nuclear area and integrated density were determined, and nuclear-associated fluorescence was calculated for each individual cell.

3.2.11. Statistical analysis

Data were plotted and analysed using GraphPad Prism 7.0a. Sample pairs were analysed with the Student's t test. Multiple samples were evaluated by a two-way analysis of variance (ANOVA) followed by Bonferroni's multiple comparison post hoc test. Asterisks denote statistical significance, as follows: *P < 0.05, **P < 0.01, ***P < 0.001. Unless otherwise stated, data are presented as mean values ± standard deviation (SD) and refer to the number of biological independent experiments.

3.3. Results

3.3.1. Characterisation of unmodified and PEGylated silk fibroin nanoparticles

Unmodified silk fibroin nanoparticles were generated using nanoprecipitation by adding the reverse engineered silk solution dropwise to acetone (Figure 3.7 A). This method yielded a uniform particle size (98.49 ± 3.7 nm with narrow polydispersity 0.095), and negative surface charges (-42.60 ± 0.72 mV) (Figure 3.7 B) (n = 3). Qualitative measurement using SEM verified the size and spherical shape of these nanoparticles (Figure 3.7 A). TsT-activated mPEG was used to decorate the surface of silk fibroin nanoparticles, using previously described methods.[40] Successful surface modification was determined by calculating the amount of surface-grafted PEG and then measuring the particle size and zeta potential. The amount of surface-grafted PEG for 50 mg silk fibroin nanoparticles was 10.72 ± 0.82 mg PEG. PEGylation increased the apparent particle size from 98.49 to 105.30 nm and increased the surface charge from −42.60 to −36.77 mV (Figure 1B). The nanoparticles were then labelled with AF488 or loaded with doxorubicin.

A

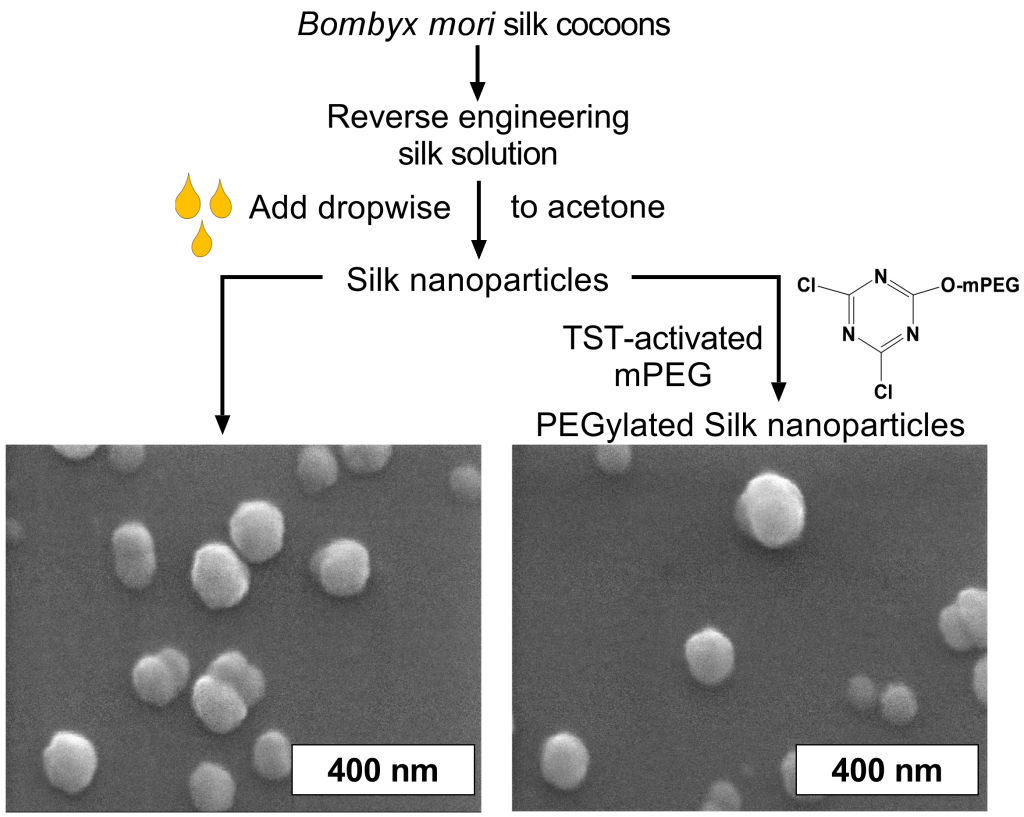

B

Samples	Particle size (nm)	Polydispersity index	Zeta potential (mV)
SNPs	98.49 ± 3.7	0.095 ± 0.01	-42.60 ± 0.72
PEG-SNPs	105.30 ± 3.6	0.087 ± 0.02	-36.77 ± 0.80

Figure 3.7. Manufacture and characterisation of unmodified and PEGylated silk fibroin nanoparticles. (A) Processes for generating unmodified and PEGylated silk fibroin nanoparticles and scanning electron microscopy images of each nanoparticle population. (B) Particle size and zeta potential measurement of unmodified and PEGylated silk fibroin nanoparticles using dynamic light scattering (DLS). (n = 3).

3.3.2. Cellular binding, uptake and trafficking of unmodified and PEGylated silk fibroin nanoparticles

Flow cytometry analyses showed that MCF-7 cells dosed with unmodified silk fibroin nanoparticles displayed a significantly higher cell-associated fluorescence when compared to cells treated with PEGylated silk fibroin nanoparticles (Figure 3.8 A). These differences were also observed using live cell confocal microscopy, and the unmodified silk fibroin nanoparticles were observed to aggregate more readily than the PEGylated silk fibroin nanoparticles (Figure 3.8 B). Analysis of each confocal image revealed similar differences in the normalised cell-associated fluorescence between the unmodified and PEGylated silk fibroin nanoparticles that agreed with the flow cytometry results (Figure 3.8 B, numbers shown on the image). The cells were also dosed in the presence of the lysosomal marker LysoTracker® Red, which confirmed that both unmodified and PEGylated silk fibroin nanoparticles were internalised and trafficked to the lysosomes (Figure 3.8 C).

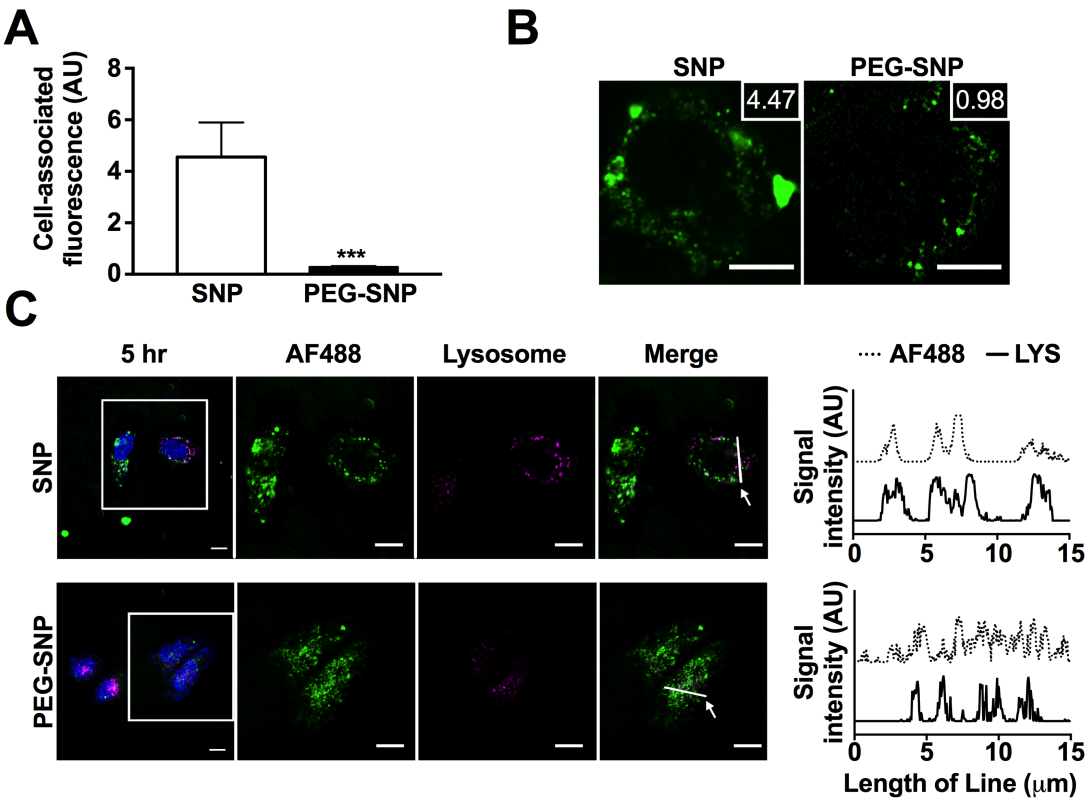

Figure 3.8. Unmodified and PEGylated silk fibroin nanoparticle uptake and lysosomal trafficking. (A) Assessment of cell-associated fluorescence by flow cytometry and (B) live cell confocal imaging of MCF-7 cells treated for 5 h with AF488- conjugated unmodified (SNP) or PEGylated (PEG-SNP) silk fibroin nanoparticles. Boxes (top right) on the images represent the normalised cell-associated fluorescence values. (C) Live cell confocal images of cells dosed for 5 h with LysoTracker® Red, together with either AF488-conjugated SNPs or PEG-SNPs. Arrowheads identify the location of the 15 μm line used in profile plots to highlight the lysosomal regions of co-localisation. Representative images of single confocal slices. Scale bars = 10 μm. (n = 3).

3.3.3. *In vitro* drug loading and release under conditions mimicking the lysosomal environment

The unmodified and PEGylated silk fibroin nanoparticles had loading efficiencies of 98.3 % ± 0.13 and 97.91% ± 0.08, respectively, when exposed to 232 µg doxorubicin (Figure 3.9 A). This was determined using the equation:

$$\text{Loading efficiency (\%)} = \frac{\text{amount of drug in nanoparticles}}{\text{amount of drug initially added}} \times 100$$

The respective zeta potentials of the doxorubicin-loaded unmodified and PEGylated silk fibroin nanoparticles were significantly reduced, by 10% and 20%, respectively, when compared to unloaded controls (Figure 3.9 B). Doxorubicin release by unmodified and PEGylated silk fibroin nanoparticles was measured in 1 × PBS at pH 5 in the absence and presence of papaïn to mimic lysosomal conditions. In the absence of papaïn, pH alone was sufficient to liberate doxorubicin from both unmodified and PEGylated silk fibroin nanoparticles, but the PEGylated silk fibroin nanoparticles displayed a 4-fold increase in doxorubicin release when compared to their unmodified counterparts (Figure 3.9 C, D). The addition of papaïn enhanced the doxorubicin release from both unmodified and PEGylated silk fibroin nanoparticles (Figure 3.9 C, D). Overall, PEGylated silk fibroin nanoparticles had a higher cumulative release than unmodified silk fibroin nanoparticles in both conditions at all time points.

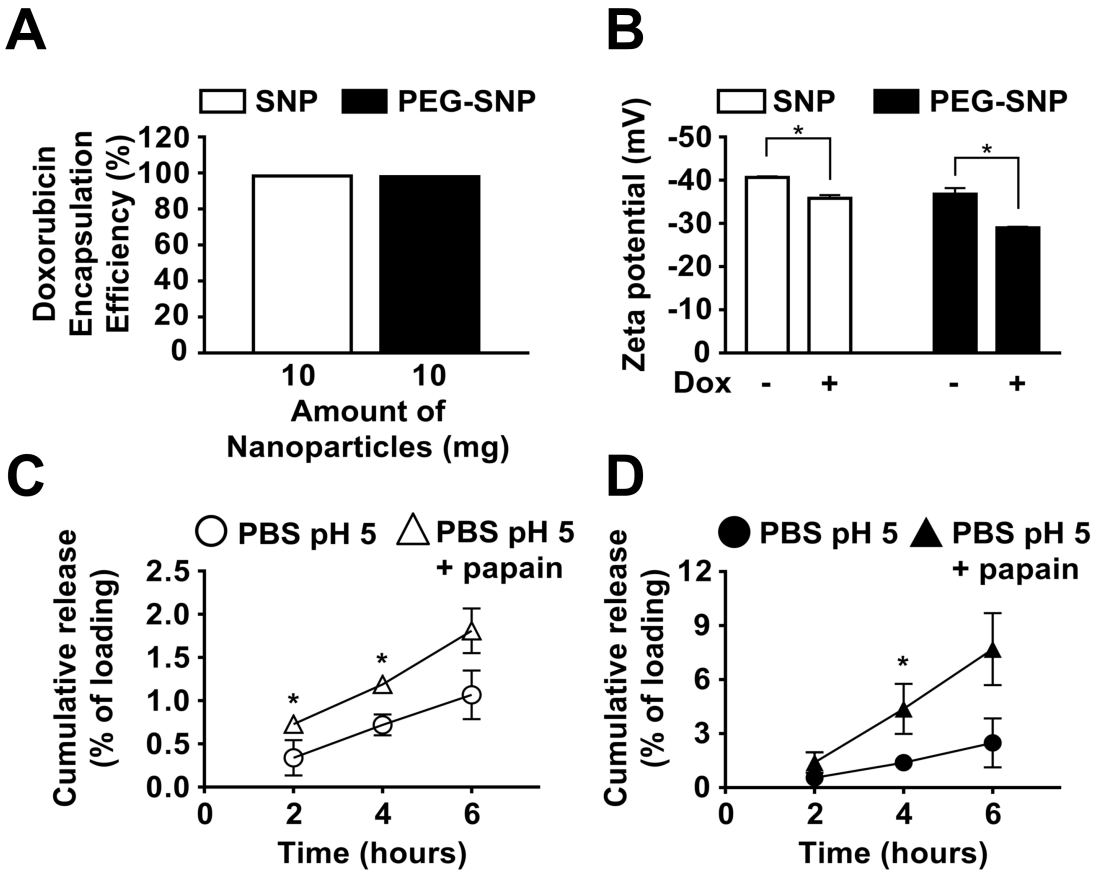

Figure 3.9. Characterisation and drug release from unmodified and PEGylated silk fibroin nanoparticles. (A) Doxorubicin encapsulation efficiency for 10 mg of unmodified and PEGylated silk fibroin nanoparticles. (B) Zeta potential (mV) of doxorubicin loaded silk fibroin nanoparticles compared to unloaded controls. Cumulative doxorubicin release from (C) unmodified and (D) PEGylated silk fibroin nanoparticles in 1 × PBS at pH 5 in the presence and absence of 1 mg/mL papaïn. Data are the means of 3 independent experiments ± SD; error bars are hidden in the plot-symbol when not visible.

3.3.4. Unmodified and PEGylated silk fibroin nanoparticles facilitate lysosomotropic anticancer drug delivery

The model system using 1 × PBS pH 5 and papaïn suggested that enzymes were important for drug release from silk fibroin nanoparticles (Figure 3.9 C, D). Therefore, the role of lysosomal acidification and proteolytic lysosomal enzymes for silk-mediated lysosomotropic drug delivery was further assessed in human breast cancer cells at single cell resolution. This was achieved by measuring the doxorubicin-associated nuclear fluorescence following dosing with doxorubicin-loaded unmodified or PEGylated silk fibroin nanoparticles for 5 hours or with freely diffusible doxorubicin at the equivalent dose (serving as the control). Established inhibitors of lysosomal enzymatic activity (leupeptin)[211] and acidification (NH_4Cl)[211,212] were used, either alone or in combination, to assess their impact on doxorubicin-associated nuclear fluorescence (Figure 3.10A).

Doxorubicin delivery by unmodified silk fibroin nanoparticles displayed a significant reliance on both lysosomal enzyme activity and pH, as total nuclear-associated fluorescence decreased by 17% and 36%, in the presence of the respective inhibitors (Figure 3.10 B, left). Drug delivery by PEGylated silk fibroin nanoparticles was significantly reduced by inhibitor treatment; lysosomal enzymatic activity and acidification resulted in 12% and 20% reductions in nuclear-associated doxorubicin fluorescence, respectively (Figure 3.10 B, centre). Combination treatments with leupeptin and NH_4Cl reduced the nuclear-associated fluorescence by 42% and 33% for unmodified and PEGylated silk fibroin nanoparticles, respectively.

The same cell model was then used to determine the differences in nuclear localisation of freely diffusible doxorubicin (Figure 3.10 B, right). Inhibition of lysosomal enzymatic activity had no significant effect on doxorubicin-associated nuclear fluorescence. However, acidification reduced the nuclear-associated doxorubicin fluorescence by 11%. The combined inhibition of both pH and enzymatic activity resulted in a 22% reduction in nuclear-associated fluorescence (Figure 3.10 B, right).

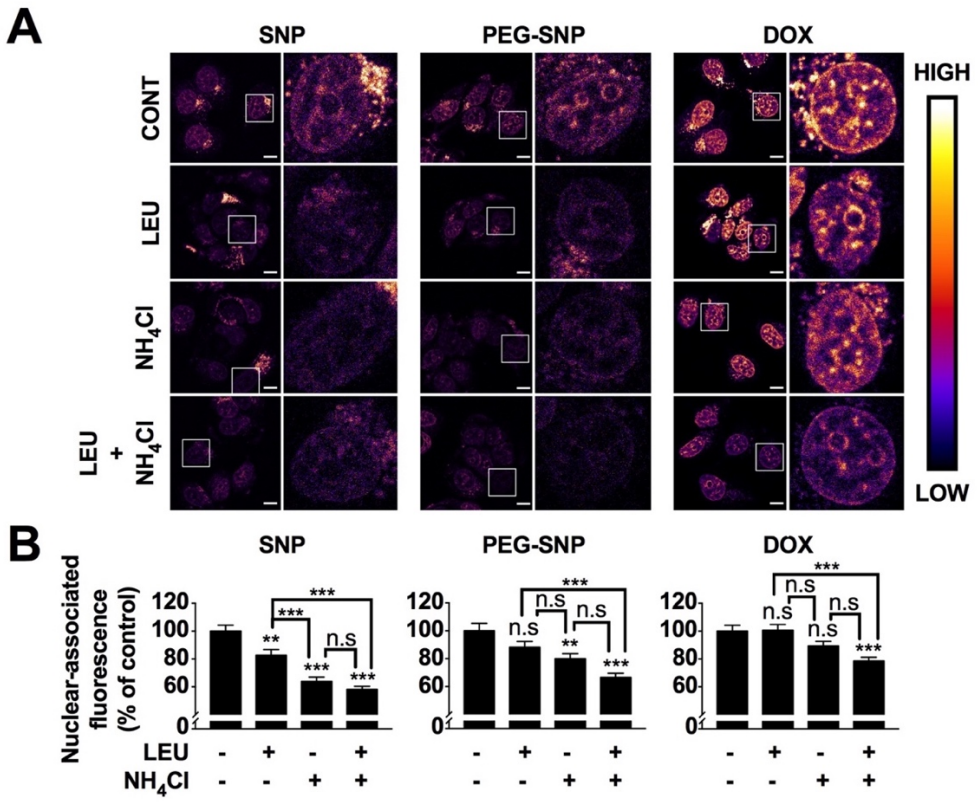

Figure 3.10. Lysosomal enzyme degradation and acidification play a significant role in facilitating nuclear delivery of doxorubicin by unmodified and PEGylated silk fibroin nanoparticles. (A) Representative live confocal microscopy images showing the role of lysosomal enzymes and acidification on doxorubicin delivery mediated by unmodified (SNP) and PEGylated (PEG-SNP) silk fibroin nanoparticles; freely diffusible doxorubicin at the equivalent dose (DOX) served as a control. Note doxorubicin is inherently autofluorescent. Images are single confocal slices, scale bars = 10 μm. (B) Nuclear-associated fluorescence of MCF-7 cells treated for 5 h with freely diffusible doxorubicin or doxorubicin-loaded unmodified or PEGylated silk fibroin nanoparticles in the absence (n = 106 to 132) or presence of (i) leupeptin (LEU) (n = 95 to 152), (ii) NH_4Cl (n = 103 to 144) or (iii) a combination treatment (n = 115 to 156). Data from two independent experiments (n = 2) ± standard error of the mean.

3.4. Discussion

Silk is increasing in popularity as a biomaterial for drug delivery, as confirmed by the current availability of several silk-based formulations, including tablets,[213] hydrogels,[62,214] scaffolds, [215] films,[216] and particles.[68,70,206,207] These advancements are supported by the decades of extensive clinical experience with the use of silk in humans in load-bearing applications (e.g. sutures and surgical meshes).[41,217] Its hierarchical structure endows silk with unique mechanical properties in its unmodified fibre format; these properties arise predominantly from the block copolymer arrangement of crystalline and amorphous segments within the silk heavy chain.[68] In addition, liquid silk, as stored in the silk gland or reverse engineered, adopts a micellar conformation in solution, which current silk fibroin nanoparticle manufacturing protocols now exploit, typically by inducing β-sheets within the crystalline domains to generate physically crosslinked nanoparticles with exquisite stability.[68]

The silk nanocrystalline regions provide a number of unique advantages for drug delivery: they exert a buffering action, tailor water content at the nanoscale, provide physical protection and reduce payload mobility (thereby improving the stability of peptide and protein drugs).[198] Silk fibroin nanoparticles can also be modified in several ways; for example, by surface decoration with PEG, which improves stability in biological buffer systems and eliminates cytokine release from macrophages,[40] or by inclusion of ultra-small Fe_3O_4 nanoparticles during silk fibroin nanoparticle manufacture to yield magnetic field responsive silk fibroin nanoparticles with enhanced *in vivo* solid tumour targeting[218] via the EPR effect.

Emerging evidence now supports the use of silk fibroin nanoparticles (approximately 100 nm in size) for anticancer drug delivery by third order targeting.[68] For example, drug release from silk fibroin nanoparticles has been shown to be pH-sensitive (with model buffers of different pH), and there is evidence that silk fibroin nanoparticles are internalised and trafficked to the lysosomes of human breast cancer cells.[69] However, this means that drug release studies from silk fibroin nanoparticles must also consider the influence of carrier degradation by lysosomal enzymes on drug release. For this reason, I set out to examine the effects of lysosomal enzyme activity on drug release, using a combination of *in vitro* and cell-based models.

A well-characterised nanoprecipitation method was used to generate unmodified and PEGylated silk fibroin nanoparticles of a similar uniform size and charge (Figure 3.7 B) to those documented in the literature.[40,69,70] The unmodified and PEGylated silk fibroin nanoparticles were both readily endocytosed by MCF-7 cells over the 5 hour incubation period, with no apparent differences in lysosomal trafficking (Figure 3.10 C). Doxorubicin was selected as model drug for loading both unmodified and PEGylated silk fibroin nanoparticles because: (i) it is a clinically relevant anticancer drug, (ii) its site of action is the nucleus, making it ideally suited for monitoring lysosomotropic drug delivery, (iii) its intracellular distribution is well documented, and (iv) its intracellular distribution in single live cells is readily tracked by fluorescence microscopy.

Drug loading and the subsequent changes in zeta potential of unmodified and PEGylated silk fibroin nanoparticles (Figure 3.7 A, B) correlated well with previously published studies (e.g. [70]). Furthermore, doxorubicin was released from unmodified

and PEGylated silk fibroin nanoparticles in acidic conditions and this supports existing evidence that drug release is highly pH-dependent (pH 4.5 >> 6.5 > 7.4,).[69] This study further mimicked the lysosomal-like environment by including papaïn, a cysteine protease enzyme. The structure and enzymatic properties of papaïn have high similarity to mammalian lysosomal enzymes (e.g. cathepsins B, H, L, S),[209] and so it is aptly suited to inform on lysosomal degradation. Doxorubicin was liberated more rapidly from the PEGylated silk fibroin nanoparticles than from unmodified silk fibroin nanoparticles at low pH, in both the presence and absence of papaïn. These differences in doxorubicin release from unmodified and PEGylated silk fibroin nanoparticles are expected however, because PEGylation changes the zeta potential of silk fibroin nanoparticles (for a detailed discussion see [40]). The inclusion of papaïn did not significantly affect the liberation of doxorubicin from PEGylated silk fibroin nanoparticles in the first 2 hours (Figure 3.9 D), whereas the unmodified silk fibroin nanoparticles already showed significant increases in doxorubicin release in the first 2 hours in the presence of papaïn (Figure 3.9 C). This suggests that PEGylation confers some early protection against lysosomal enzyme degradation of the silk fibroin nanoparticles, with the end result being a delay in the time taken to trigger doxorubicin release. Overall, the ability of papaïn to increase doxorubicin release from protein nanoparticles is expected. For example, previous work using silica nanoparticles coated with sericin (derived from *Bombyx mori* cocoons) showed that the presence of papaïn increased doxorubicin release two fold. [219]

Next, lysosomotropic delivery of doxorubicin into human breast cancer cells was examined using unmodified and PEGylated silk fibroin nanoparticles. Localisation of doxorubicin to the nucleus was selected as the marker for successful lysosomotropic

drug delivery. Leupeptin and NH_4Cl were selected as well-established inhibitors to assess the role of lysosomal enzymatic activity and acidification, respectively [211]. For the lysosomotropic delivery of doxorubicin to the nucleus; these inhibitors, both individually and in combination, are widely used for *in vitro* assessment of nanomedicine performance (e.g. [219]). In the present study, treatment with leupeptin and NH_4Cl resulted in notable decreases in the nuclear-associated fluorescence of MCF-7 cells when compared to control cells dosed in the absence of the inhibitors (Figure 3.10A). Analysis of nuclear-associated fluorescence of single cells showed a slightly higher dependence on enzymatic degradation for the unmodified silk fibroin nanoparticles than for the PEGylated silk fibroin nanoparticles (Figure 3.10B), in agreement with the results from our papaïn study (Figure 3.9 C, D). Overall, a larger role was indicated for lysosomal acidification alone than for lysosomal enzymatic activity alone in facilitating the nuclear localisation of doxorubicin in both nanoparticles. One plausible explanation for this is that drug release due to enzymatic degradation is comparatively slower[211] than pH-dependent drug release due to the time required for enzymatic degradation of the solid silk fibroin nanoparticle to liberate the drug.

The greatest changes in lysosomotropic drug delivery for either the unmodified or the PEGylated silk fibroin nanoparticles were seen following simultaneous manipulation of both the pH and the proteolytic lysosomal environment (Figure 4B). This suggests that doxorubicin release from silk fibroin nanoparticles in live cells is mediated by both pH and proteolytic enzymes. However, the relative importance of each is difficult to unravel because the low pH in lysosomes contributes to “acid-trapping” of the weakly basic doxorubicin within the lysosomes [220] , while an increase in intracellular

pH modifies the transmembrane and intracellular partitioning of doxorubicin.[221] Furthermore, optimal lysosomal enzyme activity is also pH dependent,[222] and modulation of lysosomal pH may have had effects on overall intracellular trafficking.

3.5. Conclusions

Unmodified and PEGylated silk fibroin nanoparticles loaded with doxorubicin were trafficked to lysosomes of living cells. Once there, a combination of lysosomal pH and enzymatic degradation facilitated doxorubicin release and the relocalisation of the drug to the nucleus. These results demonstrate the importance of both pH and lysosomal enzyme activity on drug release from silk fibroin nanoparticles and provide the first experimental proof of lysosomotropic drug delivery in live cells using these nanoparticles.

Chapter 4: PEGylation-dependent metabolic rewiring of macrophages with silk fibroin nanoparticles

This chapter assessed the ability of silk fibroin nanoparticles to polarise macrophages. Metabolomic analyses and cell-based assays showed that silk fibroin nanoparticles could drive macrophage polarization towards an M1-like phenotype. Silk fibroin nanoparticles performed similarly to PLGA and silica nanoparticles of a similar size, and the immunomodulatory influence of silk fibroin nanoparticles was shown to be reversed by particle PEGylation.

The results in Figure 4.5 of this chapter were published as an original article (Saborano, Wongpinyochit, Totten, Johnston, Seib and Duarte. 2017. Adv. Healthc. Mater. 6, 1601240)[184] and provide a background to the extended results presented in the chapter. This was part of a collaborative research effort and my contributions included cell culture, flow cytometric analyses and preparation of the resulting data. The remaining results in the chapter were produced during a follow-up study (Totten *et al.* 2019. ACS Appl. Mater. Interfaces. in press).[223] I was the first author of this publication and conducted all cell culture-related studies, confocal microscopy and DLS characterisation. All NMR acquisition and analysis was conducted by Duarte *et al.* The manuscript was written by myself with input from the other authors.

4.1. Introduction

The clinical approval of Abraxane in 2005 for the treatment of solid breast tumours was followed by a surge in the use of novel materials in the design of intravenous anticancer nanoparticles that target tumours. Drug-loaded nanoparticles can enter tumour tissues either passively, using the enhanced permeability and retention (EPR) effect,[16] or actively, using targeting moieties such as peptides, monoclonal antibodies, or aptamers.[105,224] The physicochemical properties of nanoparticles therefore have a direct impact on their biological performance at the systemic, tissue, cellular, and subcellular levels.[129,225] Factors such as the particle size, shape, or chemical composition dictate the likelihood of undesirable nanoparticle interactions with complement proteins and immunoglobulins in the circulating blood and with extracellular matrix (ECM) proteins. These interactions then lead to rapid (<1 min)

protein corona formation,[226] opsonization of the particle, and clearance of the nanoparticles by professional macrophages of the mononuclear phagocytic system or by tumour-associated macrophages.[17] This undesired clearance can be circumvented by conjugation of PEG to the nanoparticles. These types of conjugation have become standard practice to allow drug-loaded nanoparticles to evade macrophage detection, thereby maximizing therapeutic payload delivery to the tumour site.[130]

Macrophages are versatile innate immune cells and their processing of foreign materials (including nano-sized drug carriers) plays an essential role in the initiation and coordination of inflammatory or anti-inflammatory immune responses.[227] Until recently, the phagocytosis of nanomedicines was viewed as an undesirable event due to the risks of inducing drug hypersensitivity reactions.[228] However, interest is now growing in the immunomodulatory potential of novel nanomaterials as immunological adjuvants that can influence site-specific inflammation, particularly with regard to the tumour microenvironment.[229] The aim of this chapter was to employ *in vitro* techniques to assess the immunomodulatory potential of silk fibroin nanoparticles and provide actionable data to predict their immunological outcome.

Traditional immunoassays for cell surface markers and cytokine expression represent the gold standard for measuring immune phenotype. However, immunometabolism is now also being recognised as an indicator of inflammatory state. This chapter proposes the use of immunoassays in combination with NMR-based metabolomics to assess macrophage activation state and thereby characterise the immunomodulatory effects of nanomedicines. NMR allows unparalleled analytical reproducibility and imparts the ability to obtain unequivocal structural and quantitative information on molecules,

such as cellular metabolites.[184] The first experimental objective in this chapter was to assess the immunomodulatory performance of silk fibroin nanoparticles to those composed of different materials. PLGA and silica nanoparticles with a similar size range to unmodified silk fibroin nanoparticles (100 – 125 nm) were selected as they are currently in pre-clinical or clinical development for medical applications.[230,231] Therefore these particles are subject to extensive biocompatibility assessment and thus represent an excellent benchmark from which to compare the performance of silk fibroin nanoparticles in an immunomodulatory setting.

Unmodified and PEGylated silk fibroin nanoparticles were then assessed in greater detail to evaluate their immunological response *in vitro*. A dedicated study[223] was conducted into phenotypic and metabolic reprogramming of macrophages using these nanoparticles, and clear objectives were set to evaluate their immunomodulatory potential. First, unmodified and PEGylated silk fibroin nanoparticles were prepared and characterised using dynamic light scattering and SEM imaging. Fluorescent versions of each nanoparticle were also produced. Next, the cytotoxicity of unmodified and PEGylated silk fibroin nanoparticles was measured in RAW 264.7 macrophages using a combination of cell viability assays and qualitative SEM imaging. Live confocal microscopy confirmed lysosomal co-localisation of each nanoparticle formulation at a 24 hour timepoint. Under the same dosing conditions, the phenotypic response of macrophages to unmodified and PEGylated silk fibroin nanoparticles was assessed using *in vitro* assays, whilst NMR metabolomics revealed their metabolic response. Together, these methods provide immunogenicity profiles of unmodified and PEGylated silk fibroin nanoparticles with regard to their immunomodulatory potential in macrophages. This may be useful in the context of anticancer drug delivery

with regard to nanoparticle interactions with tumor-associated macrophages and may help to inform on the therapeutic applications of these nanoparticles.

4.2. Experimental procedures

4.2.1. Preparation, characterisation and fluorescent labelling of unmodified and PEGylated silk fibroin nanoparticles

Methodology outlining the production and characterisation of unmodified and PEGylated silk fibroin nanoparticles was provided in chapter 2 (sections 2.1 – 2.4). The standard method for labelling unmodified silk fibroin nanoparticles with Alexa Fluor 488® was covered in section 2.5. In this chapter, an alternative method of particle was developed to improve the overall fluorescence of PEGylated silk fibroin nanoparticles.

Fluorescent PEGylated silk fibroin nanoparticles were produced by resuspending unmodified silk fibroin nanoparticles (1 mL, 10 mg/mL) in $NaHCO_3$ (1 mL, 0.2 M, pH 8.6), and adding fluorescein PEG succinimidyl ester (250 µL, 30 mg/mL in DMSO). The sample was incubated for 4 h at room temperature in the dark with stirring and then TST-activated mPEG (750 µl, 30 mg/mL) in $NaHCO_3$ (0.2 M, pH 8.6) was added and allowed to react overnight under constant stirring at 4 °C. The resulting FITC-PEGylated silk fibroin nanoparticles were then centrifuged (10,000 × g for 45 minutes), the pellet was washed twice with acidified water (pH 4.6) to remove unbound dye and this was followed by three washes with ultrapure water. The

nanoparticles were stored at 4 °C in the dark until use. A schematic representation of each silk fibroin nanoparticle formulation is provided in Figure 4.1.

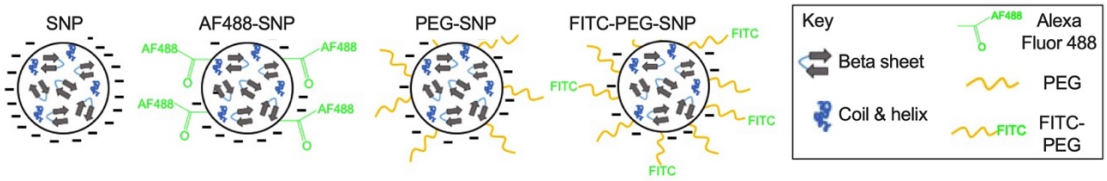

Figure 4.1. Schematic depicting unmodified (SNP), Alexa Fluor 488-labelled (AF488-SNP), PEGylated (PEG-SNP) and FITC-PEGylated (F-PEG-SNP) silk fibroin nanoparticles used to assess the effects of surface modification and concentration dependence during the study.

4.2.2. Cell culture

The mouse macrophage cell line RAW 264.7 was used in this chapter to assess the effects of nanoparticle-cell interactions on macrophage activation state. Acquisition, culture and maintenance of this cell line has been described in section 2.6.4.

4.2.3. Scanning electron microscopy

The nanoparticles were visualised by scanning electron microscopy, as detailed in chapter 3. In brief, unmodified or PEGylated silk fibroin nanoparticles (1 mg/mL) in distilled water were pipetted onto a silicon wafer and lyophilised overnight. The

specimens were sputter coated with a 20 nm layer of gold using an ACE200 low vacuum sputter coater (Leica Microsystems, Wetzlar, Germany) and analysed with an FE-SEM SU6600 (Hitachi High Technologies, Krefeld, Germany) at 5 kV and a 40,000-fold magnification.

RAW 264.7 cells were seeded onto glass coverslips and allowed to recover as detailed above. Cells were exposed to the unmodified or PEGylated silk fibroin nanoparticles for 24 hours (detailed below) and then fixed with 2%v/v glutaraldehyde in 1 × PBS, washed twice with ddH_2O, dehydrated, and critical point dried (EM CPD300, Leica Microsystems, Wetzlar, Germany). Samples were then sputter-coated with gold as detailed above with 15 nm of gold and analysed by SEM at 5 kV with 2,000-fold magnification.

4.2.4. Fourier transform infrared spectroscopy (FTIR)

The secondary silk structures were determined for air-dried silk films, 70%-ethanol–treated silk films, and lyophilised unmodified and PEGylated silk fibroin nanoparticles using Fourier transform infrared (FTIR) spectroscopy (TENSOR II FTIR spectrometer, Bruker Optik GmbH, Ettlingen, Germany), as detailed elsewhere.[40] Briefly, the samples were subjected to 128 scans at a 4 cm^{-1} resolution over the wavenumber range of 400 to 4000 cm^{-1}. The amide I region was identified: 1605−1615 cm^{-1} as side chain/aggregated strands, 1616−1637 cm^{-1} and 1697−1703 cm^{-1} as beta-sheet structure, 1638−1655 cm−1 as random coil structure, 1656−1662 cm^{-1} as alpha-helical bands, and 1663−1696 cm^{-1} as turns.[232]

4.2.5. Uptake and trafficking of unmodified and PEGylated silk fibroin nanoparticles

RAW 264.7 cells were seeded at 3×10^4 cells/cm^2 in complete DMEM without phenol red. For co-localisation experiments, fluorescently labelled silk fibroin nanoparticles were used. The cells were washed three times with 1 × PBS and the culture medium was replaced with either (i) control DMEM or (ii) DMEM supplemented with unmodified or PEGylated silk fibroin nanoparticles at either 0.1 or 0.5 mg/mL. Cells were incubated for 24 hours in total, with LysoTracker Red (50 nM in complete growth medium) added in the final 2 hours of the experiment. The incubation was stopped by placing cells on ice, aspirating all the medium, and washing the cells three times with ice cold 1 × PBS to remove unbound nanoparticles from the wells. Live cells were then stained with Hoechst 33342 (1 μg/mL in serum free medium) (Thermo Scientific, Waltham, MA, U.S.A.) for 10 min, washed three times with ice cold 1 × PBS, and imaged immediately by live confocal microscopy.

4.2.6. Calculation of co-localisation coefficients

Co-localisation between nanoparticles and lysosomes was determined on representative confocal images using the JACoP ImageJ plug-in to calculate the Manders overlap coefficients for green (nanoparticle) and magenta (lysosome) channels. The Manders coefficient ranges from 0 – 1 and indicates the degree of co-localization between two channels.[233,234] The default JACoP algorithm was used on threshold adjusted images to calculate Manders coefficients for each treatment group.

4.2.7. Flow cytometry

Flow cytometry equipment, data acquisition and data analysis software has been described in section 2.10. The preparation of RAW 264.7 macrophages using a scraping method has also been described (section 2.10).

RAW 264.7 cells were seeded at 3×10^4 cells/cm^2 in complete DMEM without phenol red. Next, cultures were incubated with silk, silica or PLGA nanoparticles (0.5 mg/mL) for 24 h and cells were collected by scraping. Tubes were centrifuged and placed on ice and the supernatant was discarded. Cells were then resuspended in either (i) control cell staining buffer (1 × PBS, 1% BSA), or (ii) cell staining buffer containing AF488 labelled anti-mouse CD80 (Biolegend, San Diego, CA, USA, Clone 16-10A1) or AF488 labelled Armenian hamster IgG isotype control (Biolegend, Clone HTK888) for 20 minutes in the dark. Cells were then washed three times in cell staining buffer by centrifugation and resuspended in cell staining buffer prior to data acquisition on the flow cytometer.

4.2.8. MTT cytotoxicity assay

A detailed methodology outlining the principles of the MTT assay and standard protocol used to determine cell viability was provided in chapter 2 (section 2.7).

In this chapter, RAW 264.7 cells were seeded at 3×10^4 cells/cm^2 in complete DMEM and allowed to recover overnight. Next, cells were either left untreated (negative control) or were dosed for 24 hours in complete DMEM supplemented with: (i) 1% v/v Triton X-100 (positive control), (ii) unmodified or PEGylated silk fibroin nanoparticles (0 – 1 mg/mL), or (iii) PEG (5,000 g/mol; Iris Biotech GmbH, Marktredwitz, Germany) (0 – 1 mg/mL). The MTT assay was carried out as outlined in section 2.7 to determine the percentage of cell viability following each treatment. As datasets were normalised to the controls, they have been shown separately in Figure 4.2.

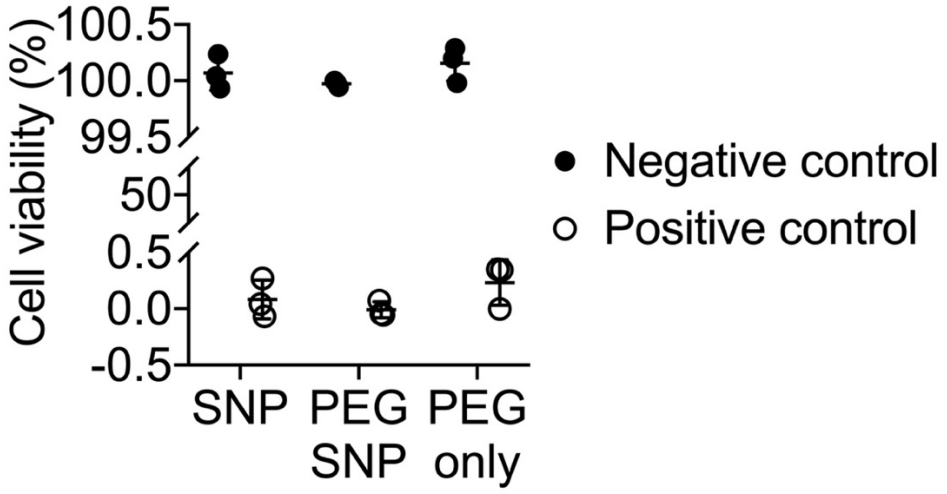

Figure 4.2. Positive and negative controls used to calculate mean cell viability in MTT cytotoxicity assays. (n = 3).

4.2.9. Phenotypic response to unmodified and PEGylated silk fibroin nanoparticles

In this chapter, RAW 264.7 cells were seeded at 3×10^4 cells/cm^2 in complete DMEM and allowed to recover overnight. Next, cells were dosed for 24 hours in complete medium supplemented with low (0.1 mg/mL) or high (0.5 mg/mL) concentrations of either unmodified or PEGylated silk fibroin nanoparticles (macrophages were exposed to silk fibroin nanoparticles without prior priming). The phenotypic response of macrophages to silk fibroin nanoparticles was then measured using a variety of assays. Detailed methodologies outlining the requirements and protocols for the lactate dehydrogenase, antioxidant, ROS, ELISA and Griess assays were provided in chapter 2 (section 2.8).

A 1% v/v Triton X-100 positive control sample was included to assess plasma membrane integrity. However, for TNF-α, nitric oxide production, antioxidant capacity, and reactive oxygen species, a positive control using lipopolysaccharide (1.5 ng/mL) was included instead to provide baseline phenotypic information on RAW 264.7 cells in an activated state. Following the 24 h incubation period, the growth medium was collected, clarified by centrifugation (380 × g for 10 min), transferred to 2 mL low-protein-binding Eppendorf tubes, and stored at −80 °C. The conditioned growth medium samples were assayed to quantitatively monitor plasma membrane integrity (lactate dehydrogenase assay), TNF-α (TNF-α ELISA), and nitric oxide levels (Griess assay). Cell lysates were generated as detailed below to measure antioxidant capacity and reactive oxygen species.

The lactate dehydrogenase assay was performed with a Pierce LDH Cytotoxicity Assay Kit (Thermo Fisher Scientific, Waltham, MA, 244 USA) following the manufacturer's instructions to assess membrane integrity in positive and negative controls, nanoparticle, and LPS treated cells. A mouse TNF-α DuoSet ELISA kit (R&D Systems, Minneapolis, MN, USA) was used to quantify TNF-α levels in a conditioned culture medium. Nitric oxide was measured with the Griess assay as detailed elsewhere.[186,187]

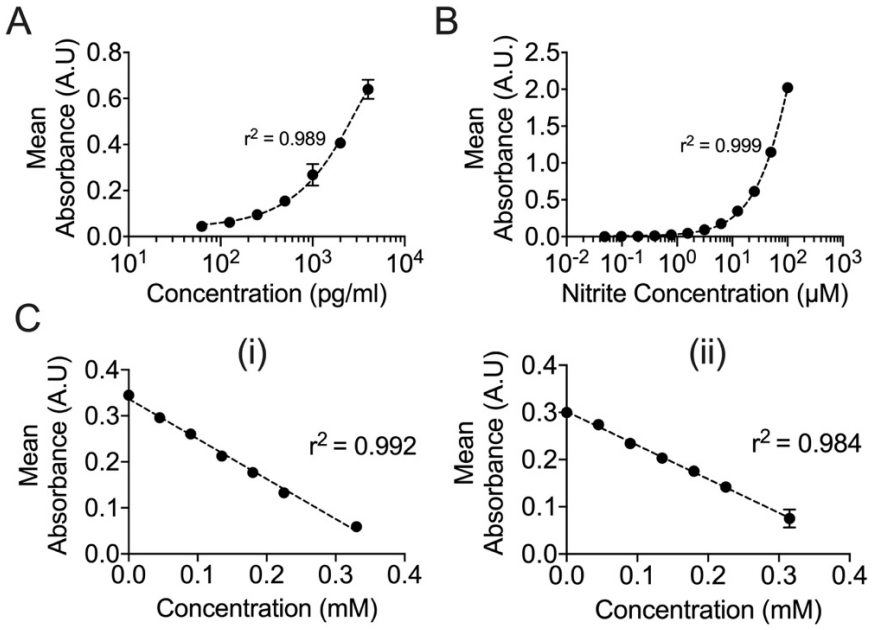

Figure 4.3. Standards used to assay inflammatory phenotype. Standard curves produced for determination of (A) TNF-α and (B) nitric oxide expression in control, nanoparticle and LPS treated samples. Curves fitted using non-linear regression analysis. (C) Standard lines produced for determination of antioxidant concentration expression in control, nanoparticle and LPS treated samples. (i) Straight line used to analyse independent repeats n = 1 and n = 2 (ii) Straight line used to analyse independent repeat n = 3. Lines fitted using linear regression analysis.

4.2.10. Sample collection for metabolomics

For metabolomic studies, RAW 264.7 cells were treated as detailed above. The culture medium was collected, clarified by centrifugation (380 × g for 10 minutes), lyophilised, and stored at -80ºC until further use. Cell extracts were prepared as detailed previously.[184] Briefly, cells were washed 3 times with ice cold 1 × PBS, quenched with methanol (650 µL, 80% v/v; cooled to -20°C), scraped off the dish, and collected in Eppendorf tubes. Next, $CHCl_3$ (260 µL, cooled to - 20°C) was added to each tube and vortexed, followed by addition of $CHCl_3$ (260 µL, cooled to - 20°C) and ddH_2O (220 µL) to each sample. The samples were vortexed, allowed to rest on ice for 10 minutes, and then centrifuged at 2,000 × g for 15 minutes. The aqueous and lipophilic phases were collected; the aqueous sample was dried under a stream of nitrogen, and the organic phase was allowed to evaporate in a fume hood. All samples were stored at -80°C until analysis.

4.2.11. NMR spectroscopy

All NMR analyses were carried out by Duarte *et al.* on cell lysates produced by myself. At the time of NMR analysis, dried samples of cell culture media and aqueous cell extracts were reconstituted in deuterated phosphate buffer (600 µL, 100 mM, pH 7.4) containing 3-(trimethylsilyl)-1-propanesulfonic acid-d6 sodium salt (0.1 mM), whereas lipophilic cell extracts were reconstituted in deuterated chloroform containing 0.03% tetramethylsilane. For NMR analysis, 550 µL of each sample were transferred into 5 mm NMR tubes. NMR spectra were acquired on a Bruker Avance DRX-500

spectrometer operating at 500.13 MHz for ^{1}H observation, at 298 K, using a 5 mm probe. Standard 1D ^{1}H spectra (pulse programs 'noesypr1d', with water suppression, for medium samples/aqueous extracts, and 'zg' for lipophilic extracts) were recorded with a 7002.8 Hz spectral width, 32 k data points, a 2 s relaxation delay, and 512 scans. Spectral processing comprised exponential multiplication with 0.3 Hz line broadening, zero filling to 64 k data points, manual phasing, baseline correction, and chemical shift calibration to the TSP or TMS signal at 0 ppm. Metabolites were identified based on 2D spectra and consultation of spectral reference databases, as detailed previously.[184]

4.2.12. Multivariate analysis and spectral integration of NMR spectra

Multivariate analysis and spectral integration were were carried out by Duarte *et al.* Spectra were exported from Amix-Viewer (version 3.9.14, BrukerBiospin, Rheinstetten, Germany) and normalised by total spectral area (excluding the region comprising the suppressed water signal) to eliminate potential difference due to cell number variations. Principal component analysis and partial least squares discriminant analysis were then applied using SIMCA-P 11.5 software (Umetrics, Umeå, Sweden), with a default seven-fold internal cross validation, from which Q2 and R2 values, reflecting predictive capability and explained variance, respectively, were extracted.

For quantitative analysis of metabolite variations, selected signals in the 1D spectra were integrated using Amix-Viewer (version 3.9.14, BrukerBiospin, Rheinstetten, Germany) and normalised by the total spectral area. For each metabolite, the

percentage variation in nanoparticle-exposed samples was calculated relative to controls, together with the effect size adjusted for small sample numbers and the respective standard errors.[235] The metabolite variations of large magnitude (i.e., with an absolute effect size greater than 0.8)[235] were expressed in a heatmap coloured as a function of % variation using the R-statistical software.

4.2.13. Statistical analyses

Data were plotted and analysed (Figures 1-4) using GraphPad Prism 7.0a. Sample pairs were analysed with the Student's t-test. Multiple samples were evaluated by one-way analysis of variance (ANOVA) between basal and nanoparticle treated groups followed by Bonferroni's multiple comparison post hoc test. Asterisks denote statistical significance, as follows: *p< 0.05, **p< 0.01, ***p< 0.001. Unless otherwise stated, data are presented as mean values ± standard deviation (SD) and refer to the number of independent biological experiments. For statistical analysis of NMR data, see the description above.

4.3. Results

4.3.1. Characterisation of unmodified and PEGylated silk fibroin nanoparticles

The silk fibroin nanoparticles used in this study were quantitatively analysed by dynamic light scattering to verify the particle size and polydispersity index of each preparation using different batches (Figure 4.4 A). The zeta potential of each batch was determined using laser doppler electrophoresis. An increase in particle size was noted between the unmodified silk fibroin nanoparticles (96.0 nm) and the PEGylated and FITC-PEGylated silk fibroin nanoparticles (105.3 nm and 106.4 nm, respectively) (Figure 4.4 A, left). The zeta potential was also significantly influenced by the PEGylation process. In their unmodified state, the silk fibroin nanoparticles had a zeta potential of -47.9 mV. However, this increased to -43.4 mV and -44.0 mV for PEGylated and FITC-PEGylated silk fibroin nanoparticles, respectively (Figure 4.4 A, centre). All three silk fibroin nanoparticle types showed a narrow polydispersity (Figure 4.4 A, right). The FTIR absorbance analyses at 1621 cm^{-1} confirmed a high abundance of beta-sheets within the structures of all three nanoparticle formulations when compared to ethanol-treated silk film controls (Figure 4.4 B). Quantitative measurements were supported by SEM images that confirmed the spherical shape of the unmodified and PEGylated silk fibroin nanoparticles (Figure 4.4 C)

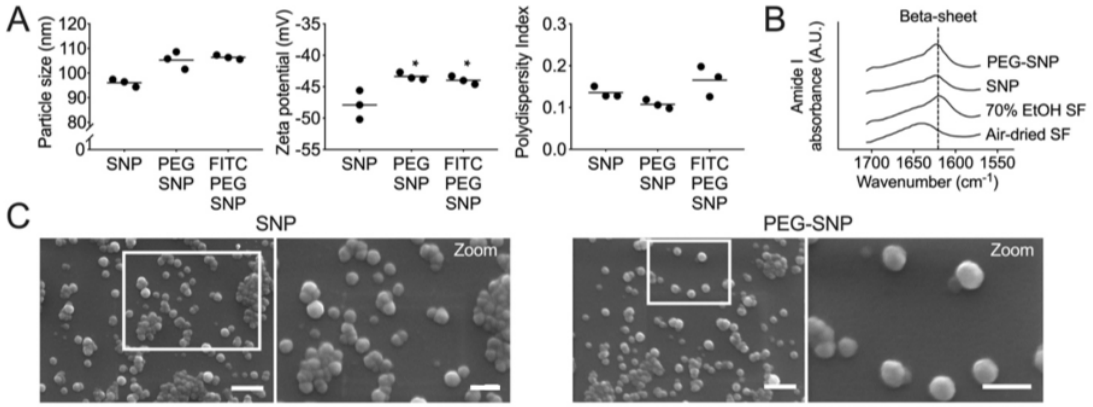

Figure 4.4. Characteristics of unmodified and PEGylated silk fibroin nanoparticles. (A) Particle size distribution, zeta potential and polydispersity indices for unmodified, PEGylated and FITC-PEGylated silk fibroin nanoparticles measured using dynamic light scattering (*, $P<0.05$, one-way ANOVA). (n = 3). (B) FTIR absorbance spectra of unmodified and PEGylated silk fibroin nanoparticles presented alongside 70% ethanol-treated or air-dried silk fibroin films (SF) as reference samples. The dotted line at 1621 cm^{-1} indicates the beta sheet (n = 3). (C) Representative scanning electron images of unmodified and PEGylated silk-fibroin nanoparticles (Scale bars: left = 500 nm; right = 250 nm).

4.3.2. Silk, silica and PLGA nanoparticles induce polarisation of macrophages towards an M1-like state.

During a comparative metabolomic analysis, 24 hour doses with 0.5 mg/mL nanoparticles made from silk, silica and PLGA were shown to modulate macrophage metabolism indicative of an M1-like phenotype.[236,237] To complement these results, the surface expression of CD80 and cytokine production in response nanoparticles was

assessed (Figure 4.5).[227] All nanoparticles induced the plasma membrane expression of CD80, with similar levels observed for silica and silk (25% of CD80 positive cells) and significantly higher levels for PLGA (39% of CD80 positive cells); LPS served as the positive control (> 90% CD80 positive cells). Conditioned cell culture medium from nanoparticle-treated and LPS treated cells showed upregulation of (pro-inflammatory) cytokines (Figure 4.5 C). For example, all nanoparticles and LPS induced substantial increases in IL-ra, CCL3 and CCL4, but the nanoparticles failed to increase GM-CSF, IL10 and IL6 above the detection limit of this assay.

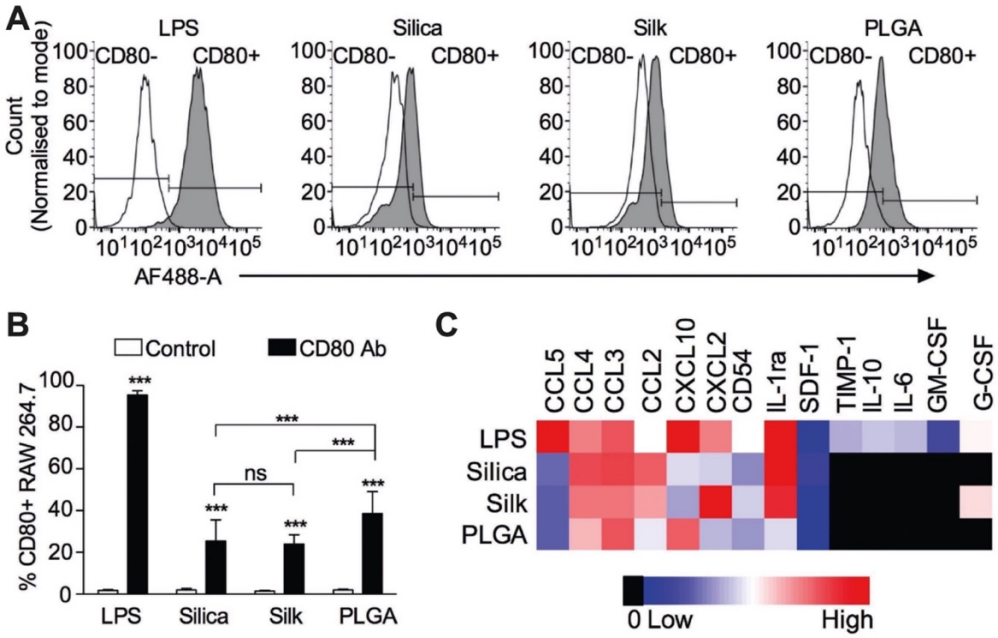

Figure 4.5. All nanoparticles induced an M1-like macrophage phenotype. RAW 264.7 cells dosed for 24 h in the absence or presence of 0.5 mg/mL silica, silk fibroin or PLGA nanoparticles. (A) Plasma membrane expression of CD80, (B) percentage of CD80 positive macrophages, and (C) expression of cytokines in response to stimuli. 1.5 ng/mL LPS served as a positive control. One-way ANOVA with Bonferroni post-hoc test between isotype control and anti-CD80 treated groups, (*** $p < 0.001$). (n = 3).

4.3.3. Interactions of unmodified and PEGylated silk fibroin nanoparticles with macrophages

RAW 264.7 cells were selected as a model mouse macrophage cell line to allow for continuity with the comparative metabolomic analysis.[184] A combination of biochemical *in vitro* assays and NMR metabolomics were used to elucidate silk fibroin nanoparticle-induced shifts in phenotypic and metabolic profiles. First, the cytotoxicity of silk fibroin nanoparticles was assessed. Exposure to unmodified silk fibroin nanoparticles caused a significant reduction in cell viability when compared to untreated controls. However, statistical analysis between cells exposed to unmodified or PEGylated silk fibroin nanoparticles at equivalent concentrations revealed no significant differences in cell viability. The unmodified and PEGylated silk fibroin nanoparticles showed cytotoxicities of less than 15% at exposure levels of up to 100 μg/mL (Figure 4.6 A). At higher concentrations, both particle types reduced cell viability. At the maximum tested concentration, the cell viability was reduced more substantially for the PEGylated silk fibroin nanoparticles than for the unmodified ones; however, the IC_{50} value remained > 1,000 μg/mL (Figure 4.6 A). Parallel experiments that tested the cytotoxicity of water-soluble PEG revealed no significant changes in cell viability over the tested concentration range (Figure 4.7). The macrophage plasma membrane integrity was monitored by lactate dehydrogenase leakage into the culture medium. Exposure of the macrophages to unmodified or PEGylated silk fibroin nanoparticles at either low (0.1 mg/mL) or high (0.5 mg/mL) nanoparticle concentrations caused no leakage of lactate dehydrogenase, indicating no plasma membrane damage (Figure 4.6 B). Qualitative assessment by SEM showed no gross

morphological changes of the macrophages following exposure to the nanoparticles. SEM images of RAW 264.7 macrophages treated at the low nanoparticle concentration showed that the unmodified nanoparticles formed aggregates at cell surface, whereas the PEGylated silk fibroin nanoparticles did not (Figure 4.8).

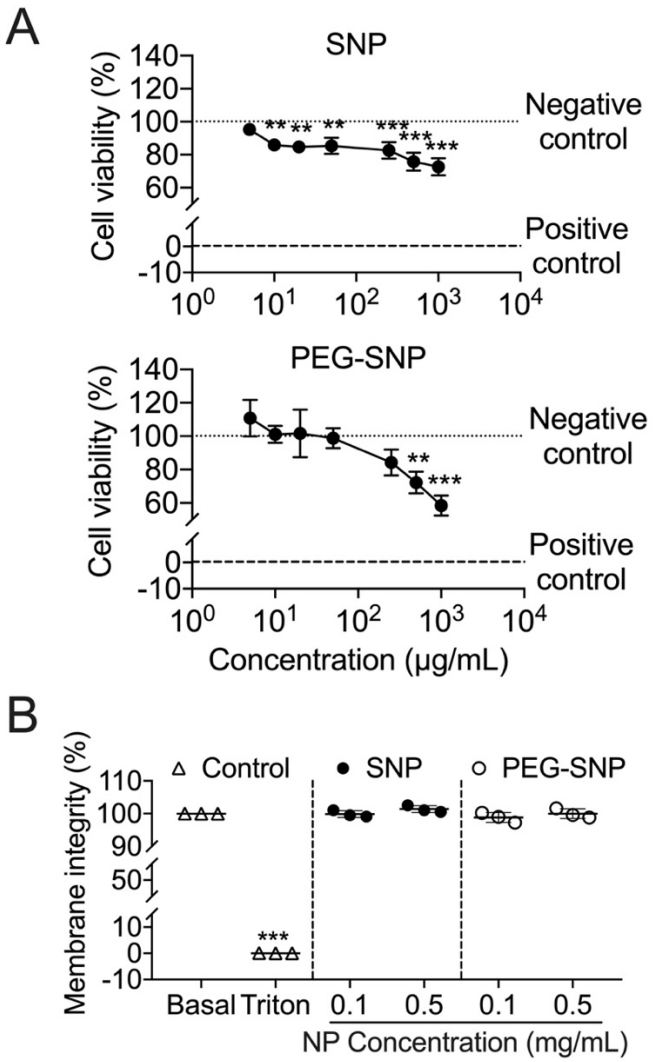

Figure 4.6. Macrophage response towards unmodified and PEGylated silk fibroin nanoparticles. (A) *In vitro* cytotoxicity of unmodified (SNP) and PEGylated (PEG-SNP) silk fibroin nanoparticles to RAW 264.7 cells following a 24 h incubation in complete media supplemented with 0 – 1000 µg/mL nanoparticles (n = 3). (B) Membrane integrity of RAW 264.7 cells following a 24 h incubation in complete media supplemented with 0.1 mg/mL or 0.5 mg/mL unmodified (SNP) or PEGylated (PEG-SNP) silk fibroin nanoparticles (n = 3). One-way ANOVA with Bonferroni post-hoc test between untreated and NP treated groups (**, $P < 0.01$; ***, $P < 0.001$).

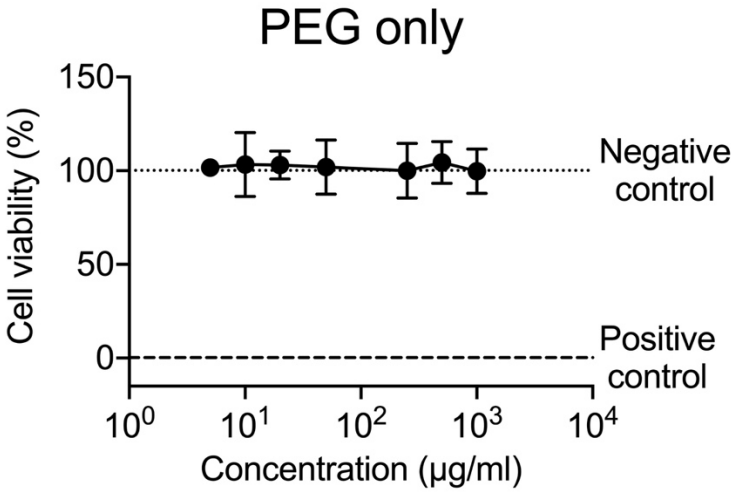

Figure 4.7. *In vitro* cytotoxicity of PEG following a 24-hour incubation in complete media supplemented with a 0 – 1000 µg/mL concentration (n = 3).

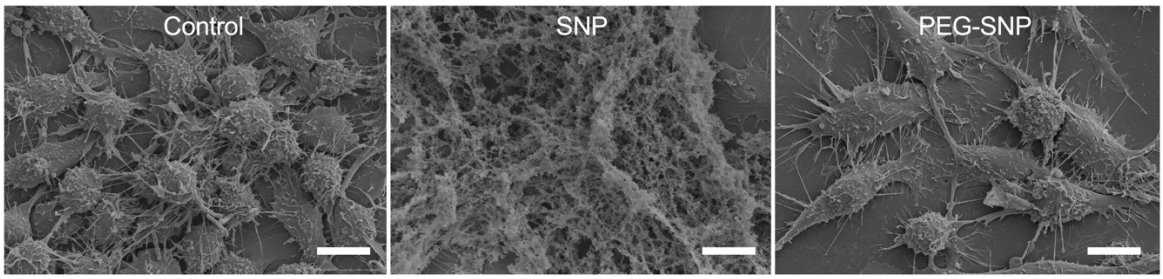

Figure 4.8. Surface interactions between silk fibroin nanoparticles and macrophages. Scanning electron microscope images of RAW 264.7 cells following a 24-hour incubation in complete media supplemented with 0.1 mg/mL unmodified (SNP) or PEGylated (PEG-SNP) silk fibroin nanoparticles. Scale bar = 100 µm.

I also verified whether endocytic uptake might be involved in the observed effects by studying the intracellular fate of the unmodified and PEGylated silk fibroin nanoparticles by live-cell confocal microscopy. Lysotracker Red® was used to label the RAW264.7 cells and nanoparticle accumulation was observed within lysosomes at 24 hours, as evidenced by the substantial co-localisation of the silk fibroin nanoparticles with the lysosomal signals. This co-localisation occurred regardless of particle PEGylation or concentration, as evidenced by the similar Manders coefficients (numbers on the merged images in Figure 4.9). However, the unmodified silk fibroin nanoparticles showed some evidence of aggregation at the cell membrane. This aggregation was reduced, and the lysosomes appeared smaller in the macrophages treated with PEGylated silk fibroin nanoparticles.

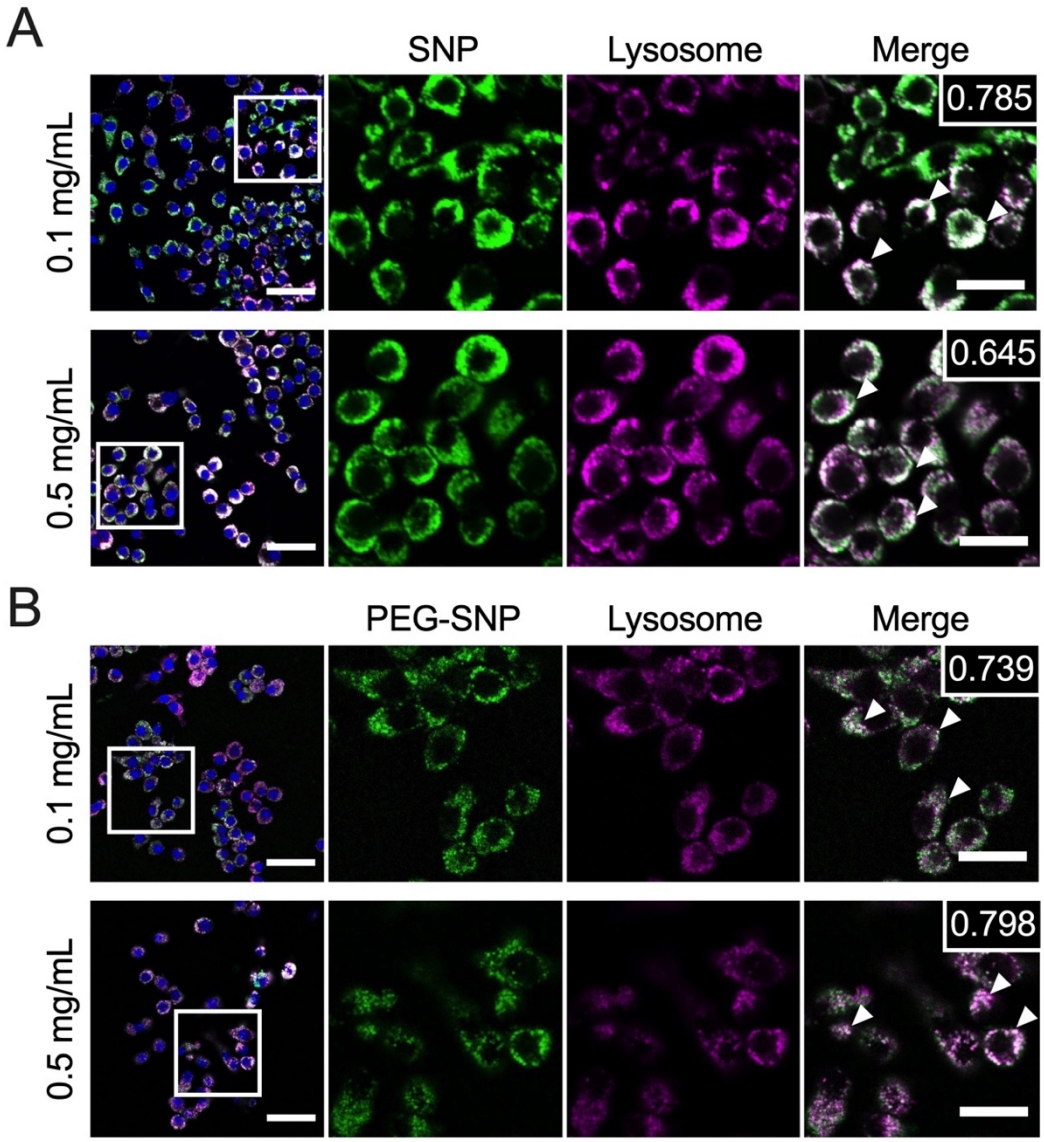

Figure 4.9. Cellular uptake of unmodified and PEGylated silk fibroin nanoparticles. Representative live cell confocal images of RAW264.7 macrophages following a 24 h dose of (A) unmodified (SNP) or (B) PEGylated (PEG-SNP) silk fibroin nanoparticles at concentrations of either (i) 0.1 mg/mL, or (ii) 0.5 mg/mL. (Scale bars: left = 40 μm; right (zoomed) = 20 μm). Numbers on merged images show the Manders coefficients calculated for each treatment group. Arrowheads identify co-localisation between the nanoparticle-associated and lysosomal signals.

4.3.4. Inflammatory response to unmodified and PEGylated silk fibroin nanoparticles

Next, the inflammatory phenotype of RAW264.7 macrophages in response to low and high nanoparticle concentration was determined. Cell exposure to unmodified silk fibroin nanoparticles induced significant TNF-α release at both nanoparticle concentrations (2.20 ng/mL and 1.70 ng/mL, respectively) when compared to basal levels (0.14 ng/mL) (Figure 4.10 A). A milder TNF-α response was observed when macrophages were treated with PEGylated silk fibroin nanoparticles, with only the high concentration causing a significant increase in TNF-α release (1.14 ng/mL). When assessing nitric oxide levels and reactive oxygen species, neither factor was influenced by a low concentration of either unmodified or PEGylated silk fibroin nanoparticles (Figures 4.9 B, C). However, at the high nanoparticle concentration, unmodified silk fibroin nanoparticles significantly increased nitric oxide levels (111%) yet decreased reactive oxygen species levels by 64%. A similar trend was observed with the high PEGylated silk fibroin nanoparticle concentration (55% increase of nitric oxide levels and 44% drop in reactive oxygen species). Total antioxidant capacity in RAW 264.7 increased substantially compared to basal levels following treatment with low and high concentrations of unmodified silk fibroin nanoparticles. However, only minimal changes were observed following treatment with PEGylated silk fibroin nanoparticles (Figure 4.10 D).

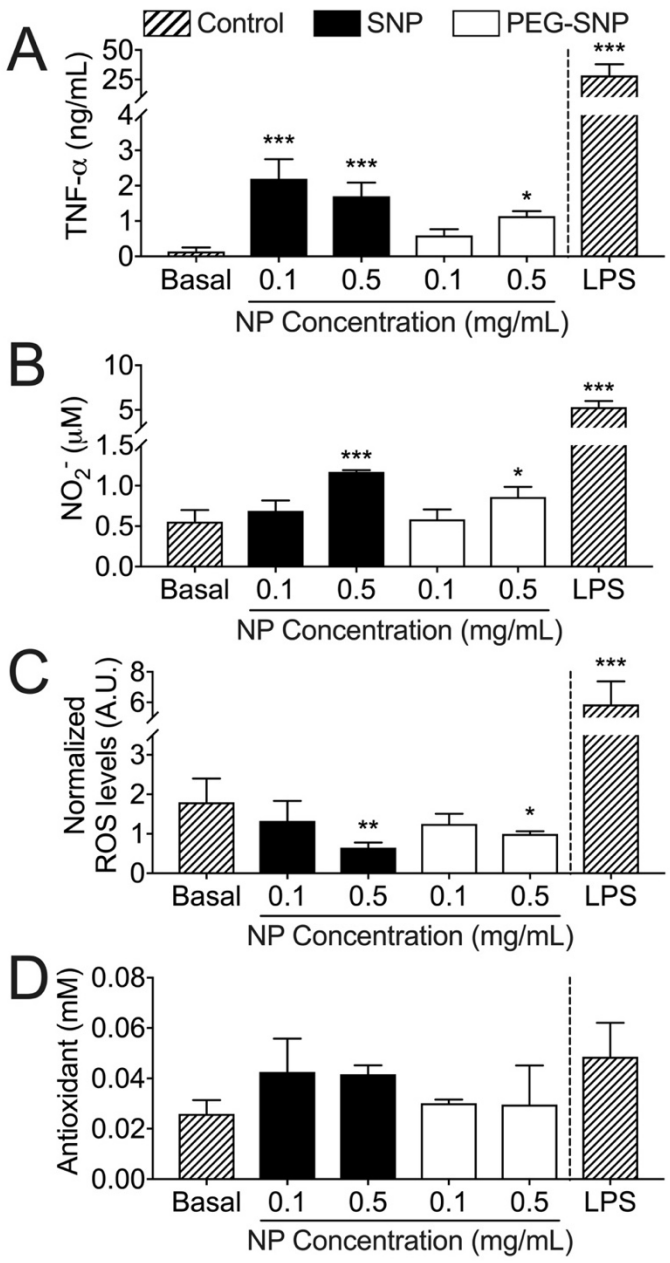

Figure 4.10. Phenotypic changes induced in macrophages exposed to unmodified (SNP) and PEGylated (PEG-SNP) silk-fibroin nanoparticles. (A) TNF-α release, (B) nitrite (NO^-_2) levels, (C) reactive oxygen species (ROS) and (D) total antioxidant capacity from RAW 264.7 macrophages following a 24-hour incubation in complete media supplemented with unmodified or PEGylated silk fibroin nanoparticles (0.1 or 0.5 mg/mL). 1.5 ng/mL LPS served as a positive control. (*, $P < 0.05$; **, $P < 0.01$; ***, $P < 0.001$, A, B and C: $n = 3$, D: $n = 4$)

The cell culture medium was also assayed to further evaluate the cytokine response of RAW264.7 cells following nanoparticle exposure (Figure 4.11). In addition to promoting a marked increase in the expression of TNF-α, the unmodified silk fibroin nanoparticles up-regulated the expression of several colony stimulating factors (M-CSF, G-CSF and GM-CSF), chemokines (CCL 1, CXCL 9, CXCL 13) and other essential pro-inflammatory cytokines (IFN-γ, IL-1α, IL-23 and IL-27). By contrast, PEGylated silk fibroin nanoparticle treatment caused a milder (or negligible) response in pro-inflammatory cytokine expression when compared to unmodified silk fibroin nanoparticles. The anti-inflammatory cytokine IL-10 remained unchanged regardless of the type of silk fibroin nanoparticle used, whereas IL-1RA expression increased in response to unmodified silk fibroin nanoparticles yet decreased following a dose with PEGylated silk fibroin nanoparticles.

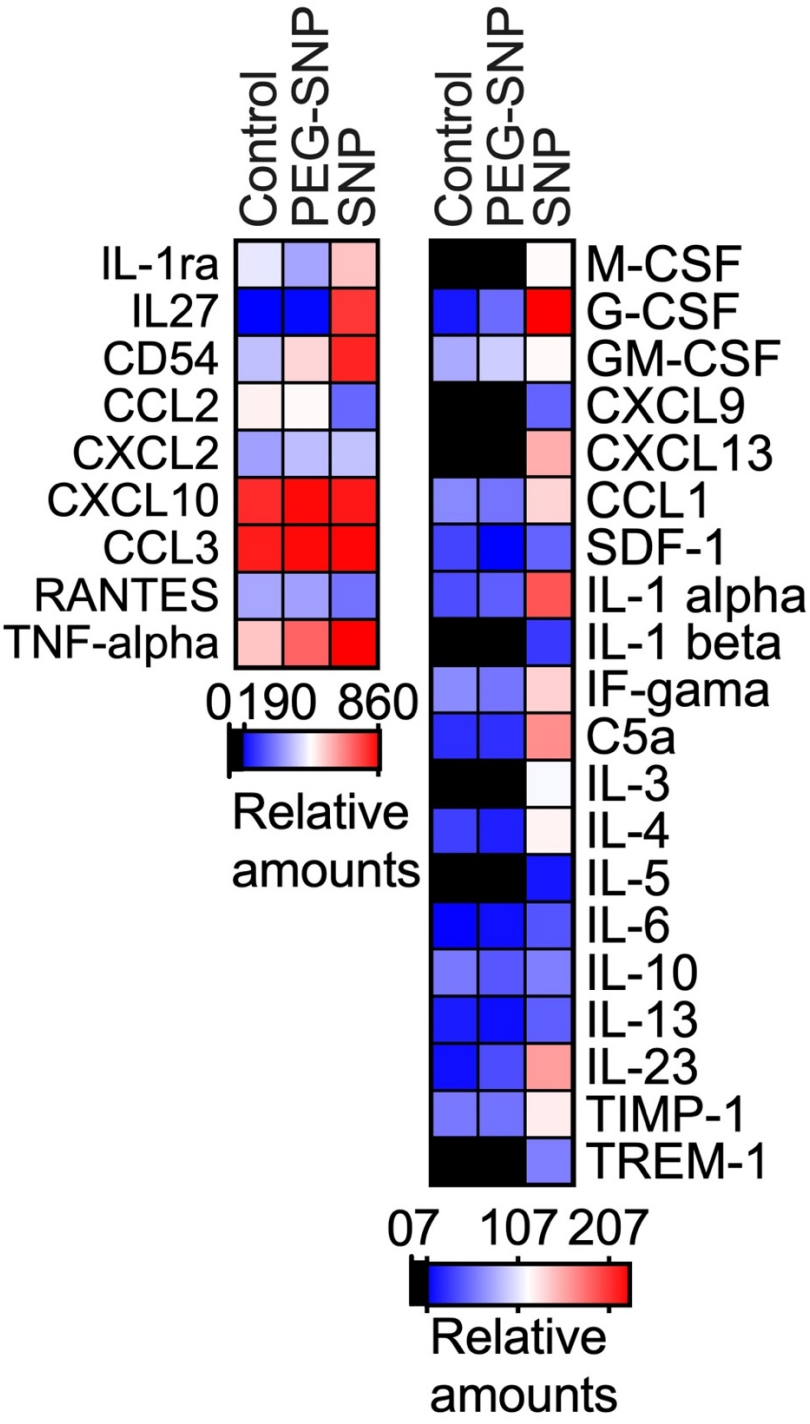

Figure 4.11. Extended cytokine profile. Cytokine profile of RAW264.7 cells following treatment for 24 h in the absence or presence of 0.1 mg/mL unmodified (SNP) or PEGylated (PEG-SNP) silk fibroin nanoparticles. Untreated cells served as the control. (n = 3)

4.3.5. Metabolomic response to unmodified and PEGylated silk fibroin nanoparticles

Next, the metabolic profiles of RAW 264.7 macrophages were analysed to further characterise the effects of silk fibroin nanoparticle PEGylation and concentration on inflammatory modulation. A scores scatter plot (Figure 4.12 A) produced by applying principal component analysis to the ^{1}H NMR spectra of aqueous cell extracts showed a separation between control and nanoparticle treated samples. Samples clustered differently depending on nanoparticle treatment, and in particular the high concentration of unmodified silk fibroin nanoparticles separated clearly from the remaining samples along principal component 1 (PC1, explaining 19.5% of total variance). These results were complemented by principle component analysis of lipophilic cell extracts (Figure 4.12 B), which showed some overlap between sample groups, especially in the case of PEGylated silk fibroin nanoparticles as they barely separated from controls. By contrast, different clusters were observed for lipophilic samples obtained from cells treated with unmodified silk fibroin nanoparticles, with those exposed to the high particle concentration grouping further away from the controls.

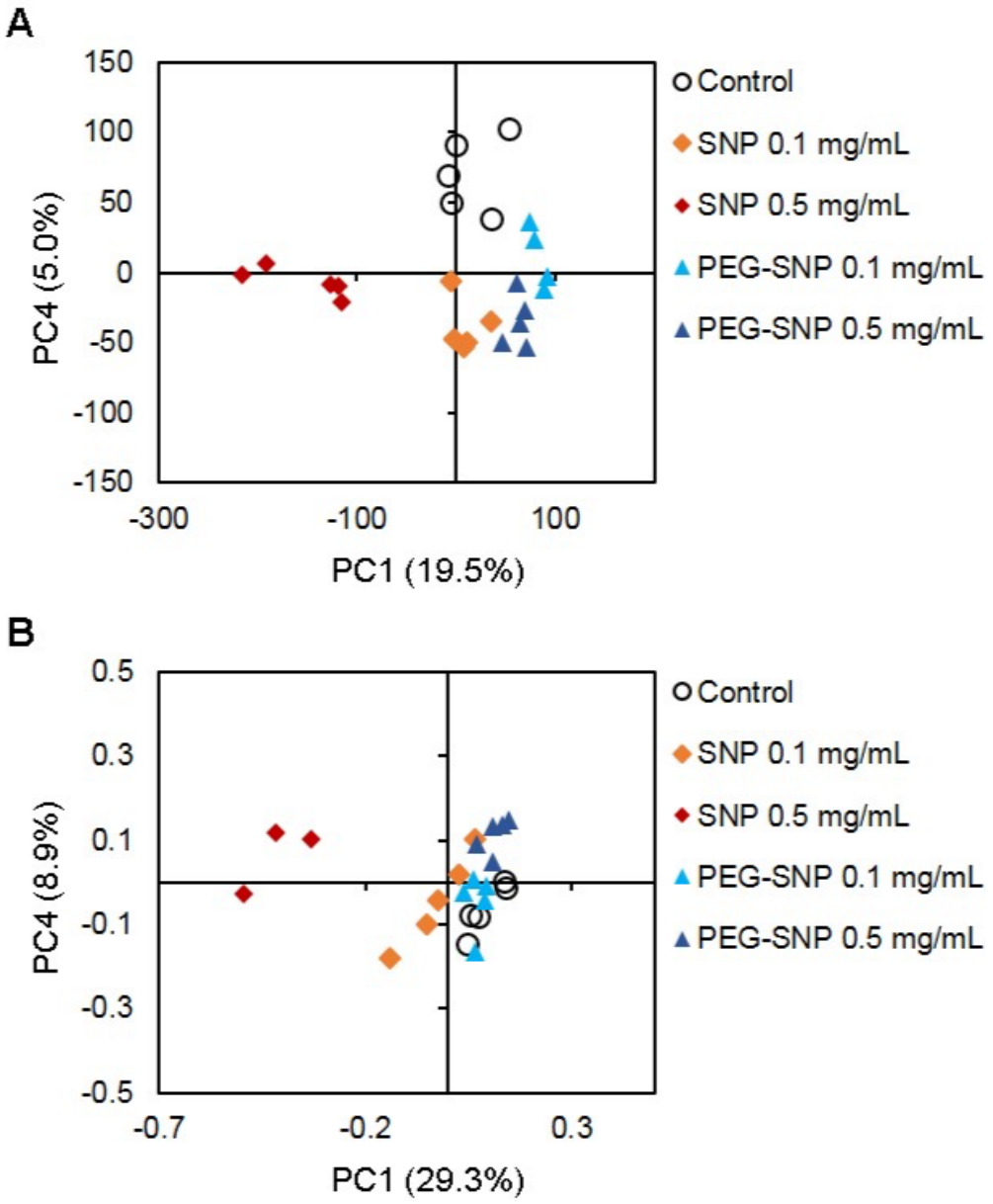

Figure 4.12. Scores scatter plots obtained by principal component analysis of ^{1}H NMR spectra from (A) aqueous extracts, (B) lipophilic extracts of RAW264.7 macrophages treated for 24 h with unmodified or PEGylated silk fibroin nanoparticles (SNPs) at concentrations of either 0.1 mg/mL or 0.5 mg/mL.

The principal component analysis scores map (Figure 4.13 A) obtained for samples from macrophages treated with unmodified silk fibroin nanoparticles confirmed the separation between control, low dose, and high dose samples. Partial least squares discriminant analysis (Figure 4.13 B) further revealed robust discrimination between control and nanoparticle-treated cells (Q2 0.79) due to differences in the levels of metabolites highlighted in the corresponding loading plots (Figure 4.13 C). In particular, unmodified silk fibroin nanoparticle-treated cells (negative scores in first latent variable, LV1) were characterised mainly by higher intracellular levels of lactate, creatine, phosphocreatine, and glycine (signals with negative LV1 loadings), together with lower levels of a few amino acids, choline compounds, betaine, and myo-inositol (positive loadings). In samples from macrophages treated with PEGylated silk fibroin nanoparticles (Figure 4.13 D), the low and high dose samples largely overlapped in the principal component analysis scores scatter plot, suggesting little dependence on nanoparticle concentration. When considering the two exposure concentrations within a single class, nanoparticle treated samples strongly differed from the controls by partial least squares discriminant analysis (Figure 4.13 E). The corresponding loading profiles (Figure 4.13 F) suggested decreased levels of branched chain amino acids and glucose, along with increased levels of glutamate, glutathione, and phosphocholine, in treated cells compared with controls.

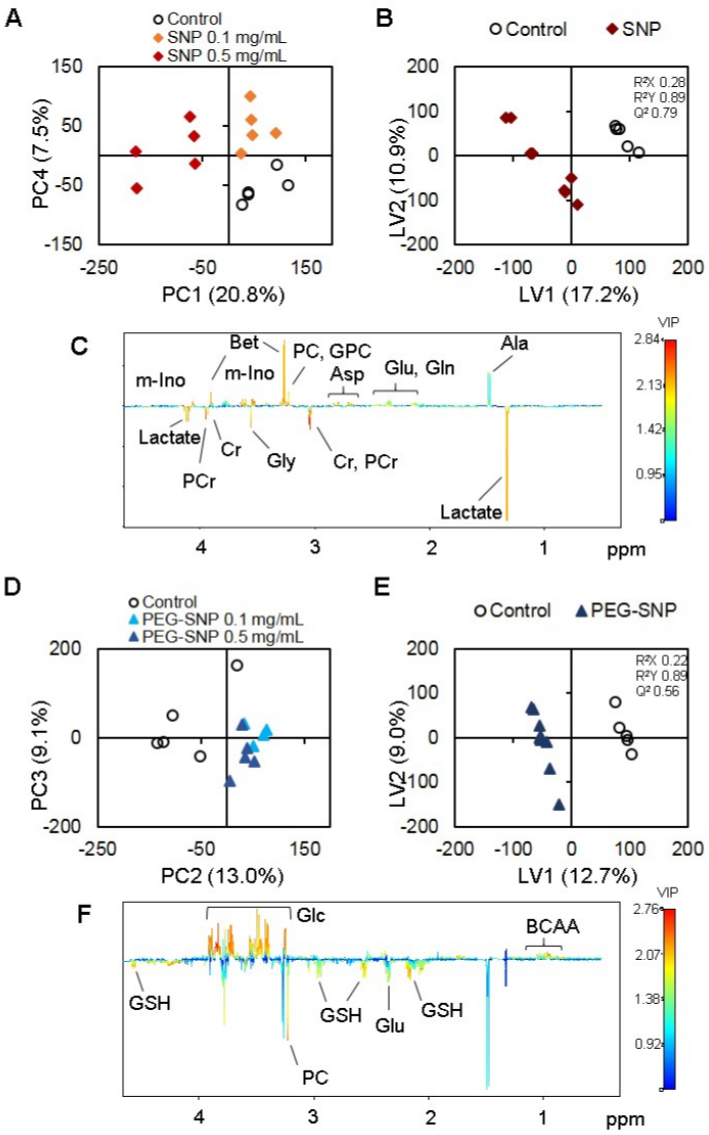

Figure 4.13. Multivariate analysis of ^{1}H NMR spectra from aqueous extracts of control macrophages and macrophages exposed for 24 hours to (A – C) unmodified (SNP), and (D-F) PEGylated (PEG-SNP) silk fibroin nanoparticles: (A, D) principal component analysis scores scatter plots; (B, E) partial least squares discriminant analysis scores scatter plots generated by pairwise comparisons (control and (PEG)-silk fibroin nanoparticle, 0.1 and 0.5 mg/mL as one class); (C, F) loadings *w* of latent variable 1 (LV1), coloured as a function of variable importance to the projection (VIP).

Spectral integration was then employed to confirm and extend the analysis of quantitative variations in individual metabolites (summarised in Figure 4.14). Overall, silk fibroin nanoparticles caused changes in 28 intracellular polar metabolites associated with different metabolic pathways. In regard to glycolysis and the tricarboxylic acid cycle (Figure 4.14 A), cells exposed to unmodified silk fibroin nanoparticles displayed a pronounced decrease in pyruvate levels and significant increases in lactate, itaconate, and succinate. By contrast, succinate and intracellular glucose levels decreased in cells treated with PEGylated silk fibroin nanoparticles. When comparing nanoparticle-induced changes to amino acid metabolism (Figure 4.14 A), unmodified silk fibroin nanoparticles decreased the intracellular levels of aspartate, glutamine, glutamate, and alanine, whereas levels of glycine, lysine, branched chain, and aromatic amino acids increased when compared to untreated controls. Interestingly, PEGylated silk fibroin nanoparticles either produced no change in some of these amino acids or caused variations in opposite direction to that observed for unmodified particles. Energy-related metabolites were also affected by silk fibroin nanoparticle treatment (Figure 4.14 A). When treated with unmodified silk fibroin nanoparticles, significant increases to creatine and phosphocreatine levels were observed at both concentrations, whilst only the high concentration impacted ATP levels (significant decrease). Again, milder effects were observed for macrophages treated with PEGylated silk fibroin nanoparticles. Marked changes were observed for metabolites that can act as antioxidants and/or osmoregulators or that relate to cell membrane composition (Figure 4.14 A). In general, these metabolites showed dose-dependent decreases in cells treated with unmodified silk fibroin nanoparticles, whereas they showed increased levels in cells treated with PEGylated silk fibroin

nanoparticles. Metabolites associated with lipid metabolism (Figure 4.14 A) were also differentially affected by the two nanoparticle types, with increases in 3-hydroxybutyrate, acetate, and formate being seen only in cells treated with unmodified silk fibroin nanoparticles.

Changes in metabolic pathways were also apparent through analysis of the exometabolome (Figure 4.14 B), with cells exposed to PEGylated silk fibroin nanoparticles consuming more glucose and excreting more lactate and itaconate when compared to untreated cells. These effects were more pronounced in cells treated with unmodified silk fibroin nanoparticles, and these cells also excreted more alanine and less citrate when compared to untreated controls. Finally, unmodified silk fibroin nanoparticles caused increases in (total/esterified) cholesterol and phosphatidylcholine, together with decreases in unsaturated fatty acids (Figure 4.14 C). By contrast, the effects of PEGylated silk fibroin nanoparticles were restricted to mild increases in total cholesterol and phosphatidylcholine.

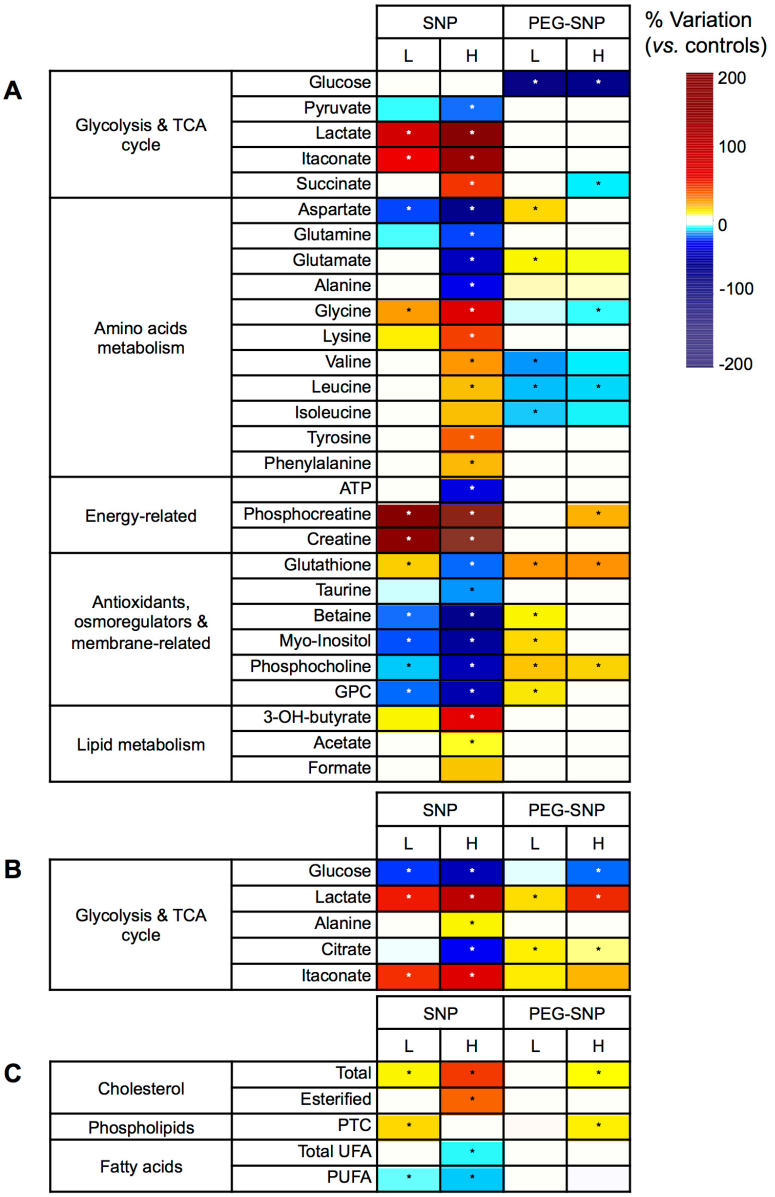

Figure 4.14. Heatmap of the main metabolite variations in (A) aqueous extracts, (B) culture media, and (C) lipophilic extracts, from macrophages exposed for 24 h to unmodified (SNP) or PEGylated (PEG-SNP) silk fibroin nanoparticles at concentrations of either 0.1 mg/mL or 0.5 mg/mL, coloured according to % variation in relation to controls. * p-value < 0.05. GPC: glycerophosphocholine, PTC: phosphatidylcholine, (P)UFA: (poly)unsaturated fatty acids.

4.4. Discussion

The biopolymer silk has a long clinical track record in humans[42] and silk fibroin nanoparticles have recently emerged as an interesting platform for drug delivery, including anticancer drugs.[68] However, the interactions of silk fibroin nanoparticles with macrophages have yet to be fully characterised, and this lack of knowledge limits the current understanding of what effects these nanoparticles will have on off-target tumour-associated macrophages. Tumour-associated macrophages show a tumorigenic profile[238] and a high distribution of these macrophages within a tumour is associated with poor patient prognosis.[141,239,240] However, these cells can be reprogrammed to assume a pro-inflammatory state that confers tumoricidal properties.[241] Therefore, since anticancer nanoparticles encounter macrophages upon accessing a tumour site, they provide a unique opportunity to modulate the inflammatory profiles of tumour-associated macrophages and thereby maximise the intratumoral performance.[154,242,243] The aims of this chapter were to examine the baseline performance of both unmodified silk fibroin nanoparticles in comparison to other materials, and to evaluate silk fibroin nanoparticle PEGylation and concentration on the inflammatory phenotype and metabolic profiles of macrophages. The purpose of this was to inform on interactions between silk fibroin nanoparticles and macrophages, and so the study was conducted without an anticancer drug payload to simplify data interpretation and to eliminate drug-mediated co-founding effects (e.g. drug-induced cytotoxicity).

When assessing the adjuvanticity of silk, silica and PLGA nanoparticles,[184] the phenotypic analyses conducted measured surface expression of CD80 and cytokine production in response to each nanoparticle type. (Figure 4.5). As one of the essential co-stimulatory molecules needed to initiate T cell activation,[244,245] CD80 is a classical marker of macrophage activation and is indicative of a change in macrophage inflammatory state. CD80 was significantly upregulated in response to all nanoparticle types (Figure 4.5 A, B), suggesting that nanoparticle-cell interactions can have an adjuvant effect on macrophages. Proteome profilers measured conditioned cell culture medium under the same conditions and revealed substantial upregulation of CCL 3 and CCL 4 (Figure 4.5 C), two pro-inflammatory chemokines[246] associated with an M1-like (LPS induced) state that are responsible for recruitment of macrophages and natural killer cells. In addition, silk fibroin nanoparticles upregulated CXCL2 and G-CSF, which are responsible for recruited neutrophils and monocytes, further indicating macrophage polarisation towards an M1-like state.[246] Importantly, none of the nanoparticle materials tested were able to increase levels GM-CSF, IL-6 or CCL 5, which are also classical indicators of an M1-like state. The additional increase to IL-1RA (an anti-inflammatory marker) in response to all nanoparticle treatments also highlighted the well-documented complexity of macrophage polarisation[247] and the need to extensively characterise macrophage markers before drawing conclusions on their biological roles.

Next, a more in depth study examining the impact of silk fibroin nanoparticle interactions with macrophages, and the effects of particle PEGylation were conducted. Similar to previously published reports[40] PEGylation of silk fibroin nanoparticles increased the hydrodynamic radius and moderated the surface charge when compared

to unmodified nanoparticles (Figure 4.4 A); an observation that aligns well with the literature.[248] The interaction of either unmodified or PEGylated silk fibroin nanoparticles with the macrophage plasma membrane caused no damage to the cell membrane (Figure 4.6 B). As observed previously,[40,249] unmodified silk fibroin nanoparticles had a higher propensity to aggregate in physiological media when compared to the PEGylated silk fibroin nanoparticles (Figure 4.8). However, this aggregation did not affect the macrophages' ability to phagocytose and traffic unmodified silk fibroin particles into lysosomes (Figure 4.9 A, B). The somewhat larger appearance of the lysosomes containing unmodified silk fibroin nanoparticles, when compared with those containing PEGylated silk fibroin nanoparticles, might be a consequence of the larger size of the internalised nanoparticle aggregates.

Both silk fibroin nanoparticle formulations were internalised and trafficked into lysosomes, but the downstream effects on the inflammatory profile of the macrophages were dependent on the surface modification and particle concentration. A high concentration of unmodified silk fibroin nanoparticles primed the RAW264.7 macrophages toward a pro-inflammatory phenotype, as evidenced by significant increases in levels of classical pro-inflammatory mediators (e.g., TNF-α, nitric oxide),[250–252] enhanced total antioxidant activity, and reduction in levels of reactive oxygen species (Figure 4.10 A – D). Reactive oxygen species levels are implicated in the differentiation of macrophages into wound-healing and tumour-associated phenotypes.[253] However, even at the low nanoparticle concentration, unmodified silk fibroin nanoparticles were able to induce a pro-inflammatory shift in macrophage phenotype, although to a lesser extent than the shift observed at the high concentrations (i.e., less production of nitric oxide and reactive oxygen species, but similar promotion

of TNF-α and antioxidant levels when compared to the high nanoparticle dose). The biological significance of macrophage priming at the low silk fibroin nanoparticle dose was also evident by the observed upregulation of the macrophage cytokine profile (e.g., colony stimulating factors, chemokines, and other essential proinflammatory substances) (Figure 4.11).

Particle PEGylation modulated the immunomodulatory effects of silk fibroin nanoparticles. At the high nanoparticle concentration, PEGylation moderated the production of pro-inflammatory mediators, including TNF-α, nitric oxide, total antioxidant activity, and reactive oxygen species when compared to the response to unmodified silk fibroin nanoparticles (Figure 4.10 A – D). At the low concentration, the PEGylated silk fibroin nanoparticles failed to evoke a robust inflammatory phenotype and only subtle differences were noted in cytokine production between the treated and control cells (Figure 4.10 A – D). Overall, these observations are important because they suggest the possibility of differential priming of macrophages, even at low nanoparticle concentrations.

While nanoparticles for drug delivery are typically designed to evade the immune system, a pro-immunogenic phenotype could be exploited to maximise intratumoral performance.[242,243] Others have shown a link between metabolic reprogramming and cell behaviour, such as macrophage activation status.[254] I therefore examined the baseline performance of both unmodified and PEGylated silk fibroin nanoparticles by monitoring nanoparticle-induced metabolic changes. Exposure to silk fibroin nanoparticles affected macrophage metabolism in a nanoparticle type- and concentration-dependent fashion (Figure 6). In agreement with our previous study,[184]

and similar to the metabolic phenotype described for lipopolysaccharide-activated pro-inflammatory macrophages,[255,256] cells treated with unmodified silk fibroin nanoparticles increased cellular glycolytic activity, as indicated by significantly increased glucose consumption, upregulated pyruvate to lactate conversion, and increased lactate and alanine excretion. Increased glycolysis was also apparent in cells treated with PEGylated silk fibroin nanoparticles, although the lactate levels in this case were only elevated in the medium supernatants, not intracellularly.

Cells treated with unmodified silk fibroin nanoparticles further displayed enhanced production of succinate and itaconate, which is consistent with the reprogramming of the tricarboxylic acid cycle associated with a pro-inflammatory state.[257] Succinate is known to inhibit cytosolic prolyl hydroxylases, thereby stabilizing HIF1α, whose target genes include glycolytic enzymes and inflammatory factors.[258] Additionally, succinate oxidation by succinate dehydrogenase drives the production of reactive oxygen species.[259] By contrast, itaconate, which is produced from citrate via cis-aconitate[260] inhibits succinate dehydrogenase[261] and acts as a counterbalance to limit inflammation.[262,263] This metabolite inhibits succinate dehydrogenase and activates the anti-inflammatory and anti-oxidant transcription factor Nrf2, thus restricting downstream inflammatory gene expression and limiting the production of pro-inflammatory mediators like IL-1β and IL-6.[263] Activation of the Nrf2/anti-oxidant response element pathway could result in increased expression of antioxidant enzymes (e.g., catalase, superoxide dismutase), as well as increased glutathione synthesis.[264] Therefore the observed itaconate increase and enhanced antioxidant capacity could ultimately equip cells better to neutralise reactive oxygen species. This proposal is consistent with the observed decrease in reactive oxygen species upon nanoparticle

treatment. Therefore, this chapter corroborates previous observations[184] of a close link between rewiring of tricarboxylic acid cycle, the cells redox status, and the production of pro-inflammatory cytokines.[264] Another consequence of this type of metabolic reprogramming could be the observed ATP depletion in cells exposed to a high concentration of unmodified silk fibroin nanoparticles, which, as noted previously,[184] could be due to both inhibition of succinate dehydrogenase (and hence oxidative phosphorylation)[265] and downregulation of substrate-level phosphorylation.[266]

The marked decrease in intracellular levels of some amino acids in cells treated with unmodified silk fibroin nanoparticles further support tricarboxylic acid cycle reprogramming. In particular, glutamine/glutamate and aspartate could be used to replenish α-ketoglutarate and oxaloacetate, respectively, and so could be involved in the aspartate-arginosuccinate shunt, which is important in lipopolysaccharide-induced macrophage activation.[256] By contrast, a different set of amino acids (glycine, lysine, branched chain, and aromatic amino acids) increased in cells treated with unmodified silk fibroin nanoparticles, possibly reflecting protein catabolism.[184] The PEGylated silk fibroin nanoparticles did not have a similar effect on the tricarboxylic acid cycle. No intracellular increases were noted in succinate or itaconate upon nanoparticle treatment; although succinate levels were decreased at the higher nanoparticle dose. Clear reduction in tricarboxylic acid cycle rewiring and itaconate production coincided with a reduced inflammatory phenotype in RAW264.7 macrophages, and this supports observations made with unmodified silk fibroin nanoparticles.

Another prominent effect of unmodified silk fibroin nanoparticles was the significant intracellular upregulation of creatine and phosphocreatine. Although the functional

relevance of these metabolites in macrophage responses to nanoparticles remains to be determined, one possibility is that the creatine kinase/phosphocreatine system plays an important role, possibly in relation to energy buffering and phagocytic function.[267] Interestingly, PEGylated silk fibroin nanoparticles produced a milder increase in phosphocreatine and no change in creatine levels, suggesting a less extensive impact on the creatine kinase system. One other explanation for the increased lysosome size observed in response to unmodified silk fibroin nanoparticles might be a differential demand on the creatine kinase system of the phagocytosing macrophages (Figure 4.9). The lower aggregation of PEGylated silk fibroin nanoparticles could possibly place less demand on the creatine kinase system. This observation warrants further investigation.

The levels of several metabolites involved in osmoregulation, anti-oxidant protection, and/or cell membrane composition also showed distinct variation patterns in cells exposed to unmodified or PEGylated silk fibroin nanoparticles. In response to unmodified silk fibroin nanoparticles the levels of antioxidant metabolites glutathione (albeit increased at the lower dose treatment), taurine, and betaine decreased, which may possibly reflect their use to counterbalance reactive oxygen species generation by pro-inflammatory macrophages.[268,269] The observed decrease in reactive oxygen species levels in nanoparticle-treated cells is in line with these observations. By contrast, the levels of glutathione, and betaine to a lesser extent, increased in cells treated with PEGylated silk fibroin nanoparticles. Opposite variations were also found for myo-inositol, phosphocholine, and glycerophosphocholine, which are metabolites with known involvement in membrane remodelling and osmotic balance.

Lastly, unmodified silk fibroin nanoparticles, but not PEGylated ones, caused increases in metabolites that could arise from enhanced lipid metabolism: 3-hydroxybutyrate, acetate, and formate. Changes in cellular lipid composition were also apparent from the analysis of lipophilic extracts (Figure 6C). Treatment with unmodified silk fibroin nanoparticles and, to a lesser extent, PEGylated silk fibroin nanoparticles caused cells to increase their cholesterol and phospholipid content. Additionally, the levels of unsaturated fatty acids decreased upon exposure to unmodified nanoparticles, again possibly reflecting remodelling of membrane composition and fluidity.

4.5. Conclusions

This chapter demonstrated that unmodified silk fibroin nanoparticles induced macrophage polarisation towards an M1-like state. Similar effects were observed when macrophages were treated with silica or PLGA nanoparticles of a similar size, indicating that silk fibroin nanoparticles have similar macrophage adjuvanticity to other leading nano-materials. Specifically, unmodified silk fibroin nanoparticles were shown to modulate macrophage activation and metabolism towards a pro-inflammatory phenotype in concentration-dependent and PEGylation-dependent manners. This was observed using traditional immunoassays for cytokine release, antioxidant levels, nitric oxide and ROS production, as well as by ^{1}H NMR metabolomic analyses that revealed extensive reprogramming of several metabolic processes. The ability to modulate macrophage phenotype with silk fibroin nanoparticles could be especially useful in the context of anticancer drug delivery, as they could act both as carriers for chemotherapeutics and as synergistic attenuators of tumour-associated macrophages towards a more tumoricidal phenotype.

Chapter 5: Assessment of cellular factors affecting endocytosis of nanoparticles.

Chapter summary:

This chapter set out to characterise cellular factors that govern endocytosis and intracellular trafficking of unmodified and PEGylated silk fibroin nanoparticles. Intracellular trafficking profiles for both particles were produced at early, intermediate and late timepoints. Attempts were made to inhibit specific endocytic pathways to verify the overall effects on intracellular trafficking. The stage of cell cycle progression and extracellular microenvironmental cues were also considered as factors influencing endocytosis of nanoparticles.

5.1. Introduction

Research in nanotechnology for healthcare applications was consolidated under the umbrella term "nanomedicine" in 2005, and the use of nanomedicines to improve drug delivery is one of the principle aims of the field.[2] As nanomedicines are engineered to treat specific diseases, they are aptly suited drug carriers as they can tune drug bioavailability, control drug release and deliver therapeutic payloads to tissues, cells or sub-cellular compartments.[1] This is evidenced in their use against solid tumours, where nanomedicines use the EPR effect to increase the effective dose that reaches the tumour site.[16] Nanomedicines then exploit the endocytic machinery of tumour cells to enter them and deliver drugs lysosomotropically, thereby changing the mechanism of delivery to overcome drug resistance mechanisms and controlling the rate of intracellular drug release as the carrier is degraded.[104]

Cells use different endocytosic pathways to internalise material from their extracellular environment and often shuttle the material into lysosomes. Importantly, endocytosis is cell type-dependent, with specialised immune cells (e.g. macrophages, dendritic cells, neutrophils) typically using the process of phagocytosis and "non-professional" cells using pinocytosis or receptor-mediated mechanisms such as clathrin-, caveolae-, Rho-, ARF6-, or CDC42-mediated endocytosis.[77] There are typically fewer restrictions on nanomedicine design when targeting phagocytic cells as phagocytosis is used to internalise a range of extracellular material, including: extracellular waste, apoptotic cells and extracellular pathogens.[82] Non-phagocytic routes of endocytosis are used by virtually all other cells to take up nutrients and maintain homeostatic balance, and this places restrictions on the nanomedicines that

can be used to target these cells. For example, clathrin-mediated endocytosis is the most widely understood endocytic pathway and the formation of clathrin-coated vesicles restricts the size of material internalised to approximately < 300 nm.[74] Size restrictions must also be considered when targeting caveolae-mediated and CDC42-mediated endocytosis mechanisms, as the upper size limits for internalisation into these pathways have been defined as < 80 nm and < 50 nm, respectively.[74] Additional factors such as the shape,[120] surface chemistry[270] and mechanical properties[271] of nanomedicines can also impact the route of entry into target cells and these factors must be considered when engineering nanomedicines for third order drug targeting.

Accessing the intracellular machinery of cells by endocytosis is essential for nanomedicines. However, downstream endocytic trafficking pathways are highly organised and can route into different locations such as the degradation pathway, the trans-Golgi network or the recycling pathway.[87] Correct intracellular routing is crucial for organelle-specific drug targeting and controlled drug release, and anticancer nanomedicines are often designed to traffic into the degradation pathway and deliver payloads lysosomotropically.[76,105] Incorrect routing to the trans-Golgi network or recycling pathway could result in intracellular re-routing or exocytosis from the cell, ultimately rendering the nanomedicine ineffective. Therefore, the different endocytic trafficking pathways must be considered to ensure maximum intracellular targeting and efficient drug release.

Routes of endocytosis and intracellular trafficking can become altered in different disease states, including cancer.[272] Integrins and cadherins are required to maintain healthy adherens junctions, tight junctions and focal adhesions, and recycling of these

cell adhesion molecules is tightly regulated by endocytosis.[273,274] In cancer, cell adhesion molecule recycling is dysregulated and the resulting breakdown in cell-cell and cell-ECM interactions contributes to metastasis in breast cancer.[275,276] Dysfunctional endocytosis has been observed in dynamin-dependent (i.e. clathrin-mediated endocytosis, caveolae-mediated endocytosis) endocytic pathways in cancer,[277,278] and predicting the intracellular performance of anticancer nanomedicines is therefore extremely difficult. In addition, there is growing interest in the influence of tumour cell and microenvironmental factors influencing the endocytosis of nanomedicines, with studies demonstrating the role of position in the cell cycle,[279] hypoxic conditions,[280] and extracellular matrix (ECM) stiffness[177,179,281] on endocytosis of nanoparticles.

The results of chapter 3 demonstrated that silk fibroin nanoparticles delivered therapeutic payloads in a lysosomotropic manner. However, the study was only conducted at one time-point and there is still very little known about the specific mechanisms governing endocytosis and trafficking of silk fibroin nanoparticles in metastatic breast epithelial cells. Therefore, this chapter aimed to elucidate the dependence of silk fibroin nanoparticles on clathrin-mediated endocytosis for correct intracellular entry and trafficking, whilst considering the influence of cancer-associated factors such as tumour cell heterogeneity and cell-ECM interactions that are known to affect endocytosis. The aims were: (i) investigate the uptake of silk fibroin nanoparticles in breast epithelial cells whilst inhibiting specific endocytic pathways, (ii) assessment of time dependent intracellular silk fibroin trafficking in the absence and presence of endocytic inhibition, (iii) explore the influence of cell cycle

progression on endocytosis of silk fibroin nanoparticles, and (iv) investigate the effects of ECM stiffness on endocytosis of nanoparticles.

5.2. Experimental procedures

5.2.1.Preparation, characterisation and fluorescent labelling of unmodified and PEGylated silk fibroin nanoparticles

A detailed methodology outlining the production and characterisation of unmodified and PEGylated silk fibroin nanoparticles was provided in chapter 2 (sections 2.1 – 2.3). The standard method for fluorescent labelling of unmodified and PEGylated silk fibroin nanoparticles has been covered elsewhere. In this chapter, AF488-silk fibroin nanoparticles and FITC-PEG-SNPs were produced according to the methods outlined in sections 2.5 and 4.2.

5.2.2. Latex nanoparticles

Fluospheres® (Thermo Fisher Scientific, Waltham, MA, USA) were purchased to be used as a model nanomedicine. These are 100 nm carboxylate-modified latex nanoparticles that have an excitation/emission profile (505/515 nm) similar to that of FITC.

5.2.3. Fluorescent transferrin

Alexa Fluor 488® labelled transferrin (AF488-Tf) was purchased (Thermo Fisher Scientific, Waltham, MA, USA) for verification of clathrin-mediated endocytosis recycling in the absence and presence of endocytosis inhibitors.

5.2.4. Production of stiffness-tuneable poly(acrylamide) hydrogel

A sandwich model protocol[189] was used to manufacture PA hydrogels with tuneable elasticity to mimic the stiffness of the breast tumour microenvironment. The required materials, and necessary protocols to produce these gels were presented in section 2.11.

In this chapter, PA hydrogels were produced using the method outlined by Tse *et al.*[189] as detailed mixing ratios are provided to produce hydrogels with specific elastic moduli ranging from 0.5 – 20 kPa. All elastic moduli quoted for PA hydrogels in this study are estimated from the data in this study.[189] PA hydrogels were functionalised with type I collagen to enable cell adhesion, as outlined in section 2.11.

5.2.5. Verification of PA hydrogel collagen I functionalisation

Collagen binding to PA hydrogels was verified using a double immunofluorescent staining protocol. Collagen-functionalised PA hydrogels in 35 mm petri dishes were stained overnight at 4 °C with mouse anti-collagen 1 monoclonal antibody (0.1 μg/mL) (Abcam, Cambridge, UK; ab6308, LOT: GR323228-1) to bind collagen on the gel surface. Next, PA gels were subjected to three 20-minute washes in 1 × PBS -tween (0.1%) (1 × PBS-T) and this was followed by a one-hour incubation at room temperature with AF488-conjugated goat anti-mouse polyclonal secondary antibody (0.1 μg/mL). The PA hydrogels were again washed three times for 20 minutes in 1 × PBS-T and then submerged in 1 × PBS to ensure the gel remained hydrated. Immunostained hydrogels were then imaged by confocal microscopy.

5.2.6. Cell culture

MCF-7 cells were used in this chapter to measure cellular factors influencing the endocytosis and intracellular trafficking of silk fibroin nanoparticles in metastatic breast epithelial cells. MCF-10A and MDA-MB-231 cells were also used when studying the effects of substrate stiffness on endocytosis as they represented healthy and triple-negative breast epithelial cells. Acquisition, culture and maintenance of all lines has been described in chapter 2 (sections 2.6). Unless otherwise stated, all cells were seeded at a density of 2×10^4 cells/cm^2.

5.2.7. MTT cytotoxicity assay

A detailed methodology outlining the principles of the MTT assay and standard protocol used to determine cell viability was provided in chapter 2 (section 2.7).

In this chapter, MCF-7 cells were seeded at 2×10^4 cells/cm^2 in complete DMEM and allowed to recover overnight. Next, cells were either left untreated (negative control) or were dosed for 24 hours in complete DMEM supplemented with either: (i) unmodified or PEGylated silk fibroin nanoparticles (0 – 500 μg/mL), or (ii) latex nanoparticles (0 – 5 mg/mL). The MTT assay was carried out as outlined in section 2.7 to determine the percentage of cell viability following each treatment.

5.2.8.Resazurin assay

A resazurin (7-Hydroxy-3H-phenoxazin-3-one 10-oxide) assay was used to assess cell viability of breast epithelial cells cultured on glass, tissue culture polystyrene or PA hydrogels following a 24 or 72 hour incubation. This assay works in a similar manner to the MTT assay, in this case with resazurin being metabolised by cells into the oxidised form that is detectable in a fluorescent microplate reader (excitation/emission: 530 – 560 ⁄ 590). Resazurin (Sigma-Aldrich, St. Louis, MO, U.S.A.) was purchased and reconstituted in 1 × PBS to a concentration of 440 μM determined from the wider literature.[282]

In this chapter, MCF-10A, MCF-7 and MDA-MB-231 cells were seeded at 2×10^4 cells/cm^2 in complete DMEM onto glass, tissue culture polystyrene or PA hydrogels of increasing stiffness (0.5 kPa – 20 kPa, estimated) and allowed to recover overnight. Next, 50 µL resazurin (440 µM) was added to each well and plates were returned to the incubator for 4 hours. 100 µL of media was transferred to wells in a black 96 well plate (Greiner Bio-One International, Austria). Cells were washed three times with 1 × PBS and then media was replaced, with cells then being returned to the incubator for another 48 hours. The process was repeated at this point to provide data on cell viability at 72 hours post seeding. Black 96 well plates were read on the POLARStar Omega plate reader.

5.2.9. Dynasore

The cell permeable dynamin inhibitor dynasore (Sigma-Aldrich, St. Louis, MO, U.S.A) was selected as an uptake inhibitor for studies investigating the internalisation of latex nanoparticles as it is a well-documented inhibitor of clathrin- and caveolae-mediated endocytosis.[283] Verification of effective dynasore inhibition is assessed by measuring the internalisation of fluorescently labelled transferrin, a serum glycoprotein that is essential for iron transport and can only enter cells using clathrin-mediated endocytosis.[284] At an 80 µM concentration Dynasore blocks the uptake of Alexa Fluor® 568 labelled transferrin in the HeLa cervical cancer cell line, human U373-MG astrocytes and monkey BSC1 and COS1 cells.[285] This concentration was therefore selected for inhibition of AlexaFluor® 488 labelled Tf in MCF-7 cells.

Dynasore was purchased and reconstituted to a stock solution of 40 mM in DMSO. The stock solution was aliquoted into 20 µl volumes and stored at -20°C. Prior to use, aliquots were removed from the -20 °C freezer and allowed to equilibrate at room temperature for at least one hour. Once aliquots were thawed they were diluted in a 15 mL conical tube using unsupplemented DMEM, high glucose, HEPES, no phenol red (Thermo Fisher Scientific, MA, USA) to a final concentration of 80 µM for in transferrin inhibition studies.

5.2.10. Transferrin inhibition studies

Cells were removed from the incubator, aspirated and washed twice with 1 × PBS to remove endogenous transferrin from the culture medium. Cells were then serum starved with unsupplemented phenol red-free DMEM containing HEPES for 30 minutes at 37 °C to allow transferrin-bound transferrin receptors to recycle back to the plasma membrane and release endogenous transferrin back into the culture medium. Cells were washed again, culture medium was replaced with phenol red-free DMEM containing HEPES that was unsupplemented or supplemented with dynasore (80 µM) and plates were returned to the 37 °C 5% CO_2 environment for 30 minutes to allow dynasore to block dynamin-dependent processes in treated wells. Next, cells were either (i) dosed immediately with AF488-labelled transferrin (10 µg/mL) for 30 minutes at 37°C, or (ii) placed on ice for 30 minutes prior to being dosed with AF488-Tf for 30 minutes at 4°C. The incubation was halted by placing cells on ice, aspirating all media and washing 3 times with ice cold 1 × PBS to remove any free transferrin

from the wells. Cells were then washed for 1 minute with ice cold glycine acid wash buffer containing 150 mM NaCl (0.2 M, pH 3.068) to remove all surface bound transferrin. The acid wash method was previously verified by treating MCF-7 cells (2 × 10^4 cells/cm^2) with AF488-Tf (10 μg/mL) at 4°C for 30 minutes and then acid washing to determine the effectiveness (Figure 5.1). All cells were detached by trypsinisation and collected for data acquisition by flow cytometry.

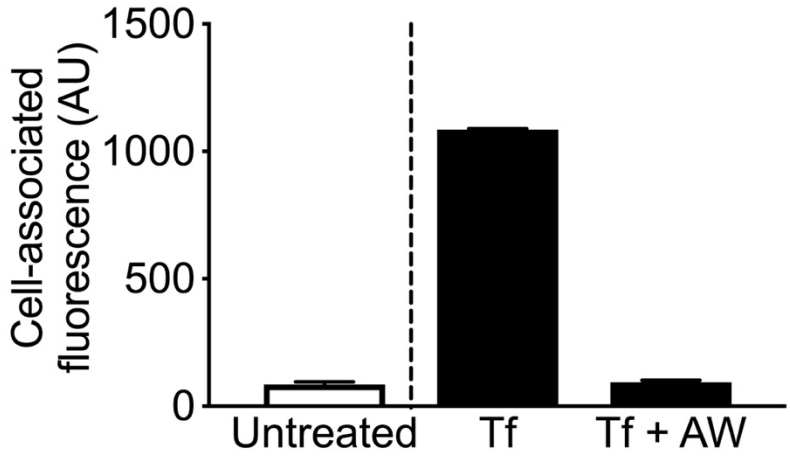

Figure 5.1. Acid wash quenching of extracellular AF488-Tf signal. MCF-7 cells seeded at 2 × 10^4 cells/cm^2 and dosed with transferrin (Tf) at 4 °C for 30 minutes. Extracellular fluorescent signal was quenched by conducting a one minute ice cold Glycine acid wash step before detachment. (n = 2).

5.2.11. siRNA interference

A smartpool siRNA transfection protocol was used to knock down AP-2 expression in MCF-7 cells as a method to inhibit clathrin-mediated endocytosis. An AP-2 DharmaFECT transfection mixture was produced by reacting 20 μM DharmaFECT 2 Transfection Reagent (GE Healthcare Dharmacon, Inc., Lafayette, Colorado, U.S.A) with 25 nM AP-2 siRNA and incubating for 20 minutes at room temperature. A control green fluorescent protein (GFP) DharmaFECT transfection mixture was also produced using the same 20 μM:25 nM mixing ratios using GFP siRNA.

MCF-7 cells were seeded (2×10^4 cells/cm^2) and left to recover for 24 – 48 hours. Cells were then transfected with either the AP-2 or GFP DharmaFECT mixture for 24 – 48 hours to allow for knock down of gene expression. To verify the effects on clathrin-mediated endocytosis, cells were pre-incubated in serum free medium for 30 minutes at 37°C (one medium change after 15 minutes) and then dosed with 10 nM AF488-Tf in serum free medium for 30 minutes. The cells were then placed on ice, washed three times with ice cold 1 × PBS and imaged by live confocal microscopy.

5.2.12. Time- and cell cycle-dependent uptake of silk fibroin nanoparticles

MCF-7 cells were seeded (2×10^4 cells/cm^2) and allowed to recover for 48 hours. Then, they were washed 3 times with 1 mL 1 × PBS and incubated for 2 hours in the absence or presence of either unmodified (100 μg/mL) or PEGylated (50 μg/mL) silk fibroin nanoparticles diluted in serum free medium. Next, cells were washed again (3 times with 1 × PBS), medium was replaced with complete DMEM, and cells were incubated for a further 3 or 22 hours, thereby providing 2h, 5h and 24h time-points from which to assess time dependent intracellular trafficking or cell cycle dependent endocytosis.

For time-dependent intracellular trafficking of silk fibroin nanoparticles the cells then underwent final washes (3 times with 1 × PBS) and were either imaged by live confocal microscopy or analysed by flow cytometry, with 20,000 live cells being recorded.

For cell cycle-dependent endocytosis of silk fibroin nanoparticles, cells were trypsinised and collected into 5 mL falcon tubes. Cells were washed three times (1 × PBS) by centrifugation and after the 3rd PBS wash and the supernatant was decanted and replaced with ice cold ethanol (70%) as a fixative. Cells were fixed at -20°C for a minimum of 24 h. Following fixation, the ethanol was removed by centrifugation and replacing the supernatant with 1 × PBS. Three PBS washes were conducted in total. Cells were then treated with RNAse A (Thermo Fisher Scientific, Waltham, MA, USA) at 37°C for 30 minutes with gentle agitation and then cells were washed a final

3 times and resuspended in 1 × PBS. 7-AAD was added to a final concentration of 5 μg/ml and cells were incubated at room temperature for 10 minutes prior to analysis by flow cytometry, with 50,000 ungated events being recorded. G1, S and G2 phases of proliferation were then identified and gated in the APC channel (Figure 5.9A).

5.2.13. Substrate stiffness-dependent endocytosis of nanoparticles

MDA-MB-231, MCF-7 or MCF-10A cells were seeded onto PA hydrogels at 2×10^4 cells/cm^2 in complete DMEM onto glass, tissue culture polystyrene or PA hydrogels of increasing stiffness (0.5 kPa – 20 kPa, estimated) and allowed to recover for 24 or 72 hours. Following recovery, media was aspirated and cells were washed three times in 1 × PBS. Coverslips containing the gels and adherent cells were then transferred to fresh wells to ensure that no cells within the wells were attached to a polystyrene surface. Cells were then dosed for either: (i) 1 hour with latex nanoparticles (20 μg/mL) in fully supplemented DMEM, or (ii) 2 hours with unmodified (50 μg/mL) or PEGylated (100 μg/mL) silk fibroin nanoparticles. Following this, cells were washed and prepared for data acquisition by flow cytometry as outlined in chapter 2 (section 2.10). 20,000 events were recorded within a live-singlet gate and geometric mean fluorescence intensity within the FITC channel (530/30) was measured to determine cell-associated fluorescence following exposure to fluorescently labelled latex or silk fibroin nanoparticles.

5.2.14. Flow cytometry

Flow cytometry equipment, data acquisition and data analysis software has been described in chapter 2 (section 2.10). The gating strategy used for data acquisition differed depending on the measurement being conducted, and these were outlined in the appropriate sections.

5.2.15. Confocal microscopy

Confocal microscopy equipment, data acquisition and data analysis software has been described in section 2.9.

5.2.16. Statistical analyses

All flow cytometry data was processed using FlowJo V10.2 (Ashland, OR, USA). All data were analysed using GraphPad Prism 7.0b (GraphPad Software, La Jolla, CA, U.S.A.). Multiple samples were evaluated by one-way analysis of variance (ANOVA) followed by Bonferroni's multiple comparison post hoc test. An asterisk denotes statistical significance as follows: *P < 0.05, **P < 0.01, ***P < 0.001. All data are presented are as mean values ± standard deviation (SD) and in reverse to the number of independent experiments.

5.3. Results

5.3.1. Cytotoxicity of unmodified and PEGylated silk fibroin nanoparticles

Cell viability of MCF-7 cells was unaffected by treatment of unmodified or PEGylated silk fibroin nanoparticles up to a concentration of 100 μg/mL. Both formulations were found to significantly impact MTT metabolism at concentrations of 250 μg/mL or higher, however this was not sufficient to reduce viability to IC_{50}.

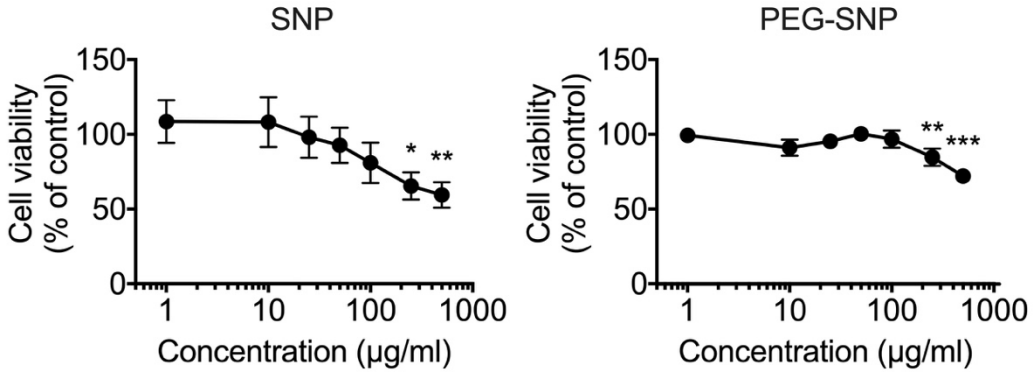

Figure 5.2. Cytotoxicity analysis of unmodified and PEGylated silk fibroin nanoparticles. MCF-7 cells dosed with 0 – 500 μg/mL unmodified or PEGylated silk fibroin nanoparticles for 24 hours. Cell viability was then measured by MTT assay. (n = 3).

5.3.2. MCF-7 cells are highly resistant to endocytic inhibition

Dynasore was selected to inhibit clathrin-mediated endocytosis due to its widely documented and reproducible use when testing nanomedicines.[283,286] The effectiveness of these inhibitors was determined by using flow cytometry and confocal microscopy to measure the effects on transferrin recycling, a process that is exclusively controlled by clathrin-mediated endocytosis. 80 μM dynasore and was selected from the literature as an effective working concentration for inhibition of clathrin-mediated endocytosis.[285] MCF-7 cells were then pre-treated for 30 minutes with dynasore (80 μM) prior to treatment with AF488-Tf for 0 – 30 minutes in the presence of dynasore (80 μM). This experimental model has been previously published using A431 (epidermal carcinoma) cells,[286] with approximately 50% – 80% inhibition of clathrin-mediated endocytosis depending on the duration of incubation with transferrin. In MCF-7 cells, the maximum inhibition observed was 40.4% and this was at the 5 minute time-point. At longer time-points the inhibitory effects were less pronounced, with 19.0% and 11.4% reductions in endocytosis being observed at the 15- and 30-minute time-points (Figure 5.3).

Attempts were also made to improve the efficiency of dynasore by determining the concentration and duration of dose empirically for MCF-7 cells. As well as the 80 μM concentration, 160 μM was also selected and MCF-7 cells were pre-treated for 30, 60 or 120 minutes prior to being dosed with AF488-Tf for 30 minutes (Figure 5.4 A, B). The inhibition efficiency was found to increase in a concentration and time-dependent manner, with the most effective treatment observed being the 160 μM dynasore dose for 120 minutes (Figure 5.4 A). However, these conditions introduced problems during

the acquisition of data on the flow cytometer by substantially reducing the number of events recorded within a live singlet gate (Figure 5.4 B). Confocal microscopy was used to image MCF-7 cells after 60 minutes in the presence of 80 μM dynasore (30-minute pre-treatment followed by 30-minute AF488-Tf dose) and showed marked changes to cell morphology (Figure 5.4 C).

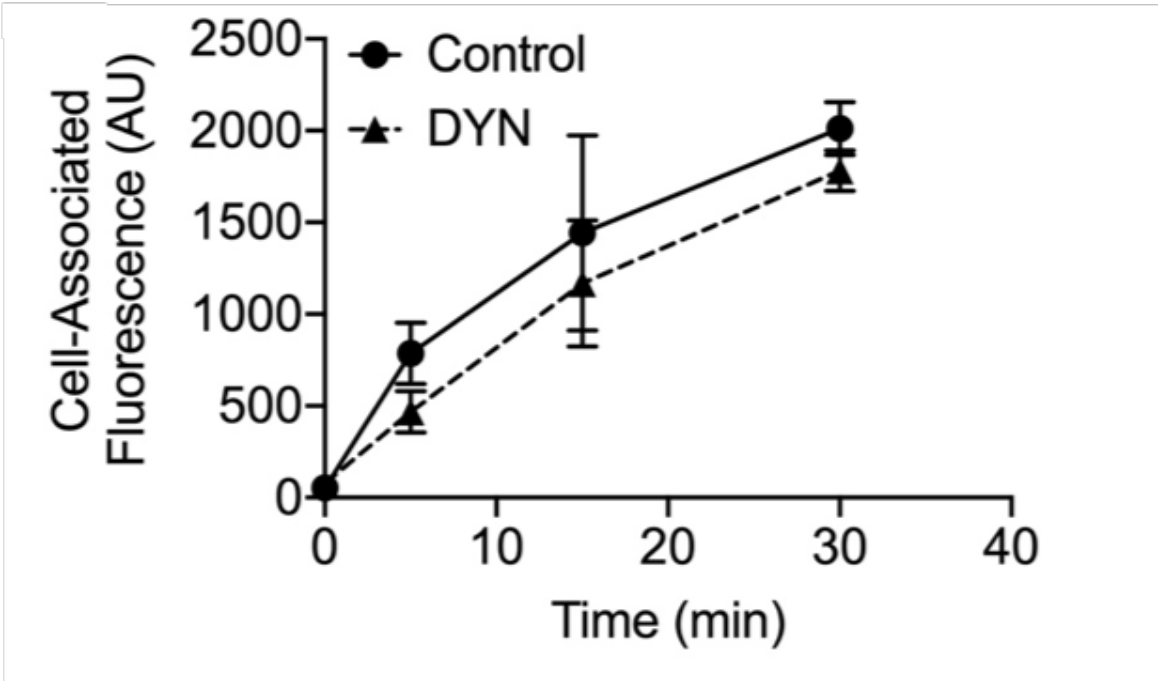

Figure 5.3. The inhibitory potential of DYN in MCF-7 cells. MCF-7 cells seeded at 4 × 10^4 cells/cm^2 and dosed with 80 μM DYN for 30 minutes followed by incubation with 5 μg/mL transferrin (Tf) at 37 °C for 0 – 30 minutes. Extracellular fluorescent signal was quenched using a 1 minute acid wash step prior to cell detachment. Data from three independent experiments (n =3).

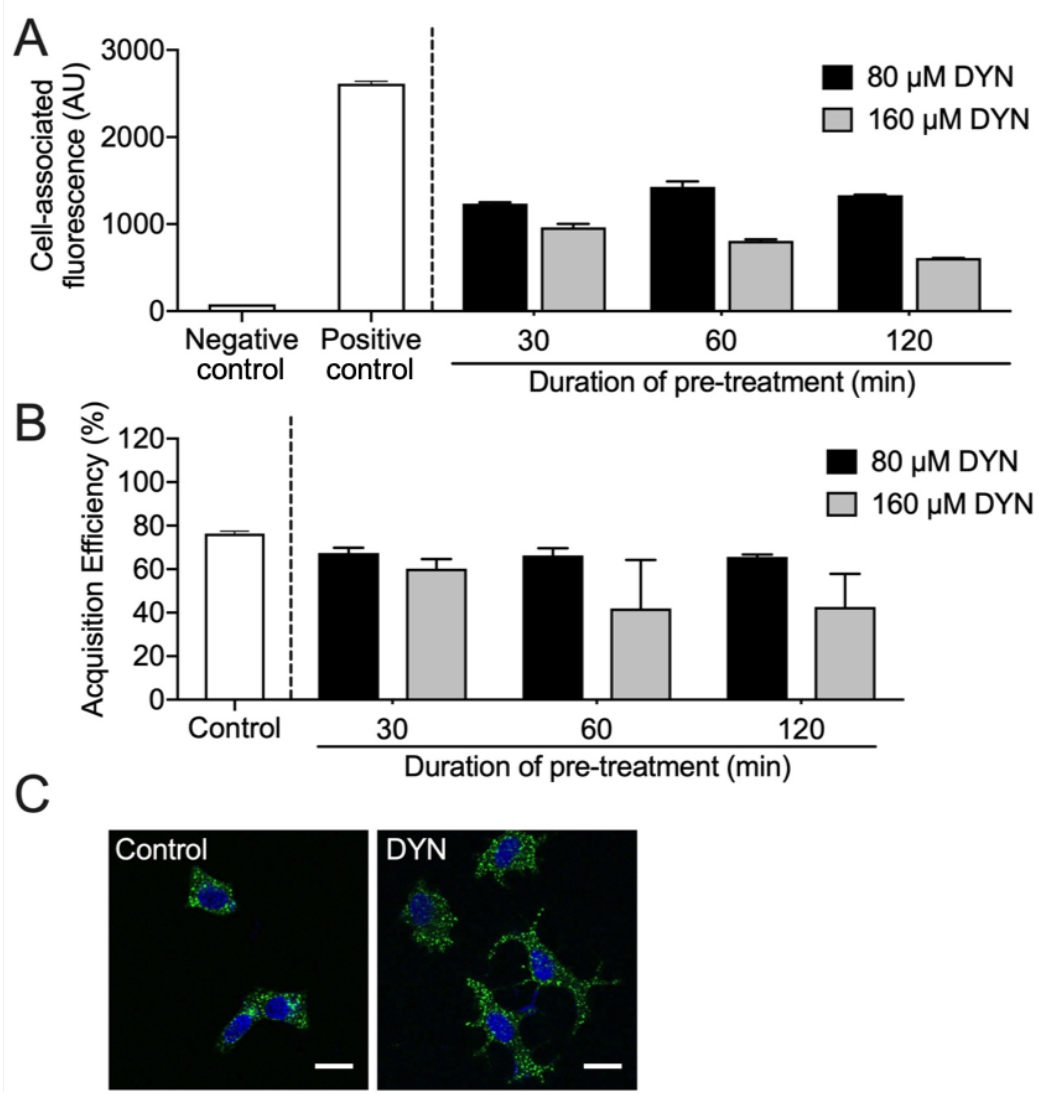

Figure 5.4. Dynasore is an inefficient tool for long term inhibition of dynamin-dependent endocytosis in MCF-7 cells. (A) Pre-treatment of MCF-7 cells for 30, 60 or 120 minutes with 80 μM or 160 μM dynasore followed by a 30 minute dose with 5 μg/mL transferrin (Tf). (B) Effects of these conditions on acquisition efficiency during flow cytometry. (C) Representative confocal images of MCF-7 cells following a 30 minute dose with transferrin without (left) or with (right) a 30 minute dynasore (80 μM) pre-treatment. Scale bars: 20 μm.

RNA interference was also used to inhibit clathrin-mediated endocytosis and siRNA against AP-2 was selected as it effectively knocks down clathrin-mediated endocytosis without introducing adverse intracellular effects.[287,288] In MCF-7 cells, siRNA inhibition of AP-2 prevented the internalisation of transferrin into intracellular vesicles (Figure 5.5). This was observed using confocal microscopy as transferrin was observed to accumulate on the surface of cells without being internalised into vesicles. In contrast, control siRNA GFP knock down cells displayed endocytosis of transferrin into vesicles and confirmed that the observed effects were specifically the result of AP-2 knock down.

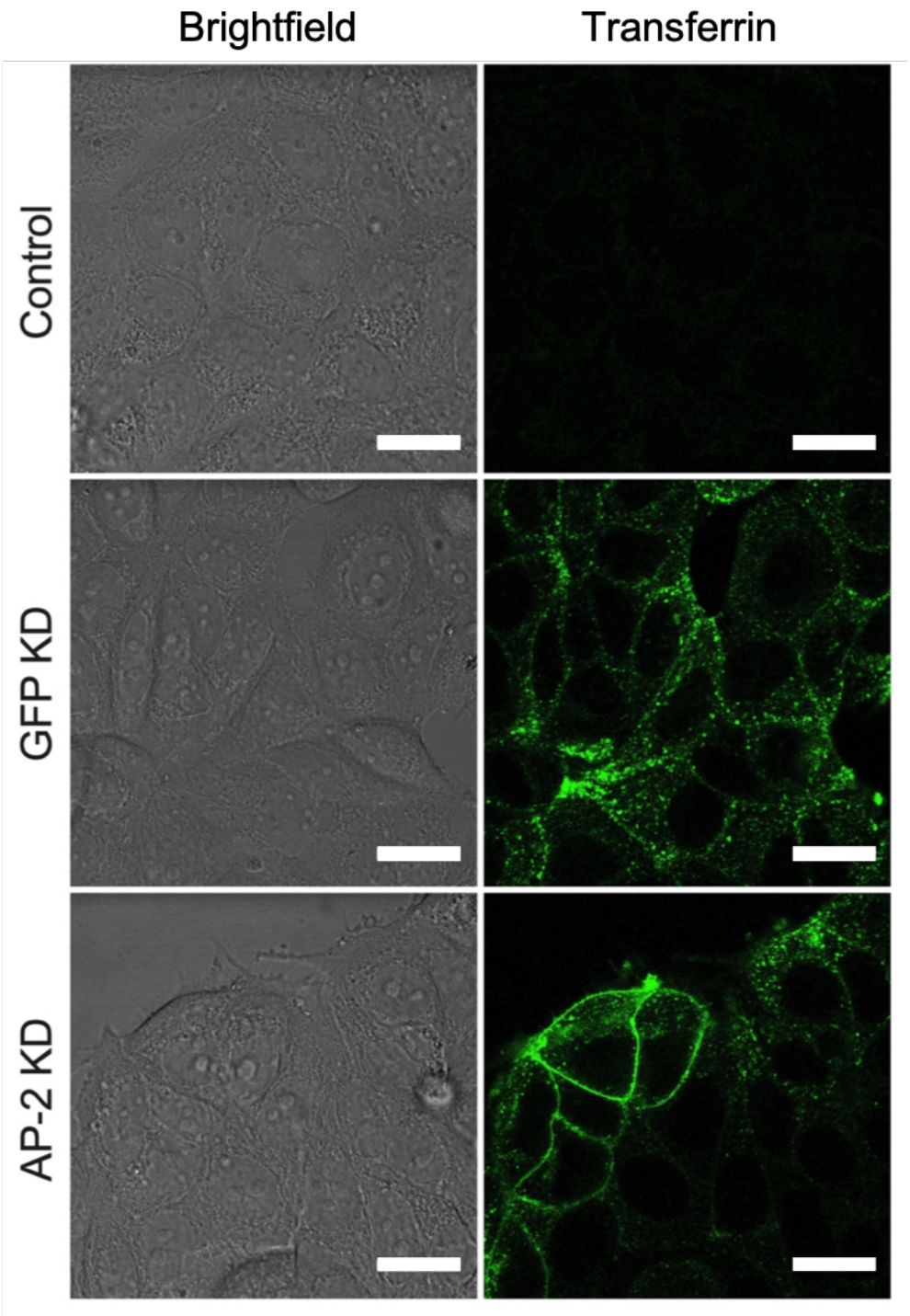

Figure 5.5. Inhibition of clathrin-mediated endocytosis in MCF-7 cells. Representative confocal slices showing endocytosis of AF488-labelled transferrin in MCF-7 cells following siRNA knock down of GFP (control) or AP-2 using dharmacon smart pool siRNA. Scale bars: 30 μm.

5.3.3. Intracellular trafficking of unmodified and PEGylated silk fibroin nanoparticles

Cell surface binding (1 hour, 4 °C) and endocytosis of unmodified (Figure 5.6) and PEGylated (Figure 5.7) silk fibroin nanoparticles at early (2 hours), intermediate (5 hours) and late (24 hours) timepoints was assessed using a combination of live confocal microscopy and flow cytometry. Mander's co-localisation tests were conducted on zoomed confocal images to calculate co-localisation coefficients between dextran-labelled vesicles and nanoparticles under each condition.

Confocal microscopy analyses revealed that unmodified silk fibroin nanoparticles formed aggregates that bound the cell-membrane binding following a 1 hour dose at 4 °C (Figure 5.6 A), whilst PEGylated silk fibroin nanoparticles appeared to exhibit substantially less membrane binding under the same conditions. Manders co-localisation coefficients of 0.0034 and 0.016 were calculated respectively for unmodified and PEGylated silk fibroin nanoparticles (numbers imposed on images), revealing very low association between endosomes and nanoparticles under these conditions. At the first 37 °C timepoint investigating early (2 hour) intracellular trafficking, both unmodified and PEGylated silk fibroin nanoparticles were observed to colocalise with dextran-labelled vesicles, as Manders coefficients of 0.586 and 0.583 were calculated respectively for unmodified and PEGylated silk fibroin nanoparticles. Similar co-localisation results were observed at the moderate (5 hour) time-point, unmodified and PEGylated silk fibroin nanoparticles producing respective Manders coefficients of 0.584 and 0.508. At the late time-point (24 hour) nanoparticles were found to persist in endo-lysosomal vesicles, with co-localisation analyses

yielding an increase in overall co-localisation (Manders coefficients of 0.927 and 0.691 respectively, for unmodified and PEGylated silk fibroin nanoparticles).

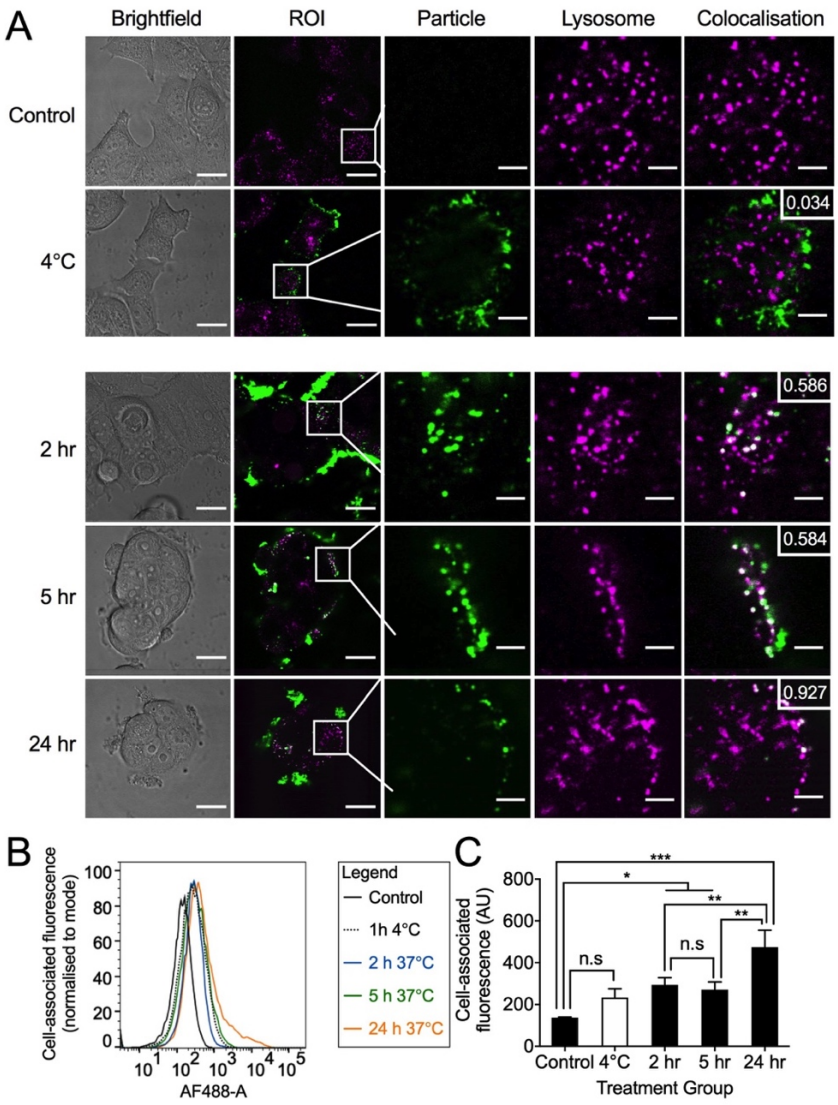

Figure 5.6. Time-dependent endocytosis and intracellular trafficking of unmodified silk fibroin nanoparticles. (A) Representative confocal microscopy images showing colocalisation of unmodified silk fibroin nanoparticles with dextran-loaded endosomes and lysosomes. Manders coefficient for colocalisation shown in boxes. (B) Flow cytometry histograms of MCF-7 cell-associated fluorescence following time-dependent treatment with unmodified silk fibroin nanoparticles. (C) Time dependent shifts in cell-associated fluorescence determined by flow cytometric analyses. Scale bars: brightfield and ROI: 20 μm; particle, lysosome and colocalisation: 4μm.

Flow cytometry analyses provided quantitative data on cell-associated fluorescence under the same conditions and revealed differential fluorescent profiles depending on nanoparticle treatment. At 4 °C, nanoparticle binding to single cells was measured and unmodified silk fibroin nanoparticles were found to increase cell-associated fluorescence of MCF-7 cells, however this was not found to be significant ($P > 0.05$). At the early (2 hour) and intermediate (5 hour) time-points, cell-associated fluorescence was significantly ($P < 0.05$) higher than untreated cells. However, no statistically relevant differences were observed between the two 37 °C endocytosis groups and the 4 °C binding group (Figure 5.6 C). Cell-associated fluorescence at the late time-point was significantly higher than the early and intermediate time-points ($P < 0.01$), supporting the microscopy findings that observed intracellular persistence after 24 hours.

When PEGylated SNP treatment was measured by flow cytometry, results from the 4 °C treatment differed significantly ($P < 0.05$) to untreated controls (Figure 5.7 C). In contrast to the time-dependent profile observed for unmodified silk fibroin nanoparticles, PEGylated silk fibroin nanoparticles showed a significant increase in cell-associated fluorescence ($P < 0.01$) at the early time point when compared to the 4 °C treatment group. However, shifts in cell-associated fluorescence were less pronounced at both of the later time-points (Figure 5.7 C). A subsequent experiment measuring cell-associated fluorescence in the presence of NH_4Cl revealed that lysosomal acidity significantly ($P < 0.001$) affected the measured cell-associated fluorescence of MCF-7 cells treated with PEGylated silk fibroin nanoparticles (Figure 5.8).

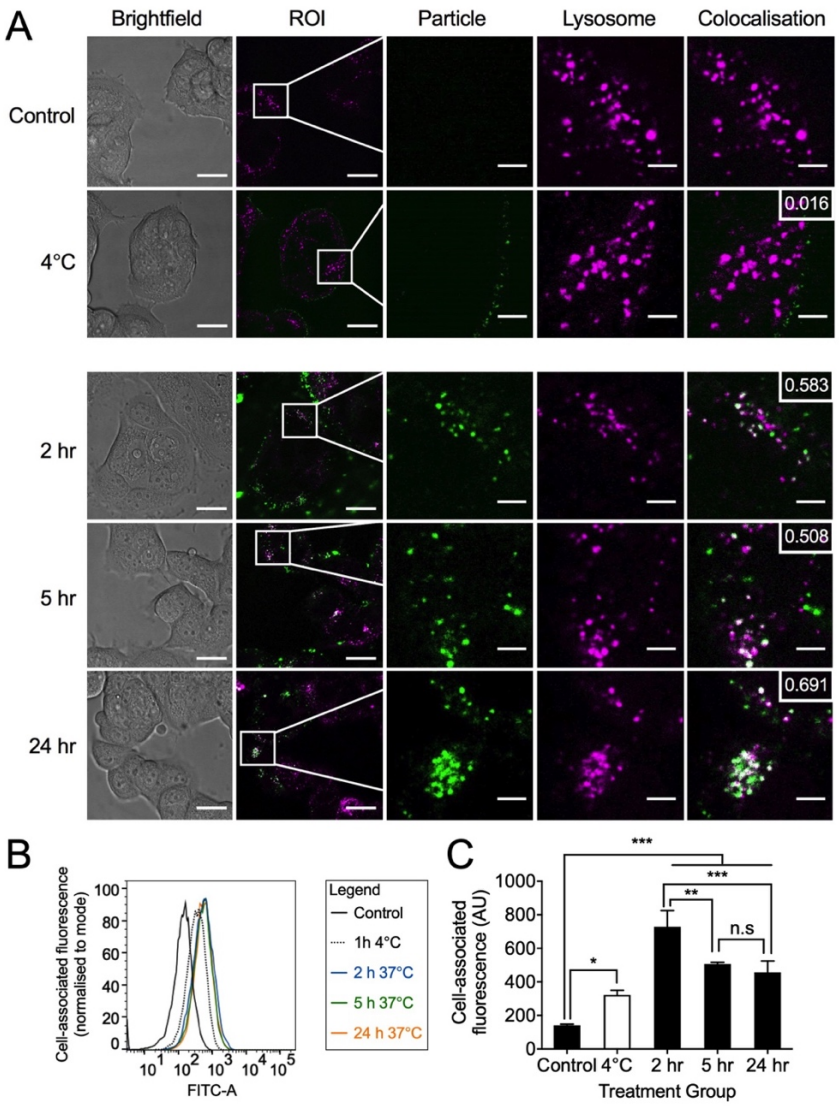

Figure 5.7. Time dependent endocytosis and intracellular trafficking of PEGylated silk fibroin nanoparticles. (A) Representative confocal microscopy images showing colocalisation of PEGylated silk fibroin nanoparticles with dextran-loaded endosomes and lysosomes. Manders coefficient for colocalisation shown in boxes. (B) Flow cytometry histograms of MCF-7 cell-associated fluorescence following time-dependent treatment with PEGylated silk fibroin nanoparticles. (C) Time dependent shifts in cell-associated fluorescence determined by flow cytometric analyses. Scale bars: brightfield and ROI: 20 μm; particle, lysosome and colocalisation: 4μm.

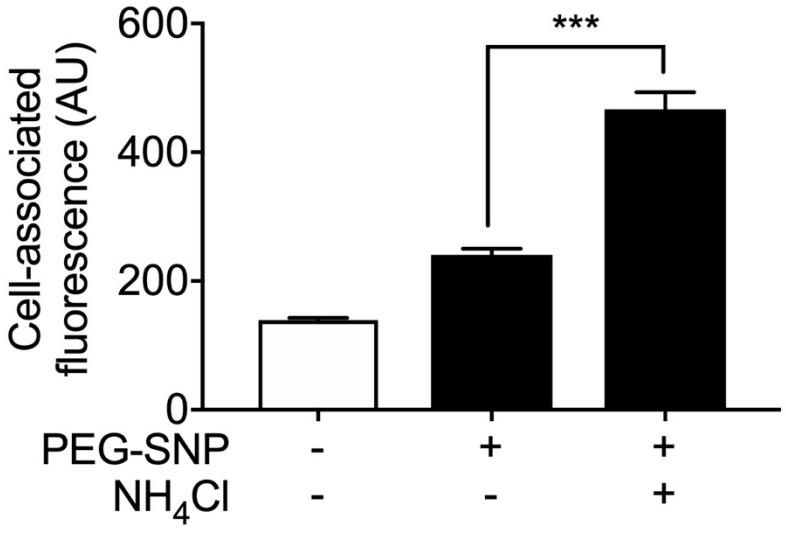

Figure 5.8. Lysosomal quenching of FITC-PEGylated silk fibroin nanoparticles significantly impacts cell-associated fluorescence readings. MCF-7 cells were untreated or dosed for 24 h with PEGylated silk fibroin nanoparticles. Before harvesting for flow cytometric analyses, cells were left untreated or pre-treated for 1 h with 10 mM NH_4Cl to inhibit lysosomal acidification of pH. (n = 3)

5.3.4. Effects of cell cycle on interactions with unmodified and PEGylated silk fibroin nanoparticles

Cell-specific factors affecting endocytosis of silk fibroin nanoparticles within a population were considered by investigating whether the state of cell division influenced nanoparticle-cell interactions. MCF-7 cells were exposed to unmodified and PEGylated silk fibroin nanoparticles for early (2 hr), intermediate (5 hr) and late (24 hr) time-points, then permeabilised and stained with 7-AAD as a cell cycle stain

prior to acquisition on the flow cytometer. Events were acquired and gated accordingly to identify cells based on progression through the cell cycle (Figure 5.9A).

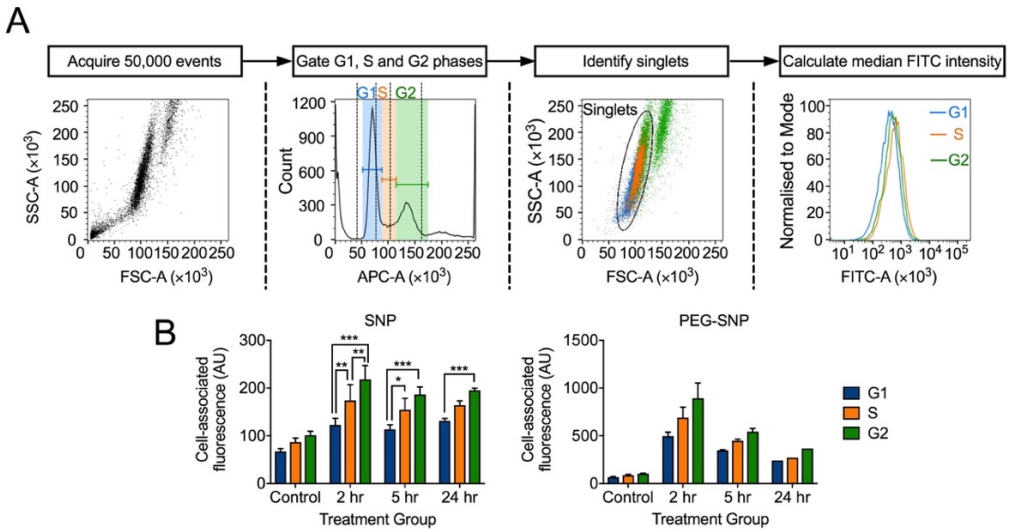

Figure 5.9. MCF-7 cells display cell-cycle dependent differences in endocytosis of unmodified (SNP) and PEGylated (PEG-SNP) silk fibroin nanoparticles. (A) Schematic depicting the gating strategy used to identify stages of cell cycle. (B) Median cell associated fluorescence shifts observed between G1, S and G2 phase populations at each time point following dosing with unmodified of PEGylated silk fibroin nanoparticles. (SNP treated; n = 3. PEG-SNP treated; n = 2).

Cell-cycle dependent differences in cell-associated fluorescence of MCF-7 cells were noted regardless of SNP treatment type (Figure 5.9 A, B). In cells treated with unmodified silk fibroin nanoparticles for 2 hours the median cell-associated fluorescence at G2 phase was significantly higher than cells at the G1 ($P < 0.001$) or S ($P < 0.01$) phases of the cell cycle. Similar trends were observed at the 5 and 24 hour time points (Figure 5.9 A), and at all time points in cells treated with PEGylated silk fibroin nanoparticles (Figure 5.9 B).

5.3.5. Production of stiffness-tubeable poly(acrylamide) hydrogels for breast tumour stiffness mimicry

PA hydrogels were produced with varying stiffness (Figure 5.10 A) using the sandwich coverslip method (Figure 5.10 B) and functionalised with type-1 collagen (Figure 5.11).

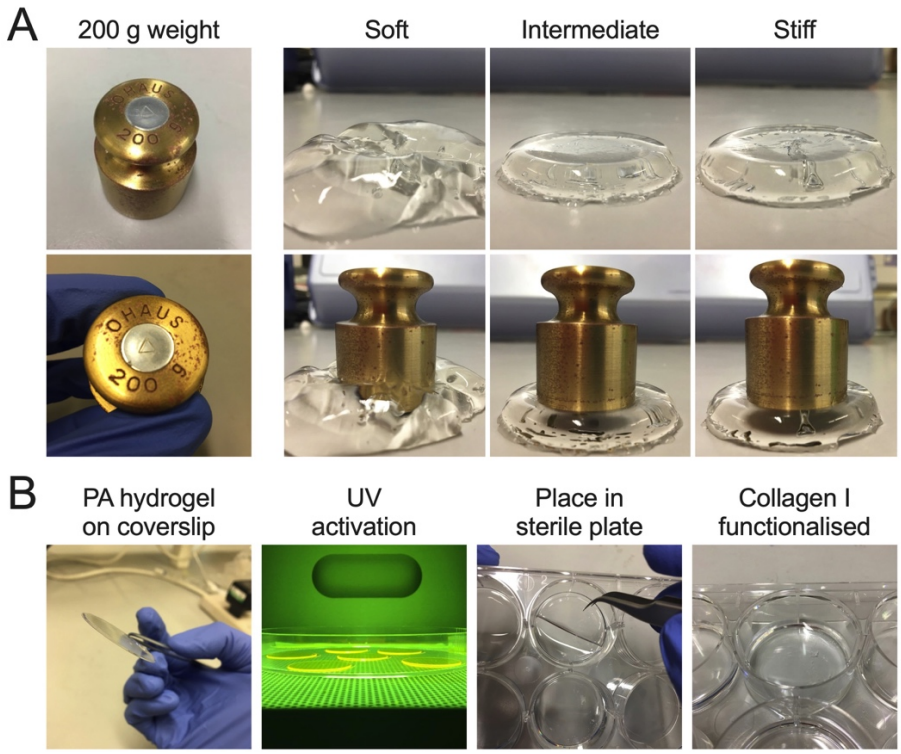

Figure 5.10. Production of stiffness-tuneable PA hydrogels for breast tumour stiffness mimicry. (A) Representative images of 200 g weight and PA hydrogels with soft (0.5 kPa), intermediate (5 kPa) and stiff (10 kPa) elastic moduli. Gels were imaged alone, or with 200 g weight on top to demonstrate differences in gel stiffness. (B) Representative images of PA hydrogels (i) on coverslips, (ii) undergoing UV activation and (iii) being placed in 6 well plates for collagen functionalisation.

Successful functionalisation of PA hydrogels with type 1 collagen was verified by immunostaining the gel surface with an AF488- labelled anti-COLL-1 monoclonal antibody (Figure 5.11). Collagen functionalisation was successful across a range of elastic moduli (0.5 kPa, 5 kPa and 10 kPa). However, the morphology of collagen depositions differed depending on the gel stiffness.

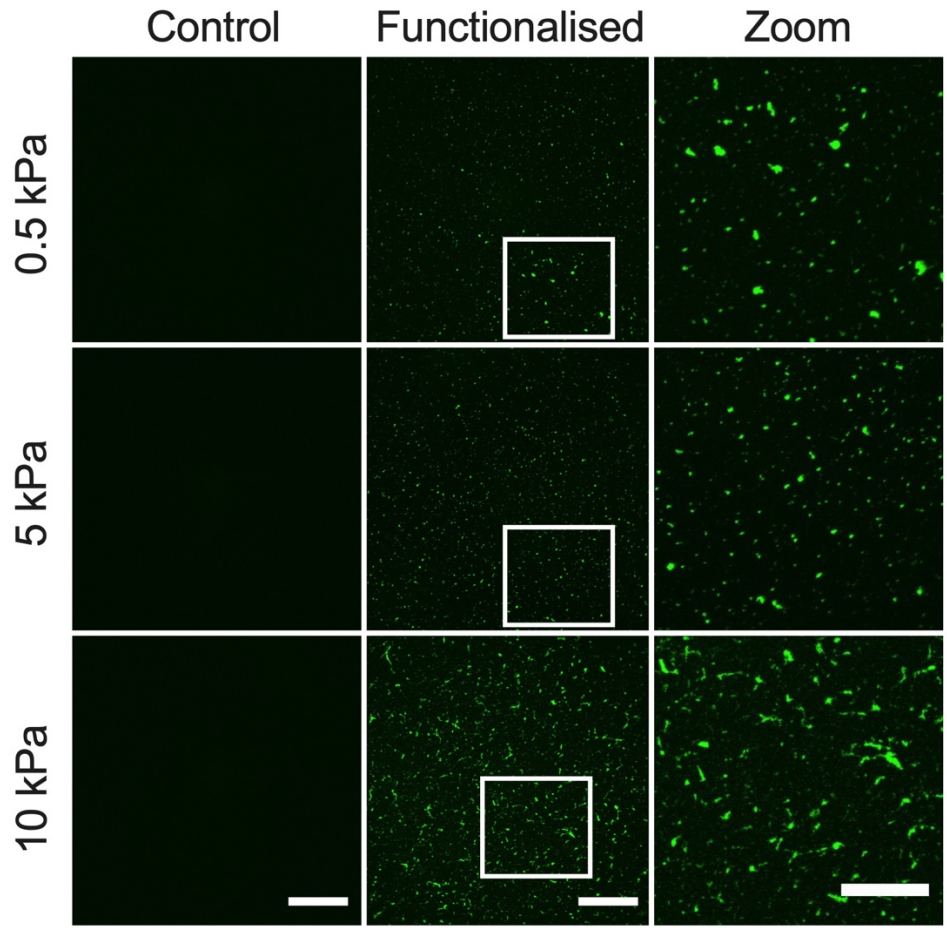

Figure 5.11. Functionalisation of poly(acrylamide) hydrogels with type-I collagen. Representative confocal slices of control and collagen-functionalised poly(acrylamide) hydrogels (0.5 kPa – 10 kPa) stained with AF488-labelled anti-COLL-1 antibody. Squares: zoomed regions of interest. Scale bars: left = 80 μm, zoom = 40 μm. (n = 1).

5.3.6. Cell adhesion and biocompatibility of stiffness tuneable poly(acrylamide) hydrogels

Having assembled collagen functionalised PA hydrogels, it was important to determine whether observed differences in collagen functionalisation affected cell adhesion and proliferation. Three cell lines representing healthy (MCF-10A), metastatic (MCF-7) and triple-negative (MDB-MB-231) breast epithelial cells were selected and the resazurin assay was used to assess cell viability 24 or 72 hours post seeding (Figure 5.12 A, B). Cells cultured on glass or polystyrene were included as controls and cell viability was normalised to the polystyrene cultured control as it represented the industry standard for cell culture. After 24 hours, all cell lines displayed a reduction in metabolism of resazurin when cultured on the soft hydrogels (elastic moduli: 0.5 – 1.8 kPa). Cells cultured on stiffer PA hydrogels (elastic moduli 2.5 – 10 kPa) showed no difference in cell viability (Figure 5.12 A).

At 72 hours post seeding, MCF-10A cells cultured on 0.5 and 1.1 kPa hydrogels displayed significant ($P < 0.01$) and substantial reductions in cell viability, respectively. In contrast, cell viability of MCF-7 and MDA-MB-231 cells was largely unchanged at the 72 hour time point with the exception of a small but significant ($P < 0.05$) decrease in MCF-7 cell viability when cultured on the 5 kPa hydrogels.

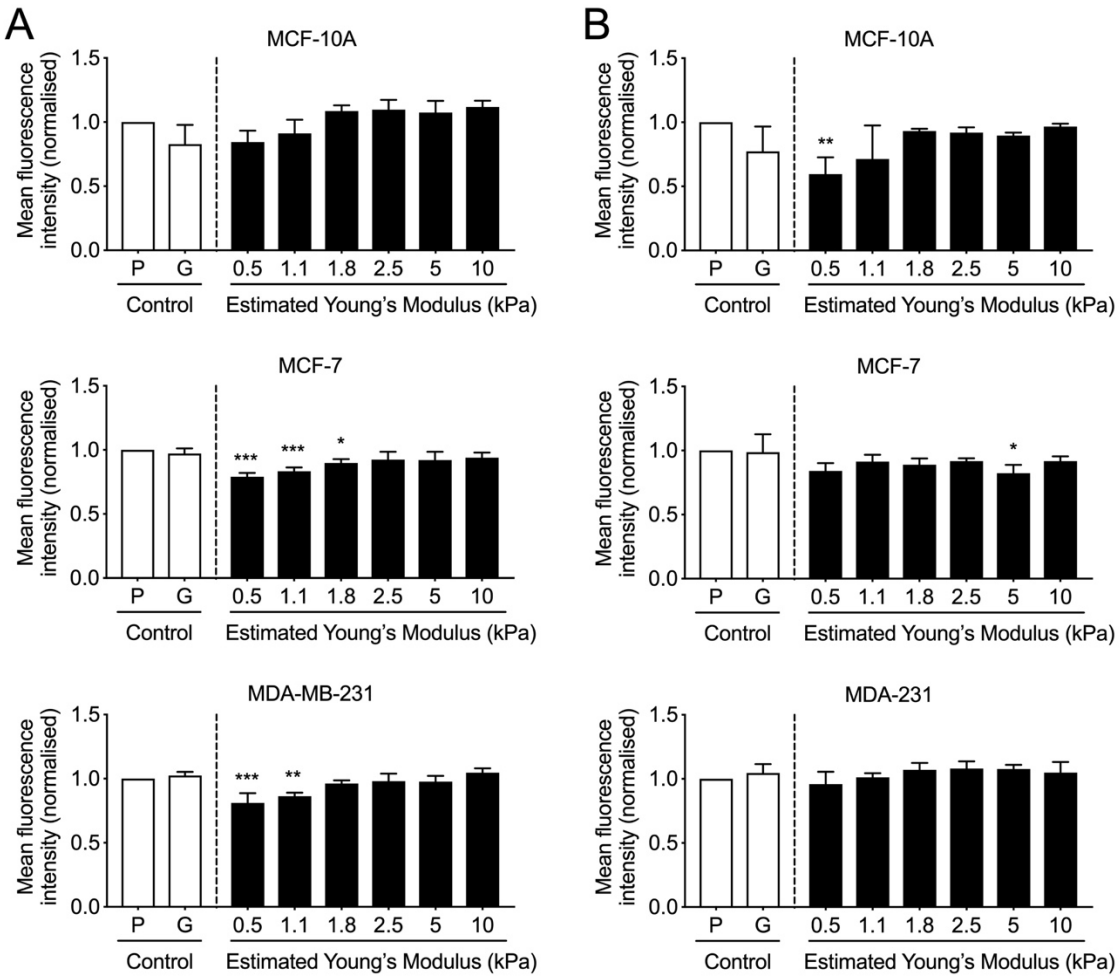

Figure 5.12. Adhesion and proliferation profiles of breast epithelial cells cultured on PA hydrogels. MCF-10A, MCF-7 and MCF-10A cells were seeded at 2×10^4 cells/cm^2 onto polystyrene (P), glass (G) or PA hydrogels of increasing elasticity (0.5 kPa – 10 kPa). Cells were dosed for 4 h with resazurin after (A) 24 h, or (B) 72 h, and overall metabolism of resazurin by each population was taken as an indicator of cell viability. (One-way ANOVA with Bonferroni post-hoc test between polystyrene and gel-cultured cells: *, $P < 0.05$; **, $P < 0.01$; ***, $P < 0.001$) (n = 3)

5.3.7. Effects of substrate stiffness on endocytosis of nanoparticles

A key aim of this chapter was to investigate the effects of substrate stiffness on the endocytosis of nanoparticles. Commercially available 100 nm latex nanoparticles were purchased a model nanomedicine and their cytotoxicity was measured in healthy (MCF-10A) and metastatic (MCF-7) human breast cells using the MTT assay (Figure 5.13). Following a 72 hour dose with latex nanoparticles (0 – 5 mg/mL) in complete medium, MCF-10A cell viability remained until exposure reached very high concentrations (>1 mg/mL). 5 mg/mL latex nanoparticles found to significantly ($P < 0.05$) affect cell viability in these cells and this concentration was noted as the IC50. MCF-7 cells tolerated latex nanoparticle treatment better than MCF-10A cells, with cell viability remaining relatively unchanged in concentrations up to 5 mg/mL.

Next, the effects of substrate stiffness on the endocytosis of latex nanoparticles was determined using flow cytometry. MCF-10A, MCF-7 and MDA-MB-231 were cultured for 72 hours on PA hydrogels (elastic moduli: 0.5 – 20 kPa) and then dosed for 60 minutes in complete growth medium supplemented with latex nanoparticles (20 μg/mL). Cells were then detached and cell-associated fluorescence values were measured by flow cytometry for each cell line under different culture conditions (Figure 5.14). Untreated control cells were used to determine cellular autofluorescence and polystyrene cultured cells provided an indication of endocytic behaviour when cultured using traditional means.

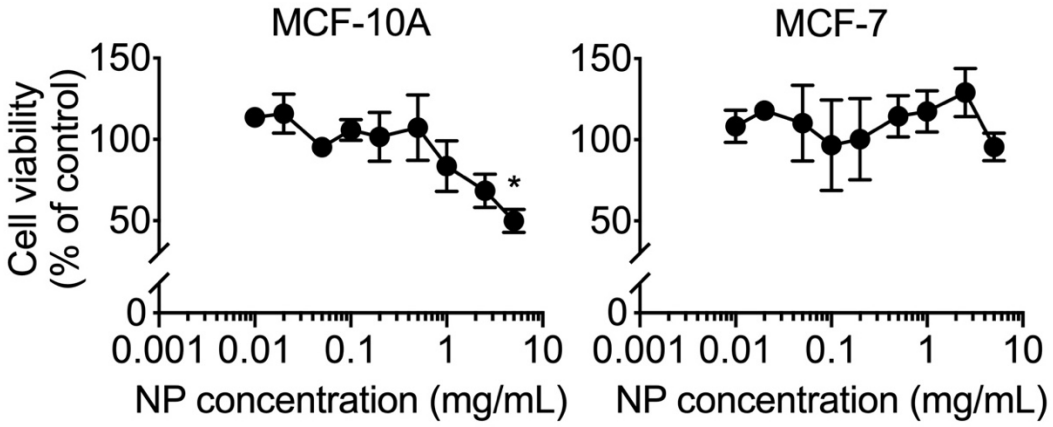

Figure 5.13. *In vitro* cytotoxicity of latex nanoparticles in healthy and metastatic breast epithelial cells. MCF-10A and MCF-7 cells seeded at 2×10^4 cells/cm^2 and incubated for 72 hours with 0 – 5 mg/mL latex nanoparticles. Cytotoxicity measured by MTT assay. (One-way ANOVA with Bonferroni post-hoc test between untreated and nanoparticle treated groups: *, $P < 0.05$) (n = 3, mean ± S.E.M).

Endocytosis of latex nanoparticles by MCF-10A cells appeared to be sensitive to changes in substrate stiffness (Figure 5.14 A). When cultured on substrates that were very soft (elastic moduli 0.5 and 1.1 kPa), cell-associated fluorescence decreased slightly when compared to cells cultured on tissue-culture polystyrene. In contrast, MCF-10A cells cultured on stiff substrates (i.e. 5 kPa and 10 kPa) significantly ($P < 0.01$ and $P < 0.001$, respectively) higher cell-associated fluorescence was evident. MCF-7 and MDA-MB-231 cells displayed substrate sensitive increases in cell-associated fluorescence when cultured on PA hydrogels, compared with culture on tissue-culture polystyrene (Figure 5.14 B, C), yet no significant differences were observed between cells cultured on hydrogels of different elasticity. Between different cell lines, the cell-associated fluorescence of latex nanoparticle treated cells also varied

substantially, with fluorescence readings for MCF-7 cells being higher than MCF-10A cells, and MDA-MB-231 cells substantially higher again.

It was important to verify if the cell-associated fluorescence readings measured by flow cytometry were representative of endocytosed latex nanoparticles or a combination of intracellular and surface bound latex nanoparticles. To do this, MCF-7 cells were cultured on PA hydrogels that were 0.5 kPa, 5 kPa or 10 kPa and treated for 60 minutes with latex nanoparticles (20 μg/mL) as described above. Cells were detached and prepared for flow cytometry under the same conditions as before but were instead imaged by confocal microscopy to locate the source of cell-associated fluorescence (Figure 5.15). MCF-7 cells displayed a round morphology due to detachment and cell-associated fluorescence found to be exclusively within intracellular vesicular organelles, indicating that flow cytometry analyses measured endocytosed material rather than surface-bound latex nanoparticles.

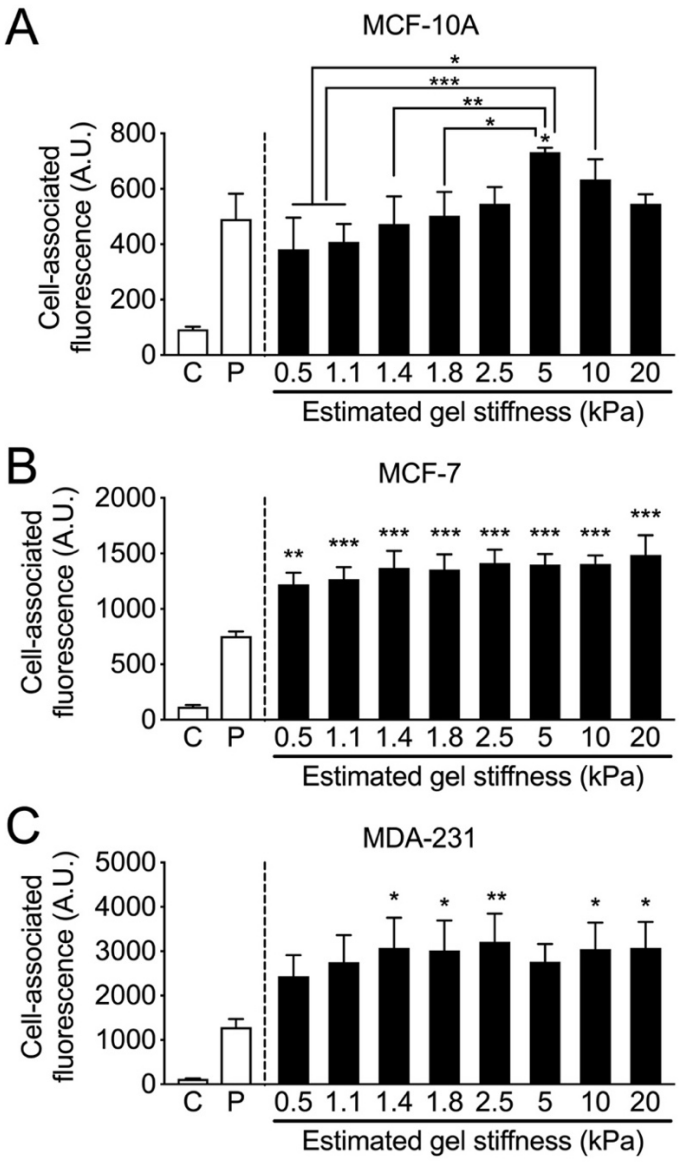

Figure 5.14. Endocytosis of nanoparticles is influenced by substrate stiffness in some breast epithelial cell lines. Cell-associated fluorescence of (A) MCF-10A, (B) MCF-7 and (C) MDA-MB-231 cells when cultured for 72 hours on collagen-functionalised PA hydrogels and then dosed for 60 minutes with 20 μg/mL latex nanoparticles. Elastic moduli of gels were within the range of 0.5 – 20 kPa. (One-way ANOVA with Bonferroni post-hoc test between 0.5 kPa and remaining gels: **, $P < 0.01$; ***, $P < 0.001$) (n = 3). C = untreated control, P = polystyrene dosed

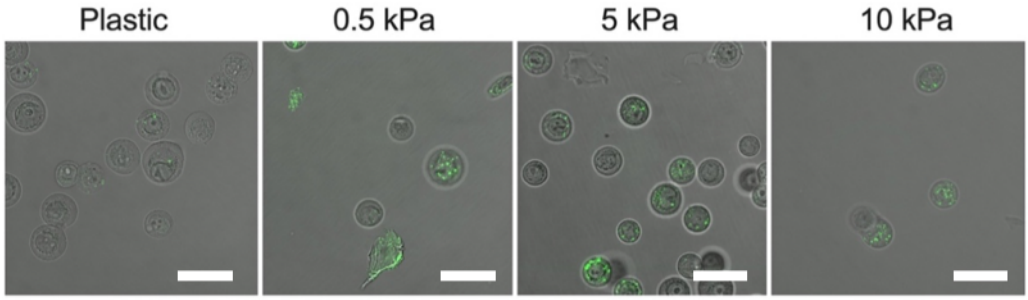

Figure 5.15. Confocal analysis of cells prior to analysis by flow cytometry. MCF-7 cells cultured on polystyrene or PA hydrogels with elastic moduli of 0.5 kPa, 5 kPa and 10 kPa. Cells were dosed for 60 minutes with 20 μg/mL latex nanoparticles, harvested for flow cytometry analyses, and then live-imaged immediately. Scale bar 40 μm. (n = 1)

Attempts were also made to measure the effects of substrate stiffness on endocytosis of unmodified and PEGylated silk fibroin nanoparticles. MCF-7 cells were seeded at 2×10^4 cells/cm^2 onto tissue culture polystyrene or PA hydrogels that were 0.5 kPa, 5 kPa or 10 kPa and allowed to prime cells for 72 hours before being dosed in for 2 hours in serum free medium supplemented with AF488-silk fibroin nanoparticles (50 μg/mL) or FITC-PEG-SNPs (100 μg/mL). Untreated control cells were used to determine autofluorescence of MCF-7 cells. For both formulations cell-associated fluorescence increased incrementally with increasing substrate stiffness, suggesting a stiffness-dependent relationship (Figure 5.16 A). However, the observed increases in cell-associated fluorescence were small, and the flow cytometry histogram profiles revealed substantial overlap between NP-treated cells cultured on gels, and basal autofluorescence of polystyrene cultured MCF-7 cells (Figure 5.16 B). An additional positive control using FITC-labelled latex nanoparticles under the same conditions

found a clear difference in cell-associated fluorescence between untreated and nanoparticle-treated cells (Figure 5.16 B).

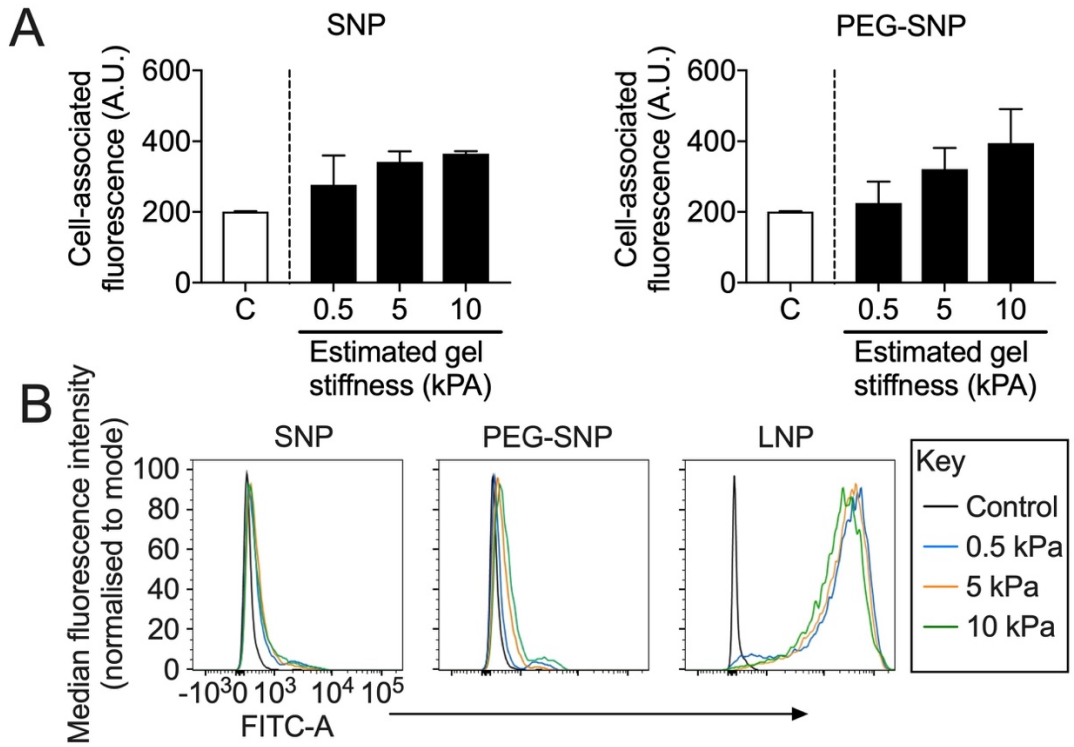

Figure 5.16. Stiffness-dependent endocytosis of unmodified and PEGylated silk fibroin nanoparticles. (A) Cell-associated fluorescence of MCF-7 cells when cultured for 72 h on collagen-functionalised PA hydrogels and then dosed for 2 h in serum-free medium with (i) 50 µg/mL unmodified (SNP) or (ii) 100 µg/mL PEGylated (PEG-SNP) silk fibroin nanoparticles. Untreated control (C) cells represent basal autofluorescence of cells. (B) Representative flow cytometry histograms highlighting differences in fluorescent shifts of MCF-7 cells depending on treatment with unmodified silk, PEGylated silk, or latex (LNP) nanoparticles. (n = 2).

5.4. Discussion

Unmodified and PEGylated silk fibroin nanoparticles were found to be well tolerated by breast epithelial cells in cytotoxicity studies (Figure 5.2) and this was consistent with previously published studies.[40,69]

Dynasore is a non-competitive chemical inhibitor of dynamin GTPases and is used extensively to investigate dynamin-dependent endocytosis pathways such as clathrin-mediated endocytosis and caveolae-mediated endocytosis.[283,285] Dynasore is used extensively when investigating endocytosis of nanomedicines and was selected for this study due to its well documented use and reproducibility.[283,286,289] In this study a, 30 minute pretreatment with 80 μM dynasore was ineffective at inhibiting endocytosis of transferrin in MCF-7 (Figure 5.3) as the maximum inhibition observed was 40.4% after only 5 minutes exposure to transferrin. At 30 minutes dynasore was only capable of inhibiting 11.4% of transferrin endocytosis and these results did not support a similar study conducted on A431 cells.[286] Increasing the concentration and duration of dose improved the inhibitory effects of dynasore (Figure 5.4 A). However, this also increased the difficulty of acquiring viable events in the flow cytometer, possibly due to the dynasore exposure having cytotoxic effects. In addition, the 30 minute pre-treatment at 80 μM markedly affected cell morphology when cells were imaged by confocal microscopy (Figure 5.4 C), further suggesting cytotoxic or off-target effects. Chemical inhibitors such as dynasore are well-documented to exhibit off-target intracellular effects,[290–292] often because the inhibitors also act on other essential intracellular pathways. In the case of dynasore, dynamin inhibition can affect actomyosin polymerisation which has marked effects on cytoskeletal structure and

intracellular trafficking.[293] Dynasore can also disrupt lipid raft organisation in the plasma membrane in a dynamin-independent manner,[294] further highlighting the off target affects associated with this chemical inhibitor.

RNA interference[286] was selected as an alternative to chemical inhibition of endocytosis because as it is highly specific to individual endocytic pathways and the use of siRNA depletion exhibits fewer off-target effects when compared to chemical inhibition.[292] Clathrin-mediated endocytosis was selected for endocytic knock down as it is the most well characterised mechanism of endocytic uptake and there are already dedicated methods to inhibit the process.[286] Whilst many studies have successfully demonstrated knock down of clathrin-mediated endocytosis using siRNA depletion of the clathrin heavy chain, this can introduce undesirable cellular effects due to the ubiquitous use of clathrin heavy chain in other cellular activities such as mitosis[295] and cell signalling.[296,297] As the purpose of conducting RNA interference was to reduce the instance of undesirable interactions, AP-2 depletion was selected as it is a more reliable inhibitor of clathrin mediated endocytiosis.[287,288] Again, MCF-7 cells were found to respond poorly to endocytic inhibition as confocal analyses of Tf-treated cells revealed low success rate of transfection.

Despite the setbacks inhibiting endocytic pathways in MCF-7 cells, it was still important to characterise intracellular trafficking in order to understand how efficiently silk fibroin nanoparticles use endocytosis to deliver payloads. Both unmodified and PEGylated silk fibroin nanoparticles were known to traffic to lysosomes within 5 hours from the lysosomotropic study conducted in chapter 3.[190] However, it was important to verify this again as the mechanism of PEGylation (FITC-

PEGylated) was slightly different in this study. As expected, both unmodified and PEGylated silk fibroin nanoparticles were found within dextran-labelled endosomes within 5 hours of dosing. To improve the understanding of unmodified silk fibroin nanoparticle intracellular trafficking, the time-points of 2 hours and 24 hours verified early endocytosis and retention within MCF-7 breast cancer cells and both unmodified and PEGylated silk fibroin nanoparticles were observed in endosomes at these time-points. Unfortunately, the failure of endocytic inhibition studies prevented further analysis on the mechanisms of entry for silk fibroin nanoparticles.

To assess heterogeneity in endocytosis within a population the effects of positioning in the cell cycle were considered as factors influencing endocytosis. The stage of cell division is known to affect the endocytosis of 40 nm latex nanoparticles in A549 cells, with cells in G2 phase being documented to endocytose more than cells in G1 or S phase.[279] In this study assessing unmodified silk fibroin nanoparticle (100 nm) endocytosis, uptake was highest in G2 phase, with a reduction in endocytosis observed in cells at S phase and the lowest uptake by cells at G1 phase of cell division (Figure 5.9 B, left), complementing the trends observed by Kim *et al.* A similar trend was observed for the uptake of PEGylated silk fibroin nanoparticles in a population of MCF-7 cells (Figure 5.9 B, right). Several reasons could account for these differences. For example, intracellular processes are vastly different between G1 (growth), S (DNA synthesis) and G2 (protein synthesis) phases and the rate of endocytosis is known to increase in cells at G2 phase as the process is essential for maintaining membrane integrity in before mitosis.[298–300] The increase in endocytosis of nanomedicines could therefore be caused by an increase in the inherent endocytic ability of dividing cells, compared with cells at an earlier stage of cell division. Regardless of the reasons for

this, the findings of this study indicate that silk fibroin nanoparticles are endocytosed more readily by cells about to undergo division, and this is a desirable feature for their application as an anticancer nanomedicine.

Nanoparticle and cell specific factors have been understood to influence nanomedicine uptake since the conception of lysosomotropic principles. However, the role of tumour microenvironmental factors such as the hypoxic environment[280] and ECM stiffening[177,179] are emerging as indirect regulators of nanoparticle endocytosis. Tumour stiffness is one of the primary diagnostic features of breast cancer,[169] and breast epithelial cells respond to microenvironmental stiffness to remodel breast tissue in non-disease states such as pregnancy.[301] A stiffness-tuneable hydrogel system was produced to culture cells on surfaces mimicking the stiffness of breast tissue in healthy and metastatic states. PA hydrogels with elastic moduli ranging from 0.5 kPa – 20 kPa were produced (Figure 5.10 A, B). Increased collagen deposition and cross-linking are known to drive ECM stiffening,[302] and so PA hydrogels were functionalised with type I collagen to more accurately model the microenvironmental conditions (Figure 5.11).

When the objectives of this chapter were set, a hydrogel model had never been used to assess endocytosis in breast cancer cells. However, a similar report[303] was published at the same time as data was acquired for this chapter (July 2017). Wang *et al.* assessed endocytosis of D-α-tocopheryl PEG-succinate micelles in MCF-7 and MDA-MB-231 cells over similar timepoints (5 – 60 minutes) and PA hydrogel stiffness ranges (1 – 25 kPa) to this study and was the first publication to assess substrate-dependent endocytosis in breast cancer. Whilst this substantially reduced the novelty of my study, it provided uniquely comparable datasets from which to validate my own findings.

MCF-10A, MCF-7 and MDA-MB-231 cells adhered to PA hydrogels within 24 hours of seeding (Figure 5.12). However, all cell lines displayed reductions in cell viability on soft (0.5 & 1.1 kPa) PA hydrogels when compared to stiff hydrogels (1.8 – 10 kPa). These differences were found to be not significant ($P > 0.05$). This was supported by Wang *et al.* in MCF-7 and MDA-MB-231 cells when cell viability at 24 hours was determined with Click-iT EdU flow cytometry.[303] After 72 hours, cell viability of MCF-10A cells cultured on soft (0.5 & 1.1 kPa) PA hydrogels was significantly lower than cells cultured on stiff hydrogels (1.8 – 10 kPa). The differences observed in MCF-10A cell viability may reflect a slower rate of proliferation rather than a cytotoxic effect at 72 hours, especially because MCF-7 and MDA-MB-231 cells showed fewer changes in cell viability when cultured on different PA hydrogel groups (Figure 5.12). This would support current opinion within the field of breast mechanobiology that breast epithelial cells lose their sensitivity to ECM stiffness as they undergo dedifferentiation and become more metastatic.[167]

Endocytosis of 100 nm latex nanoparticles was investigated in MCF-10A, MCF-7 and MDA-MB-231 cells following a 1 hour exposure and each cell line responded predictably based on their disease model (Figure 5.14). In MCF-10A cells, endocytosis of latex nanoparticles increased gradually when cultured on soft PA hydrogels (0.5 – 2.5 kPa) and significant increases to endocytosis were observed between MCF-10A cells cultured on soft and stiff substrates (Figure 5.14 A). Endocytosis by MCF-7 and MDA-MB-231 cells was significantly higher in cells cultured on PA hydrogels compared to polystyrene cultured cells. However, no significant differences were detected between cells cultured on PA hydrogels of different stiffness values (Figure 5.14 B, C). When this study was compared to Wang *et al.*, datasets for endocytosis

after 1 hour in MDA-MB-231 cells were supported by Wang's study. However, MCF-7 data was not supported as Wang *et al.* noted a small but significant ($P < 0.05$) decrease in endocytosis in cells cultured on soft (1 kPa) PA gels compared with cells cultured on stiff (7 – 25 kPa) PA gels.[303]

Wang *et al.*[303] published the first comprehensive study investigating the link between endocytosis of nanomedicines and substrate stiffness in breast cancer cells.[303] However, the performance of silk fibroin nanoparticles under these conditions was yet to be determined. The same hydrogel system was employed to investigate endocytosis of unmodified and PEGylated silk fibroin nanoparticles following a 2 hour dose under the same conditions used to assess silk fibroin nanoparticle uptake and trafficking earlier in this chapter. Similar to the results observed in the latex nanoparticle study and by Wang *et al.*, a slight increase in cell-associated fluorescence was observed between cells cultured on soft (0.5 kPa), intermediate (5 kPa) or stiff (10 kPa) PA hydrogels however, this was not found to be significant (Figure 5.16 A). A comparison of the flow cytometry histograms of unmodified silk fibroin nanoparticles, PEGylated silk fibroin nanoparticles and latex nanoparticles when dosed under these conditions revealed that both silk formulations only induced minimal changes to cell-associated fluorescence when compared to treatment with latex nanoparticles (Figure 5.16). As a high proportion of silk-treated cells were found to have similar cell-associated fluorescence profiles to untreated control cells, the differences were not considered biologically relevant and could be the result of insufficient fluorescent labelling of the particles.

5.5. Conclusions

This chapter demonstrated that MCF-7 cells are highly resistant to both chemical and RNA interference mechanisms to knock down endocytosis. As a result, the aim of elucidating the dependence of silk fibroin nanoparticles on clathrin-mediated endocytosis in tumour cells was not achieved. Intracellular trafficking profiles for unmodified and PEGylated silk fibroin nanoparticles in the absence of inhibitors, and both particles were found to co-localise with lysosomes within 2 hours of dosing and were retained over intermediate (5 hour) and long time-points (24 hour). Endocytosis of unmodified and PEGylated silk fibroin nanoparticles was found to be influenced by the target cell's position in the cell cycle, with a G2 > G1 > S profile being obtained. The effects of substrate stiffness on the endocytosis of latex nanoparticles in breast cancer cells was investigated using a stiffness-tuneable PA hydrogel model and cell lines representing healthy and metastatic epithelial cells. Increasing substrate stiffness drove increases to endocytosis in healthy breast epithelial cells, but this shift was less pronounced in metastatic breast epithelial cells. The substrate-stiffness model was also used to assess unmodified and PEGylated silk fibroin nanoparticle uptake. However, issues with fluorescent labelling of the nanoparticles hindered the acquisition of robust datasets and conclusions could not be drawn on this relationship.

Chapter 6: General Discussion and Conclusions

Chapter summary:

This chapter summarises the research outputs of the thesis including: (i) proof of lysosomotropic anticancer drug delivery from silk fibroin nanoparticles (Totten *et al.* 2017. J. Drug Target. 25, pp 865–872), (ii) immunogenic performance validation of silk fibroin nanoparticles (Saborano, Wongpinyochit, Totten, Johnston, Seib and Duarte. 2017. Adv. Healthc. Mater. 6, 1601240), and (iii) assessment of macrophage immunomodulation with silk fibroin nanoparticles (Totten *et al.* 2019. ACS Appl. Mater. Interfaces. in press). Unpublished findings silk fibroin nanoparticle endocytosis and intracellular trafficking are also reviewed. For future work, microfluidic nanoparticle assembly is proposed as a solution to improve nanoparticle drug loading and an interest in nanoparticle shape tuning to enhance circulatory performance is also expressed. The thesis is then brought to an overall conclusion.

6.1. General discussion

This thesis explored silk as a novel biopolymer for anticancer nanomedicine. The primary aim of the thesis was to validate the *in vitro* performance of silk fibroin nanoparticles and key objectives were selected to achieve this goal.

The first objective was to determine the dependence of silk fibroin nanoparticles on lysosomal function to mediate drug release (Chapter 3). Unmodified and PEGylated silk fibroin nanoparticles were loaded with a model breast cancer chemotherapy drug (doxorubicin) and pH and enzymatic activity were proven to trigger drug release by using simulated lysosomal conditions (e.g. adjusting pH and the model proteolytic enzyme papaïn).[190] Internalisation of silk fibroin nanoparticles by human breast cancer cells (MCF-7) was visualised by confocal microscopy, revealing that both unmodified and PEGylated silk fibroin nanoparticles trafficked to lysosomes within 5 hours of dosing. A combination of lysosomal acidity and enzymatic degradation facilitated drug release from the silk fibroin nanoparticles; this was evidenced by perturbation of lysosomal acidification and serine, cysteine and threonine protease activity using individual or a combination of chemical inhibitors.[190] Overall, combination inhibition resulted in a 42% ± 2.2% and 33% ± 3% reduction in nuclear-associated drug accumulation for unmodified and PEGylated silk fibroin nanoparticles, respectively. This provided the first direct evidence for silk fibroin nanoparticle-mediated lysosomotropic drug delivery in live cells at single cell resolution.[190]

The next objective (Chapter 4) was to assess the immunogenicity of silk fibroin nanoparticles in comparison to other materials currently in pre-clinical or clinical development. RAW 264.7 macrophages were exposed to silk, silica and PLGA

nanoparticles and the cellular response was assessed by monitoring both phenotypic and metabolic responses.[184] A combination of phenotypic (ELISA, immunostaining) and metabolic analyses were used to assess the polarisation of macrophages following nanoparticle dosing. Silk fibroin nanoparticles were found to induce only mild activation of macrophages; a response that was consistent with the wider literature on silk.[41,184] The activation profiles observed with silk fibroin nanoparticles were similar to that of silica and PLGA. The successful validation of silk fibroin nanoparticles immunogenicity provides a foundation for follow-on studies. However, instead of assessing their *in vivo* performance additional *in vitro* studies were conducted with the aim to better understanding silk fibroin nanoparticles as well as to regulate macrophage response.

The focus were particle-macrophage interactions because macrophages of the monocyte phagocytic system and tumour associated macrophages are recognised barriers to efficient tumour cell targeting (chapter 4). The inflammatory phenotype and metabolic profiles of macrophages exposed to unmodified or PEGylated silk fibroin nanoparticles were assessed. Macrophages showed a nanoparticle type dependent phenotypic and metabolic responses. Unmodified silk fibroin nanoparticles induced the upregulation of several processes, including production of proinflammatory mediators (e.g. cytokines), release of nitric oxide and promotion of antioxidant activity. These responses were accompanied by changes in the macrophage metabolomic profiles that were consistent with a proinflammatory state. By contrast, PEGylated silk fibroin nanoparticles induced milder changes to both inflammatory and metabolic profiles, suggesting that immunomodulation of macrophages with silk fibroin nanoparticles was PEGylation-dependent. Overall, PEGylation of silk fibroin

nanoparticles reduced the inflammatory and metabolic responses initiated by macrophages. This observation could be exploited to guide the future therapeutic applications of these nanoparticles.

Finally, the kinetics of silk fibroin nanoparticle endocytosis in breast cancer cells were assessed with a focus on elucidating the specific endocytic pathways used, producing intracellular trafficking profiles and determining factors that influence efficient nanoparticle uptake (chapter 5). Several attempts were made to investigate specific endocytic pathways in MCF-7 cells using chemical and siRNA interference techniques. However, these attempts were unsuccessful and this could be due to well documented variability in sensitivity of certain cell lines to endocytic inhibition.[290,304] Following on from the success of chapter 3 a more thorough investigation of the intracellular trafficking of silk fibroin nanoparticles was conducted. Time dependent confocal microscopy revealed that silk fibroin nanoparticles reach endosomes in MCF-7 cells within 2 hours of dosing and persist intracellularly at both 5 and 24 hours. Cell-associated fluorescence at each time point was influenced by tumour-cell cell cycle staging in a G2>G1>S dependent manner that was consistent with the wider literature.[279] This provided evidence of a heterogeneous cellular response to silk fibroin nanoparticles *in vitro*. Following on from this, ECM stiffness was considered as an external cellular modulator of nanoparticle endocytosis in breast cancer. Therefore, breast epithelial cell lines were cultured on collagen functionalised polyacrylamide hydrogels of varying elasticity. Once the cells were substrate primed, they were dosed with latex or silk fibroin nanoparticles. Substrate stiffness was documented to modulate endocytosis of latex nanoparticles in healthy, but not metastatic breast epithelial cells. However, attempts to implement the model with silk

fibroin nanoparticles ultimately failed due to limited fluorescence quantum yield of labelled silk fibroin nanoparticles. With the appropriate time and resources (i.e. refined particle engineering and labelling strategies), this study could be conducted again in the future to yield information that will be essential to fully understanding the factors influencing silk fibroin nanoparticle internalisation kinetics.

6.2. Future work

This project validated the performance of silk fibroin nanoparticles manufactured using a manual solvent nanoprecipitation method. Whilst this method is robust and reproducible, it is laborious and not suitable for up scaling. Therefore a scalable microfluidic manufacturing process was developed by colleagues and applied to silk fibroin nanoparticles.[305] I was involved in running preliminary biological validation of microfluidic-assembled silk fibroin nanoparticles.[305] The microfluidic system has now been optimised for future studies investigating the performance of silk fibroin nanoparticles. Based on the research outputs[184,190,223,305] and limitations of this study, I would expect this project to inform on future experimental design to validate the performance of silk fibroin nanoparticles *in vivo*. I therefore propose the implementation of microfluidic silk fibroin nanoparticle production for all future work packages investigating the (anticancer) applications of silk fibroin nanoparticles. A microfluidic system provides greater *in situ* control over particle characteristics. For example, anticancer drug(s) could be added to the microfluidic system during production to achieve superior drug loading (>4%w/w).[69] Improved loading is necessary before progressing silk fibroin nanoparticles into pre-clinical *in vivo* studies

(e.g. the orthotopic MDA-MB-231 breast cancer xenograft model).[306] Due to time constraints, it was not possible to explore microfluidic assembly of drug-loaded silk fibroin nanoparticles during this thesis. However, this will be an ideal starting point for future studies because the infrastructure and protocols are now in place.

A different, but exciting research avenue is to explore the impact of nanoparticle shape on function.; for example, how nanoparticle shape improves *in vivo* performance (e.g. pharmacokinetics, tumour targeting, endocytic uptake and trafficking). This thesis demonstrated the effectiveness of spherical, negatively charged silk fibroin nanoparticles and explored the effects of particle PEGylation. However, the effects of nanoparticle shape have never been explored using silk fibroin nanoparticles. Studies with other materials (see section 1.1.3) have shown that nanomedicines with tuned shape exert superior circulatory performance to spherical nanomedicines. Thus, there is a clear rationale for developing shaped silk nanomedicines in the future.

6.3. Conclusion

In summary, this thesis demonstrates that silk fibroin nanoparticles are readily internalised by tumour cells, traffic to lysosomes and deliver therapeutic payloads in a lysosomotropic manner. The endocytosis of silk fibroin nanoparticles by tumour cells was influenced by cell-specific factors such as cell cycle. However, microenvironmental influences such as ECM elasticity remain to be fully characterised. In off target "bystander" cells, silk fibroin nanoparticles displayed similar adjuvanticity to macrophages when compared to other leading nanomaterials and the activation potential of silk fibroin nanoparticles was found to be PEGylation-dependent. Overall, silk fibroin nanoparticles show interesting carrier features that are particularly promising in the anticancer drug delivery context. Future silk fibroin nanoparticle research will benefit from both the successes and failures that this project has encountered.

References

1. Duncan, R. & Richardson, S. C. W. Endocytosis and intracellular trafficking as gateways for nanomedicine delivery: Opportunities and challenges. *Mol. Pharm.* **9**, 2380–2402 (2012).

2. European Science Foundation. *Nanomedicine. An ESF–European Medical Research Councils (EMRC) Forward Look Report.* **1**, (2005).

3. Barenholz, Y. Doxil®--the first FDA-approved nano-drug: lessons learned. *J. Control. Release* **160**, 117–34 (2012).

4. Miele, E., Spinelli, G. P., Miele, E., Tomao, F. & Tomao, S. Albumin-bound formulation of paclitaxel (Abraxane ABI-007) in the treatment of breast cancer. *Int. J. Nanomedicine* **4**, 99–105 (2009).

5. Dinndorf, P. A., Gootenberg, J., Cohen, M. H., Keegan, P. & Pazdur, R. FDA drug approval summary: pegaspargase (oncaspar) for the first-line treatment of children with acute lymphoblastic leukemia (ALL). *Oncologist* **12**, 991–8 (2007).

6. Handelsman, Y. Role of Bile Acid Sequestrants in the Treatment of Type 2 Diabetes. *Diabetes Care* **34**, S244–S250 (2011).

7. Slatopolsky, E. A., Burke, S. K. & Dillon, M. A. RenaGel®, a nonabsorbed calcium- and aluminum-free phosphate binder, lowers serum phosphorus and parathyroid hormone. *Kidney Int.* **55**, 299–307 (1999).

8. Bushinsky, D. A. *et al.* Patiromer induces rapid and sustained potassium lowering in patients with chronic kidney disease and hyperkalemia. *Kidney Int.* **88**, 1427–1433 (2015).

9. Miller, A. *et al.* Treatment of multiple sclerosis with Copolymer-1 (Copaxone®): implicating mechanisms of Th1 to Th2/Th3 immune-deviation. *J. Neuroimmunol.* **92**, 113–121 (1998).

10. Duncan, R. & Gaspar, R. Nanomedicine(s) under the microscope. *Mol. Pharm.* **8**, 2101–2141 (2011).

11. Schroeder, A. *et al.* Treating metastatic cancer with nanotechnology. *Nat. Rev. Cancer* **12**, 39–50 (2011).

12. Matsumura, Y. & Maeda, H. A new concept for macromolecular therapeutics in cancer chemotherapy: mechanism of tumoritropic accumulation of proteins and the antitumor agent smancs. *Cancer Res.* **46**, 6387–6392 (1986).

13. Maeda, H., Wu, J., Sawa, T., Matsumura, Y. & Hori, K. Tumor vascular permeability and the EPR effect in macromolecular therapeutics: A review. *J. Control. Release* **65**, 271–284 (2000).

14. Golombek, S. K. *et al.* Tumor targeting via EPR: Strategies to enhance patient responses. *Adv. Drug Deliv. Rev.* **130**, 17–38 (2018).

15. Fujiwara, Y. *et al.* A multi-national, randomised, open-label, parallel, phase III non-inferiority study comparing NK105 and paclitaxel in metastatic or recurrent breast cancer patients. *Br. J. Cancer* **120**, 475–480 (2019).

16. Nakamura, H., Jun, F. & Maeda, H. Development of next-generation macromolecular drugs based on the EPR effect: challenges and pitfalls. *Expert Opin. Drug Deliv.* **12**, 53–64 (2015).

17. Blanco, E., Shen, H. & Ferrari, M. Principles of nanoparticle design for overcoming biological barriers to drug delivery. *Nat. Biotechnol.* **33**, 941–951 (2015).

18. Akbarzadeh, A. *et al.* Liposome: classification, preparation, and applications. *Nanoscale Res. Lett.* **8**, 102 (2013).

19. Bangham, A. D., Standish, M. M. & Watkins, J. C. Diffusion of univalent ions across the lamellae of swollen phospholipids. *J. Mol. Biol.* **13**, 238-IN27 (1965).

20. Gregoriadis, G. Drug entrapment in liposomes. *FEBS Lett.* **36**, 292–296 (1973).

21. Mayer, L. D. *et al.* Characterization of liposomal systems containing doxorubicin entrapped in response to pH gradients. *Biochim. Biophys. Acta* **1025**, 143–51 (1990).

22. Gabizon, A. *et al.* Prolonged circulation time and enhanced accumulation in malignant exudates of doxorubicin encapsulated in polyethylene-glycol coated liposomes. *Cancer Res.* **54**, 987–992 (1994).

23. Ringsdorf, H. Structure and properties of pharmacologically active polymers. *J. Polym. Sci. Polym. Symp.* **51**, 135–153 (1975).

24. Duncan, R. The dawning era of polymer therapeutics. *Nat. Rev. Drug Discov.* **2**, 347–60 (2003).

25. Duncan, R. Designing polymer conjugates as lysosomotropic nanomedicines. *Biochem. Soc. Trans.* **35**, 56–60 (2007).

26. Duncan, R. & Vicent, M. J. Polymer therapeutics-prospects for 21st century: the end of the beginning. *Adv. Drug Deliv. Rev.* **65**, 60–70 (2013).

27. Garrett, C. R. *et al.* Randomized phase 2 study of pegylated SN-38 (EZN-2208) or irinotecan plus cetuximab in patients with advanced colorectal cancer. *Cancer* **119**, 4223–4230 (2013).

28. Ibrahim, N. K. *et al.* Multicenter phase II trial of ABI-007, an albumin-bound paclitaxel, in women with metastatic breast cancer. *J. Clin. Oncol.* **23**, 6019–26 (2005).

29. Petros, R. a & DeSimone, J. M. Strategies in the design of nanoparticles for therapeutic applications. *Nat. Rev. Drug Discov.* **9**, 615–627 (2010).

30. Suk, J. S., Xu, Q., Kim, N., Hanes, J. & Ensign, L. M. PEGylation as a strategy for improving nanoparticle-based drug and gene delivery. *Adv. Drug Deliv. Rev.* **99**, 28–51 (2016).

31. Truong, N. P., Whittaker, M. R., Mak, C. W. & Davis, T. P. The importance of nanoparticle shape in cancer drug delivery. *Expert Opin. Drug Deliv.* **12**, 129–142 (2014).

32. Mu, L. & Feng, S. . A novel controlled release formulation for the anticancer drug paclitaxel (Taxol®): PLGA nanoparticles containing vitamin E TPGS. *J. Control. Release* **86**, 33–48 (2003).

33. Chawla, J. S. & Amiji, M. M. Biodegradable poly(ε-caprolactone) nanoparticles for tumor-targeted delivery of tamoxifen. *Int. J. Pharm.* **249**, 127–138 (2002).

34. Liu, P. *et al.* cRGD-functionalized mPEG-PLGA-PLL nanoparticles for imaging and therapy of breast cancer. *Biomaterials* **33**, 6739–47 (2012).

35. Slowing, I. I., Vivero-Escoto, J. L., Wu, C.-W. & Lin, V. S.-Y. Mesoporous silica nanoparticles as controlled release drug delivery and gene transfection carriers. *Adv. Drug Deliv. Rev.* **60**, 1278–88 (2008).

36. Sun, Y. & Xia, Y. Shape-controlled synthesis of gold and silver nanoparticles. *Science* **298**, 2176–9 (2002).

37. Ghosh, P., Han, G., De, M., Kim, C. K. & Rotello, V. M. Gold nanoparticles in delivery applications. *Adv. Drug Deliv. Rev.* **60**, 1307–15 (2008).

38. SUN, C., LEE, J. & ZHANG, M. Magnetic nanoparticles in MR imaging and drug delivery☆. *Adv. Drug Deliv. Rev.* **60**, 1252–1265 (2008).

39. Janes, K. A., Fresneau, M. P., Marazuela, A., Fabra, A. & Alonso, M. J. Chitosan nanoparticles as delivery systems for doxorubicin. *J. Control. Release* **73**, 255–267 (2001).

40. Wongpinyochit, T., Uhlmann, P., Urquhart, A. J. & Seib, F. P. PEGylated Silk Nanoparticles for Anticancer Drug Delivery. *Biomacromolecules* **16**, 3712–22 (2015).

41. Altman, G. H. *et al. Silk-based biomaterials*. *Biomaterials* **24**, 401–416 (2003).

42. Holland, C., Numata, K., Rnjak-Kovacina, J. & Seib, F. P. The Biomedical Use of Silk: Past, Present, Future. *Adv. Healthc. Mater.* **1800465**, 1800465 (2019).

43. Moy, R. L., Lee, A. & Zalka, A. Commonly used suture materials in skin surgery. *Am. Fam. Physician* **44**, 2123–8 (1991).

44. Haupt, J., García-López, J. M. & Chope, K. Use of a novel silk mesh for ventral midline hernioplasty in a mare. *BMC Vet. Res.* **11**, 58 (2015).

45. Fine, N. A. *et al.* SERI surgical scaffold, prospective clinical trial of a silk-derived biological scaffold in two-stage breast reconstruction: 1-year data. *Plast. Reconstr. Surg.* **135**, 339–51 (2015).

46. Administration, F. and D. November 2018 510(k) Clearances. (2018). Available at: https://www.fda.gov/MedicalDevices/ProductsandMedicalProcedures/DeviceApprovalsandClearances/510kClearances/ucm627939.htm. (Accessed: 2nd April 2019)

47. Watkins, R., Wu, L., Zhang, C., Davis, R. M. & Xu, B. Natural product-based nanomedicine: recent advances and issues. *Int. J. Nanomedicine* **10**, 6055–74 (2015).

48. Aigner, T. B., DeSimone, E. & Scheibel, T. Biomedical Applications of Recombinant Silk-Based Materials. *Adv. Mater.* **30**, 1704636 (2018).

49. Seib, F. P. & Kaplan, D. L. Silk for drug delivery applications: Opportunities and challenges. *Isr. J. Chem.* **53**, 756–766 (2013).

50. Perez-Rigueiro, J., Viney, C., Llorca, J. & Elices, M. Mechanical properties of single-brin silkworm silk. *J. Appl. Polym. Sci.* **75**, 1270–1277 (2000).

51. Zhou, C. Z. *et al.* Fine organization of Bombyx mori fibroin heavy chain gene. *Nucleic Acids Res.* **28**, 2413–9 (2000).

52. Zhou, C. Z. *et al.* Silk fibroin: structural implications of a remarkable amino acid sequence. *Proteins* **44**, 119–22 (2001).

53. Tanaka, K. *et al.* Determination of the site of disulfide linkage between heavy and light chains of silk fibroin produced by Bombyx mori. *Biochim. Biophys. Acta - Protein Struct. Mol. Enzymol.* **1432**, 92–103 (1999).

54. Lu, Q. *et al.* Silk Self-Assembly Mechanisms and Control From Thermodynamics to Kinetics. *Biomacromolecules* **13**, 826–832 (2012).

55. Jin, H. J. & Kaplan, D. L. Mechanism of silk processing in insects and spiders. *Nature* **424**, 1057–1061 (2003).

56. Seib, F. P. Silk nanoparticles-an emerging anticancer nanomedicine. *AIMS Bioeng.* **4**, 239–258 (2017).

57. Yamada, H., Igarashi, Y., Takasu, Y., Saito, H. & Tsubouchi, K. Identification of fibroin-derived peptides enhancing the proliferation of cultured human skin fibroblasts. *Biomaterials* **25**, 467–472 (2004).

58. Lu, S. *et al.* The influence of the hydrophilic–lipophilic environment on the structure of silk fibroin protein. *J. Mater. Chem. B* **3**, 2599–2606 (2015).

59. Wongpinyochit, T., Johnston, B. F. & Seib, F. P. Degradation Behavior of Silk Nanoparticles - Enzyme Responsiveness. *ACS Biomater. Sci. Eng.* **4**, 942–951 (2018).

60. Karp, N. *et al.* SERI Surgical Scaffold in 2-Stage Breast Reconstruction: 2-Year Data from a Prospective, Multicenter Trial. *Plast. Reconstr. surgery. Glob. open* **5**, e1327 (2017).

61. Thurber, A. E., Omenetto, F. G. & Kaplan, D. L. In vivo bioresponses to silk proteins. *Biomaterials* **71**, 145–157 (2015).

62. Rockwood, D. N. *et al.* Materials fabrication from Bombyx mori silk fibroin. *Nat. Protoc.* **6**, 1612–31 (2011).

63. Wang, Y. *et al.* In vivo degradation of three-dimensional silk fibroin scaffolds. *Biomaterials* **29**, 3415–3428 (2008).

64. Gil, E. S., Panilaitis, B., Bellas, E. & Kaplan, D. L. Functionalized Silk Biomaterials for Wound Healing. *Adv. Healthc. Mater.* **2**, 206–217 (2013).

65. Fernández-García, L. *et al.* Safety and tolerability of silk fibroin hydrogels implanted into the mouse brain. *Acta Biomater.* **45**, 262–275 (2016).

66. Thurber, A. E., Omenetto, F. G. & Kaplan, D. L. In vivo bioresponses to silk proteins. *Biomaterials* **71**, 145–157 (2015).

67. Uebersax, L. *et al.* Biocompatibility and osteoconduction of macroporous silk fibroin implants in cortical defects in sheep. *Eur. J. Pharm. Biopharm.* **85**, 107–118 (2013).

68. Seib, F. P. Silk nanoparticles—an emerging anticancer nanomedicine. *AIMS Bioeng.* **4**, 239–258 (2017).

69. Seib, F. P., Jones, G. T., Rnjak-Kovacina, J., Lin, Y. & Kaplan, D. L. pH-Dependent Anticancer Drug Release from Silk Nanoparticles. *Adv. Healthc. Mater.* **2**, 1606–1611 (2013).

70. Wongpinyochit, T., Johnston, B. F. & Seib, F. P. Manufacture and Drug Delivery Applications of Silk Nanoparticles. *J. Vis. Exp.* e54669–e54669 (2016). doi:10.3791/54669

71. Albanese, A., Tang, P. S. & Chan, W. C. W. The Effect of Nanoparticle Size, Shape, and Surface Chemistry on Biological Systems. *Annu. Rev. Biomed. Eng.* **14**, 1–16 (2012).

72. Vepari, C., Matheson, D., Drummy, L., Naik, R. & Kaplan, D. L. Surface modification of silk fibroin with poly(ethylene glycol) for antiadhesion and antithrombotic applications. *J. Biomed. Mater. Res. A* **93**, 595–606 (2010).

73. Murphy, A. R. & Kaplan, D. L. Biomedical applications of chemically-modified silk fibroin. *J. Mater. Chem.* **19**, 6443 (2009).

74. Canton, I. & Battaglia, G. Endocytosis at the nanoscale. *Chem. Soc. Rev.* **41**, 2718–39 (2012).

75. Tauber, A. I. Metchnikoff and the phagocytosis theory. *Nat. Rev. Mol. Cell Biol.* **4**, 897–901 (2003).

76. De Duve, C. The lysosome. *Sci. Am.* **208**, 64–72 (1963).

77. Doherty, G. J. & McMahon, H. T. Mechanisms of Endocytosis. *Annu. Rev. Biochem.* **78**, 857–902 (2009).

78. Conner, S. D. & Schmid, S. L. Regulated portals of entry into the cell. *Nature* **422**, 37–44 (2003).

79. Sorkin, A. & von Zastrow, M. Endocytosis and signalling: intertwining molecular networks. *Nat. Rev. Mol. Cell Biol.* **10**, 609–622 (2009).

80. Poon, I. K. H., Lucas, C. D., Rossi, A. G. & Ravichandran, K. S. Apoptotic cell clearance: basic biology and therapeutic potential. *Nat. Rev. Immunol.* **14**, 166–80 (2014).

81. Owens, D. E. & Peppas, N. A. Opsonization, biodistribution, and pharmacokinetics of polymeric nanoparticles. *Int. J. Pharm.* **307**, 93–102 (2006).

82. Flannagan, R. S., Jaumouillé, V. & Grinstein, S. The cell biology of phagocytosis. *Annu. Rev. Pathol.* **7**, 61–98 (2012).

83. Kinchen, J. M. & Ravichandran, K. S. Phagosome maturation: going through the acid test. *Nat. Rev. Mol. Cell Biol.* **9**, 781–95 (2008).

84. Wynn, T. A., Chawla, A. & Pollard, J. W. Macrophage biology in development , homeostasis and disease. *Nature* **496**, 445–455 (2013).

85. Maxfield, F. R. & McGraw, T. E. Endocytic recycling. *Nat. Rev. Mol. Cell Biol.* **5**, 121–132 (2004).

86. Grant, B. D. & Donaldson, J. G. Pathways and mechanisms of endocytic recycling. *Nat. Rev. Mol. Cell Biol.* **10**, 597–608 (2009).

87. Sahay, G., Alakhova, D. Y. & Kabanov, A. V. Endocytosis of nanomedicines. *J. Control. Release* **145**, 182–95 (2010).

88. Kafshgari, M. H., Harding, F. J. & Voelcker, N. H. Insights into Cellular Uptake of Nanoparticles. *Curr. Drug Deliv.* 63–77 (2015).

89. McMahon, H. T. & Boucrot, E. Molecular mechanism and physiological functions of clathrin-mediated endocytosis. *Nat. Rev. Mol. Cell Biol.* **12**, 517–533 (2011).

90. Lajoie, P. & Nabi, I. R. *Lipid rafts, caveolae, and their endocytosis*. *International Review of Cell and Molecular Biology* **282**, (Elsevier Inc., 2010).

91. Rothberg, K. G. *et al.* Caveolin, a protein component of caveolae membrane coats. *Cell* **68**, 673–682 (1992).

92. Rejman, J., Oberle, V., Zuhorn, I. S. & Hoekstra, D. Size-dependent internalization of particles via the pathways of clathrin- and caveolae-mediated endocytosis. *Biochem. J.* **377**, 159–169 (2004).

93. Oh, P., McIntosh, D. P. & Schnitzer, J. E. Dynamin at the Neck of Caveolae Mediates Their Budding to Form Transport Vesicles by GTP-driven Fission from the Plasma Membrane of Endothelium. *J. Cell Biol.* **141**, 101–114 (1998).

94. Mayor, S. & Pagano, R. E. Pathways of clathrin-independent endocytosis. *Nat. Rev. Mol. Cell Biol.* **8**, 603–12 (2007).

95. Torgersen, M. L., Skretting, G., van Deurs, B. & Sandvig, K. Internalization of cholera toxin by different endocytic mechanisms. *J. Cell Sci.* **114**, 3737–47 (2001).

96. Donaldson, J. G. Multiple roles for Arf6: sorting, structuring, and signaling at the plasma membrane. *J. Biol. Chem.* **278**, 41573–6 (2003).

97. Lundmark, R., Doherty, G. J., Vallis, Y., Peter, B. J. & Mcmahon, H. T. Arf family GTP loading is activated by, and generates, positive membrane curvature. *Biochem. J* **414**, 189–194 (2008).

98. Lundmark, R. *et al.* The GTPase-activating protein GRAF1 regulates the CLIC/GEEC endocytic pathway. *Curr. Biol.* **18**, (2008).

99. Marjoram, R. J., Lessey, E. C. & Burridge, K. Regulation of RhoA activity by adhesion molecules and mechanotransduction. *Curr. Mol. Med.* **14**, 199–208 (2014).

100. Lamaze, C. *et al.* Interleukin 2 Receptors and Detergent-Resistant Membrane Domains Define a Clathrin-Independent Endocytic Pathway. *Mol. Cell* **7**, 661–671 (2001).

101. De Duve, C., Pressman, B. C., Gianetto, R., Wattiaux, R. & Appelmans, F. Tissue fractionation studies. 6. Intracellular distribution patterns of enzymes in rat-liver tissue. *Biochem. J.* **60**, 604–17 (1955).

102. De Duve, C. *The lysosome turns fifty*. *Nature Cell Biology* **7**, (2005).

103. De Duve, C. *et al.* Lysosomotropic agents. *Biochem. Pharmacol.* **23**, (1974).

104. Markman, J. L., Rekechenetskiy, A., Holler, E. & Ljubimova, J. Y. Nanomedicine therapeutic approaches to overcome cancer drug resistance. *Adv. Drug Deliv. Rev.* **65**, 1866–79 (2013).

105. Srinivasarao, M., Galliford, C. V. & Low, P. S. Principles in the design of ligand-targeted cancer therapeutics and imaging agents. *Nat. Rev. Drug Discov.* **14**, 1–17 (2015).

106. Sahay, G., Kim, J. O., Kabanov, A. V. & Bronich, T. K. The exploitation of differential endocytic pathways in normal and tumor cells in the selective targeting of nanoparticulate chemotherapeutic agents. *Biomaterials* **31**, 923–933 (2010).

107. Gradishar, W. J. Albumin-bound paclitaxel: a next-generation taxane. *Expert Opin. Pharmacother.* **7**, 1041–1053 (2006).

108. Daniels, T. R., Delgado, T., Helguera, G. & Penichet, M. L. The transferrin receptor part II: Targeted delivery of therapeutic agents into cancer cells. *Clin. Immunol.* **121**, 159–176 (2006).

109. Steichen, S. D., Caldorera-Moore, M. & Peppas, N. A. A review of current nanoparticle and targeting moieties for the delivery of cancer therapeutics. *Eur. J. Pharm. Sci.* **48**, 416–427 (2013).

110. Duncan, R., Coatsworth, J. K. & Burtles, S. Preclinical toxicology of a novel polymeric antitumour agent: HPMA copolymerdoxorubicin (PK1). *Hum. Exp. Toxicol.* **17**, 93–104 (1998).

111. Venditto, V. J. & Szoka, F. C. Cancer nanomedicines: so many papers and so few drugs! *Adv. Drug Deliv. Rev.* **65**, 80–8 (2013).

112. Jain, R. K. & Stylianopoulos, T. Delivering nanomedicine to solid tumors. *Nat. Rev. Clin. Oncol.* **7**, 653–664 (2010).

113. Soo Choi, H. *et al.* Renal clearance of quantum dots. *Nat. Biotechnol.* **25**, 1165–1170 (2007).

114. Chithrani, B. D., Ghazani, A. A. & Chan, W. C. W. Determining the size and shape dependence of gold nanoparticle uptake into mammalian cells. *Nano Lett.* **6**, 662–668 (2006).

115. Yu, B. *et al.* Current status and future developments in preparation and application of nonspherical polymer particles. *Adv. Colloid Interface Sci.* **256**, 126–151 (2018).

116. Champion, J. A., Katare, Y. K. & Mitragotri, S. Making polymeric micro- and nanoparticles of complex shapes. *Proc. Natl. Acad. Sci.* **104**, 11901–11904 (2007).

117. Rolland, J. P. *et al.* Direct Fabrication and Harvesting of Monodisperse, Shape-Specific Nanobiomaterials. *J. Am. Chem. Soc.* **127**, 10096–10100 (2005).

118. Rolland, J. P., Hagberg, E. C., Denison, G. M., Carter, K. R. & De Simone, J. M. High-Resolution Soft Lithography: Enabling Materials for Nanotechnologies. *Angew. Chemie Int. Ed.* **43**, 5796–5799 (2004).

119. Gratton, S. E. *et al.* The effect of particle design on cellular internalization

pathways. *Proc. Natl. Acad. Sci. U. S. A.* **105**, 11613–11618 (2008).

120. Richards, D. M. & Endres, R. G. Target shape dependence in a simple model of receptor-mediated endocytosis and phagocytosis. *Proc. Natl. Acad. Sci.* **113**, 6113–6118 (2016).

121. Lee, S. Y., Ferrari, M. & Decuzzi, P. Design of bio-mimetic particles with enhanced vascular interaction. *J. Biomech.* **42**, 1885–1890 (2009).

122. Dalhaimer, P. *et al.* Shape effects of filaments versus spherical particles in flow and drug delivery. *Nat. Nanotechnol.* **2**, 249–255 (2007).

123. Min, Y., Akbulut, M., Kristiansen, K., Golan, Y. & Israelachvili, J. The role of interparticle and external forces in nanoparticle assembly. *Nat. Mater.* **7**, 527–538 (2008).

124. Gao, H., Shi, W. & Freund, L. B. Mechanics of receptor-mediated endocytosis. *Proc. Natl. Acad. Sci. U. S. A.* **102**, 9469–74 (2005).

125. He, C., Hu, Y., Yin, L., Tang, C. & Yin, C. Effects of particle size and surface charge on cellular uptake and biodistribution of polymeric nanoparticles. *Biomaterials* **31**, 3657–3666 (2010).

126. Slowing, I., Trewyn, B. G. & Lin, V. S.-Y. Effect of Surface Functionalization of MCM-41-Type Mesoporous Silica Nanoparticles on the Endocytosis by Human Cancer Cells. *J. Am. Chem. Soc.* **128**, 14792–14793 (2006).

127. Cedervall, T. *et al.* Understanding the nanoparticle-protein corona using methods to quantify exchange rates and affinities of proteins for nanoparticles.

Proc. Natl. Acad. Sci. **104**, 2050–2055 (2007).

128. Lundqvist, M. *et al.* Nanoparticle size and surface properties determine the protein corona with possible implications for biological impacts. *Proc. Natl. Acad. Sci. U. S. A.* **105**, 14265–70 (2008).

129. Nel, A. E. *et al.* Understanding biophysicochemical interactions at the nano-bio interface. *Nat. Mater.* **8**, 543–557 (2009).

130. Harris, J. M. & Chess, R. B. Effect of pegylation on pharmaceuticals. *Nat. Rev. Drug Discov.* **2**, 214–21 (2003).

131. Walkey, C. D., Olsen, J. B., Guo, H., Emili, A. & Chan, W. C. W. Nanoparticle Size and Surface Chemistry Determine Serum Protein Adsorption and Macrophage Uptake. *J. Am. Chem. Soc.* **134**, 2139–2147 (2012).

132. Walkey, C. D. & Chan, W. C. W. Understanding and controlling the interaction of nanomaterials with proteins in a physiological environment. *Chem. Soc. Rev.* **41**, 2780–2799 (2012).

133. Davis, F. F. *et al.* Enzyme-Polyethylene Glycol Adducts: Modified Enzymes with Unique Properties. in *Enzyme Engineering* 169–173 (Springer US, 1978). doi:10.1007/978-1-4684-6985-1_35

134. Chauhan, V. P. & Jain, R. K. Strategies for advancing cancer nanomedicine. *Nat. Mater.* **12**, (2013).

135. Meacham, C. E. & Morrison, S. J. Tumour heterogeneity and cancer cell plasticity. *Nature* **501**, 328–337 (2013).

136. Hanahan, D. & Weinberg, R. A. Hallmarks of cancer: the next generation. *Cell* **144**, 646–74 (2011).

137. Gerlinger, M. *et al.* Intratumor Heterogeneity and Branched Evolution Revealed by Multiregion Sequencing. *N. Engl. J. Med.* **366**, 883–892 (2012).

138. Dean, M., Fojo, T. & Bates, S. Tumour stem cells and drug resistance. *Nat. Rev. Cancer* **5**, 275–284 (2005).

139. Rosen, J. M. & Jordan, C. T. The Increasing Complexity of the Cancer Stem Cell Paradigm. *Science (80-.).* **324**, 1670–1673 (2009).

140. Trédan, O., Galmarini, C. M., Patel, K. & Tannock, I. F. Drug resistance and the solid tumor microenvironment. *J. Natl. Cancer Inst.* **99**, 1441–1454 (2007).

141. Lewis, C. E. & Pollard, J. W. Distinct role of macrophages in different tumor microenvironments. *Cancer Res.* **66**, 605–12 (2006).

142. Cassetta, L. & Pollard, J. W. Targeting macrophages: therapeutic approaches in cancer. *Nat. Rev. Drug Discov.* **17**, 887–904 (2018).

143. Lin, E. Y., Gouon-Evans, V., Nguyen, A. V. & Pollard, J. W. The Macrophage Growth Factor CSF-1 in Mammary Gland Development and Tumor Progression. *J. Mammary Gland Biol. Neoplasia* **7**, 147–162 (2002).

144. Su, S. *et al.* A Positive Feedback Loop between Mesenchymal-like Cancer Cells and Macrophages Is Essential to Breast Cancer Metastasis. *Cancer Cell* **25**, 605–620 (2014).

145. Casazza, A. *et al.* Impeding Macrophage Entry into Hypoxic Tumor Areas by Sema3A/Nrp1 Signaling Blockade Inhibits Angiogenesis and Restores Antitumor Immunity. *Cancer Cell* **24**, 695–709 (2013).

146. Noy, R. & Pollard, J. W. Tumor-Associated Macrophages: From Mechanisms to Therapy. *Immunity* **41**, 49–61 (2014).

147. Lin, E. Y. *et al.* Macrophages Regulate the Angiogenic Switch in a Mouse Model of Breast Cancer. *Cancer Res.* **66**, 11238–11246 (2006).

148. DeNardo, D. G. *et al.* CD4+ T Cells Regulate Pulmonary Metastasis of Mammary Carcinomas by Enhancing Protumor Properties of Macrophages. *Cancer Cell* **16**, 91–102 (2009).

149. Chanmee, T., Ontong, P., Konno, K. & Itano, N. Tumor-Associated Macrophages as Major Players in the Tumor Microenvironment. *Cancers (Basel).* **6**, 1670–1690 (2014).

150. Yang, J. *et al.* Tumor-associated macrophages regulate murine breast cancer stem cells through a novel paracrine EGFR/Stat3/Sox-2 signaling pathway. *Stem Cells* **31**, 248–58 (2013).

151. Paulus, P., Stanley, E. R., Schäfer, R., Abraham, D. & Aharinejad, S. Colony-Stimulating Factor-1 Antibody Reverses Chemoresistance in Human MCF-7 Breast Cancer Xenografts. *Cancer Res.* **66**, 4349–4356 (2006).

152. Mantovani, A., Polentarutti, N., Luini, W., Peri, G. & Spreafico, F. Role of host defense mechanisms in the antitumor activity of adriamycin and daunomycin in

mice. *J. Natl. Cancer Inst.* **63**, 61–6 (1979).

153. Kroemer, G., Galluzzi, L., Kepp, O. & Zitvogel, L. Immunogenic Cell Death in Cancer Therapy. *Annu. Rev. Immunol.* **31**, 51–72 (2013).

154. Singh, Y. *et al.* Targeting tumor associated macrophages (TAMs) via nanocarriers. *J. Control. Release* **254**, 92–106 (2017).

155. Heldin, C.-H., Rubin, K., Pietras, K. & Östman, A. High interstitial fluid pressure — an obstacle in cancer therapy. *Nat. Rev. Cancer* **4**, 806–813 (2004).

156. Chauhan, V. P. *et al.* Normalization of tumour blood vessels improves the delivery of nanomedicines in a size-dependent manner. *Nat. Nanotechnol.* **7**, 383–388 (2012).

157. Wei, S. C. *et al.* Matrix stiffness drives epithelial–mesenchymal transition and tumour metastasis through a TWIST1–G3BP2 mechanotransduction pathway. *Nat. Cell Biol.* **17**, 678–688 (2015).

158. Kumar, A., Placone, J. K. & Engler, A. J. Understanding the extracellular forces that determine cell fate and maintenance. *Development* **144**, 4261–4270 (2017).

159. Engler, A. J., Sen, S., Sweeney, H. L. & Discher, D. E. Matrix elasticity directs stem cell lineage specification. *Cell* **126**, 677–689 (2006).

160. Rehfeldt, F., Engler, A. J., Eckhardt, A., Ahmed, F. & Discher, D. E. Cell responses to the mechanochemical microenvironment-Implications for regenerative medicine and drug delivery. *Adv. Drug Deliv. Rev.* **59**, 1329–1339 (2007).

161. Swaminathan, V. & Waterman, C. M. The molecular clutch model for mechanotransduction evolves. *Nat. Cell Biol.* **18**, 459–61 (2016).

162. Matte, B. F. *et al.* Matrix stiffness mechanically conditions EMT and migratory behavior of oral squamous cell carcinoma. *J Cell Sci* **132**, jcs224360 (2019).

163. Teng, E. L. & Engler, A. J. Mechanical influences on cardiovascular differentiation and disease modeling. *Exp. Cell Res.* **377**, 103–108 (2019).

164. Kumar, A. *et al.* Mechanical activation of noncoding-RNA-mediated regulation of disease-associated phenotypes in human cardiomyocytes. *Nat. Biomed. Eng.* **3**, 137–146 (2019).

165. Zhou, Y. *et al.* Extracellular matrix in lung development, homeostasis and disease. *Matrix Biol.* **73**, 77–104 (2018).

166. Ondeck, M. G. *et al.* Dynamically stiffened matrix promotes malignant transformation of mammary epithelial cells via collective mechanical signaling. *Proc. Natl. Acad. Sci. U. S. A.* **116**, 3502–3507 (2019).

167. Acerbi, I. *et al.* Human breast cancer invasion and aggression correlates with ECM stiffening and immune cell infiltration. *Integr. Biol. (Camb).* **7**, 1120–34 (2015).

168. Thomas, K., Engler, A. J. & Meyer, G. A. Extracellular matrix regulation in the muscle satellite cell niche. *Connect. Tissue Res.* **56**, 1–8 (2015).

169. Johnson, K. R. *et al.* Tensional homeostasis and the malignant phenotype. *Cancer Cell* **8**, 241–254 (2005).

170. Lu, P., Weaver, V. M. & Werb, Z. The extracellular matrix: A dynamic niche in cancer progression. *J. Cell Biol.* **196**, 395–406 (2012).

171. Northey, J. J., Przybyla, L. & Weaver, V. M. Tissue Force Programs Cell Fate and Tumor Aggression. *Cancer Discov.* **7**, 1224–1237 (2017).

172. Butcher, D. T., Alliston, T. & Weaver, V. M. A tense situation: forcing tumour progression. *Nat. Rev. Cancer* **9**, 108–22 (2009).

173. Plodinec, M. *et al.* The nanomechanical signature of breast cancer. *Nat. Nanotechnol.* **7**, 757–65 (2012).

174. Levental, K. R. *et al.* Matrix Crosslinking Forces Tumor Progression by Enhancing Integrin Signaling. *Cell* **139**, 891–906 (2009).

175. Miroshnikova, Y. A. *et al.* Tissue mechanics promote IDH1-dependent HIF1α–tenascin C feedback to regulate glioblastoma aggression. *Nat. Cell Biol.* **18**, 1336–1345 (2016).

176. Krndija, D. *et al.* Substrate stiffness and the receptor-type tyrosine-protein phosphatase alpha regulate spreading of colon cancer cells through cytoskeletal contractility. *Oncogene* **29**, 2724–2738 (2010).

177. Missirlis, D. The effect of substrate elasticity and actomyosin contractility on different forms of endocytosis. *PLoS One* **9**, e96548 (2014).

178. Zhang, S., Gao, H. & Bao, G. Physical Principles of Nanoparticle Cellular Endocytosis. *ACS Nano* 8655–8671 (2015).

179. Huang, C. *et al.* Substrate stiffness regulates cellular uptake of nanoparticles. *Nano Lett.* **13**, 1611–5 (2013).

180. Soule, H. D., Vazquez, J., Long, A., Albert, S. & Brennan, M. A Human Cell Line From a Pleural Effusion Derived From a Breast Carcinoma. *J Natl Cancer Inst* **51**, 1409–1416 (1973).

181. Soule, H. D. *et al.* Isolation and characterization of a spontaneously immortalized human breast epithelial cell line, MCF-10. *Cancer Res.* **50**, 6075–86 (1990).

182. Cailleau, R., Young, R., Olivé, M. & Reeves, W. J. Breast tumor cell lines from pleural effusions. *J. Natl. Cancer Inst.* **53**, 661–74 (1974).

183. Raschke, W. C., Baird, S., Ralph, P. & Nakoinz, I. Functional macrophage cell lines transformed by abelson leukemia virus. *Cell* **15**, 261–267 (1978).

184. Saborano, R. *et al.* Metabolic Reprogramming of Macrophages Exposed to Silk, Poly(lactic-co-glycolic acid), and Silica Nanoparticles. *Adv. Healthc. Mater.* **6**, 1601240 (2017).

185. Sgouras, D. & Duncan, R. Methods for the evaluation of biocompatibility of soluble synthetic polymers which have potential for biomedical use: use of the tetrazolium-based colorimetric assay (MTT) as a preliminary screen for evaluation of in vitro cytotoxicity. *J. Mater. Sci. Mater. Med.* **1**, 61–68 (1990).

186. Misko, T. P., Schilling, R. J., Salvemini, D., Moore, W. M. & Currie, M. G. A Fluorometric Assay for the Measurement of Nitrite in Biological Samples.

Analytical Biochemistry **214**, 11–16 (1993).

187. Ridnour, L. A. *et al.* A spectrophotometric method for the direct detection and quantitation of nitric oxide, nitrite, and nitrate in cell culture media. *Anal. Biochem.* **281**, 223–229 (2000).

188. Schneider, C. A., Rasband, W. S. & Eliceiri, K. W. NIH Image to ImageJ: 25 years of image analysis. *Nat. Methods* **9**, 671–675 (2012).

189. Rowlands, A. S., George, P. A. & Cooper-White, J. J. Directing osteogenic and myogenic differentiation of MSCs: interplay of stiffness and adhesive ligand presentation. *Am. J. Physiol. Physiol.* **295**, C1037–C1044 (2008).

190. Totten, J. D., Wongpinyochit, T. & Seib, F. P. Silk nanoparticles: proof of lysosomotropic anticancer drug delivery at single-cell resolution. *J. Drug Target.* **25**, 865–872 (2017).

191. Trouet, A., Deprez-de Campeneere, D. & De Duve, C. Chemotherapy through lysosomes with a DNA-daunorubicin complex. *Nat. New Biol.* **239**, 110–2 (1972).

192. Dawidczyk, C. M. *et al.* State-of-the-art in design rules for drug delivery platforms: Lessons learned from FDA-approved nanomedicines. *J. Control. Release* **187**, 133–144 (2014).

193. Cheng, C. J., Tietjen, G. T., Saucier-Sawyer, J. K. & Saltzman, W. M. A holistic approach to targeting disease with polymeric nanoparticles. *Nat. Rev. Drug Discov.* **14**, 239–247 (2015).

194. Weiss, G. J. *et al.* First-in-human phase 1/2a trial of CRLX101, a cyclodextrin-containing polymer-camptothecin nanopharmaceutical in patients with advanced solid tumor malignancies. *Invest. New Drugs* **31**, 986–1000 (2013).

195. Wallace, A. M., Hoh, C. K., Vera, D. R., Darrah, D. D. & Schulteis, G. Lymphoseek: A Molecular Radiopharmaceutical for Sentinel Node Detection. *Ann. Surg. Oncol.* **10**, 531–538 (2003).

196. Gonzalez-Angulo, A. M. *et al.* Weekly nab-rapamycin in patients with advanced nonhematologic malignancies: Final results of a phase i trial. *Clin. Cancer Res.* **19**, 5474–5484 (2013).

197. Yucel, T., Lovett, M. L. & Kaplan, D. L. Silk-based biomaterials for sustained drug delivery. *J. Control. Release* **190**, 381–397 (2014).

198. Pritchard, E. M., Dennis, P. B., Omenetto, F., Naik, R. R. & Kaplan, D. L. Physical and chemical aspects of stabilization of compounds in silk. *Biopolymers* **97**, 479–498 (2012).

199. Gupta, V., Aseh, A., Ríos, C. N., Aggarwal, B. B. & Mathur, A. B. Fabrication and characterization of silk fibroin-derived curcumin nanoparticles for cancer therapy. *Int. J. Nanomedicine* **4**, 115–122 (2009).

200. Lammel, A. S., Hu, X., Park, S.-H., Kaplan, D. L. & Scheibel, T. R. Controlling silk fibroin particle features for drug delivery. *Biomaterials* **31**, 4583–91 (2010).

201. Wang, X., Yucel, T., Lu, Q., Hu, X. & Kaplan, D. L. Silk nanospheres and

microspheres from silk/pva blend films for drug delivery. *Biomaterials* **31**, 1025–1035 (2010).

202. Gholami, A., Tavanai, H. & Moradi, A. R. Production of fibroin nanopowder through electrospraying. *J. Nanoparticle Res.* **13**, 2089–2098 (2011).

203. Lu, Q. *et al.* Silk fibroin electrogelation mechanisms. *Acta Biomater.* **7**, 2394–2400 (2011).

204. Zhao, Z. *et al.* Formation of curcumin nanoparticles via solution-enhanced dispersion by supercritical CO2. *Int. J. Nanomedicine* **10**, 3171–81 (2015).

205. Lozano-Pérez, A. A. *et al.* Production of silk fibroin nanoparticles using ionic liquids and high-power ultrasounds. *J. Appl. Polym. Sci.* **132**, n/a-n/a (2014).

206. Zhang, Y.-Q. *et al.* Formation of silk fibroin nanoparticles in water-miscible organic solvent and their characterization. *J. Nanoparticle Res.* **9**, 885–900 (2007).

207. Kundu, J., Chung, Y.-I., Kim, Y. H., Tae, G. & Kundu, S. C. Silk fibroin nanoparticles for cellular uptake and control release. *Int. J. Pharm.* **388**, 242–250 (2010).

208. Pasut, G. & Veronese, F. M. The journey of a drug-carrier in the body: An anatomo-physiological perspective. *J. Control. Release* **161**, 461–472 (2012).

209. Stoka, V., Turk, B. & Turk, V. Lysosomal Cysteine Proteases: Structural Features and their Role in Apoptosis. *IUBMB Life (International Union Biochem. Mol. Biol. Life)* **57**, 347–353 (2005).

210. Turk, B., Turk, V. & Turk, D. Structural and functional aspects of papain-like cysteine proteinases and their protein inhibitors. *Biol. Chem.* **378**, 141–50 (1997).

211. Seglen, P. O., Grinde, B. & Solheim, A. E. Inhibition of the lysosomal pathway of protein degradation in isolated rat hepatocytes by ammonia, methylamine, chloroquine and leupeptin. *Eur. J. Biochem.* **95**, 215–25 (1979).

212. Millot, C., Millot, J. M., Morjani, H., Desplaces, a & Manfait, M. Characterization of acidic vesicles in multidrug-resistant and sensitive cancer cells by acridine orange staining and confocal microspectrofluorometry. *J. Histochem. Cytochem.* **45**, 1255–1264 (1997).

213. Katayama, H., Issiki, M. & Yoshitomi, H. Application of fibroin in controlled release tablets containing theophylline. *Biol. Pharm. Bull.* **23**, 1229–34 (2000).

214. Seib, F. P., Pritchard, E. M. & Kaplan, D. L. Self-assembling doxorubicin silk hydrogels for the focal treatment of primary breast cancer. *Adv. Funct. Mater.* **23**, 58–65 (2013).

215. Vepari, C. & Kaplan, D. L. Silk as a Biomaterial. *Prog. Polym. Sci.* **32**, 991 (2007).

216. Seib, F. P. *et al.* Focal therapy of neuroblastoma using silk films to deliver kinase and chemotherapeutic agents in vivo. *Acta Biomater.* **20**, 32–38 (2015).

217. Jewell, M., Daunch, W., Bengtson, B. & Mortarino, E. The development of SERI Surgical Scaffold, an engineered biological scaffold. *Ann. N. Y. Acad. Sci.*

1358, 44–55 (2015).

218. Tian, Y., Jiang, X., Chen, X., Shao, Z. & Yang, W. Doxorubicin-Loaded Magnetic Silk Fibroin Nanoparticles for Targeted Therapy of Multidrug-Resistant Cancer. *Adv. Mater.* **26**, 7393–7398 (2014).

219. Liu, J. *et al.* Safe and Effective Reversal of Cancer Multidrug Resistance Using Sericin-Coated Mesoporous Silica Nanoparticles for Lysosome-Targeting Delivery in Mice. *Small* **13**, 1602567 (2017).

220. Lloyd, J. B. Lysosome membrane permeability: implications for drug delivery. *Adv. Drug Deliv. Rev.* **41**, 189–200 (2000).

221. Simon, S., Roy, D. & Schindler, M. Intracellular pH and the control of multidrug resistance. *Proc. Natl. Acad. Sci. U. S. A.* **91**, 1128–32 (1994).

222. Ohkuma, S. & Poole, B. Fluorescence probe measurement of the intralysosomal pH in living cells and the perturbation of pH by various agents. *Cell Biol.* **75**, 3327–31 (1978).

223. Totten, J. D., Wongpinyochit, T., Carrola, J., Duarte, I. F. & Seib, F. P. PEGylation-Dependent Metabolic Rewiring of Macrophages with Silk Fibroin Nanoparticles. *ACS Appl. Mater. Interfaces* **11**, 14515–14525 (2019).

224. Yao, V. J. *et al.* Ligand-targeted theranostic nanomedicines against cancer. *J. Control. Release* **240**, 267–286 (2016).

225. Shi, J., Kantoff, P. W., Wooster, R. & Farokhzad, O. C. Cancer nanomedicine: progress, challenges and opportunities. *Nat. Rev. Cancer* **17**, 20–37 (2016).

226. Tenzer, S. *et al.* Rapid formation of plasma protein corona critically affects nanoparticle pathophysiology. *Nat. Nanotechnol.* **8**, (2013).

227. Mosser, D. M. & Edwards, J. P. Exploring the full spectrum of macrophage activation. *Nat. Rev. Immunol.* **8**, 958–69 (2008).

228. Dobrovolskaia, M. A., McNeil, S. E. & Neil, S. E. M. Immunological properties of engineered nanomaterials. *Nat. Nanotechnol.* **2**, 469–78 (2007).

229. Wolfram, J. *et al.* Safety of Nanoparticles in Medicine. *Curr. Drug Targets* **16**, 1671–81 (2015).

230. Bitar, A., Ahmad, N. M., Fessi, H. & Elaissari, A. Silica-based nanoparticles for biomedical applications. *Drug Discov. Today* **17**, 1147–1154 (2012).

231. Sharma, S., Parmar, A., Kori, S. & Sandhir, R. PLGA-based nanoparticles: A new paradigm in biomedical applications. *TrAC Trends Anal. Chem.* **80**, 30–40 (2016).

232. Hu, X., Kaplan, D. & Cebe, P. Determining beta-sheet crystallinity in fibrous proteins by thermal analysis and infrared spectroscopy. *Macromolecules* **39**, 6161–6170 (2006).

233. Manders, E. M. M., Verbeek, F. J. & Aten, J. A. Measurement of co-localization of objects in dual-colour confocal images. *J. Microsc.* **169**, 375–382 (1993).

234. Dunn, K. W., Kamocka, M. M. & McDonald, J. H. A practical guide to evaluating colocalization in biological microscopy. *AJP Cell Physiol.* **300**, C723–C742 (2011).

235. Berben, L., Sereika, S. M. & Engberg, S. Effect size estimation: Methods and examples. *Int. J. Nurs. Stud.* **49**, 1039–1047 (2012).

236. Strelko, C. L. *et al.* Itaconic Acid Is a Mammalian Metabolite Induced during Macrophage Activation. *J. Am. Chem. Soc.* **133**, 16386–16389 (2011).

237. Meiser, J. *et al.* Pro-inflammatory Macrophages Sustain Pyruvate Oxidation through Pyruvate Dehydrogenase for the Synthesis of Itaconate and to Enable Cytokine Expression. *J. Biol. Chem.* **291**, 3932–46 (2016).

238. Mantovani, A., Sozzani, S., Locati, M., Allavena, P. & Sica, A. Macrophage polarization: tumor-associated macrophages as a paradigm for polarized M2 mononuclear phagocytes. *Trends Immunol.* **23**, 549–555 (2002).

239. De Palma, M. & Lewis, C. E. Macrophage regulation of tumor responses to anticancer therapies. *Cancer Cell* **23**, 277–286 (2013).

240. Zhang, Q. *et al.* Prognostic Significance of Tumor-Associated Macrophages in Solid Tumor: A Meta-Analysis of the Literature. *PLoS One* **7**, e50946 (2012).

241. Mantovani, A., Marchesi, F., Malesci, A., Laghi, L. & Allavena, P. Tumour-associated macrophages as treatment targets in oncology. *Nat. Rev. Clin. Oncol.* **14**, 399 (2017).

242. Ostuni, R., Kratochvill, F., Murray, P. J. & Natoli, G. Macrophages and cancer: From mechanisms to therapeutic implications. *Trends Immunol.* **36**, 229–239 (2015).

243. Ngambenjawong, C., Gustafson, H. H. & Pun, S. H. Progress in tumor-

associated macrophage (TAM)-targeted therapeutics. *Adv. Drug Deliv. Rev.* **114**, 206–221 (2017).

244. Freedman, A. S., Freeman, G. J., Rhynhart, K. & Nadler, L. M. Selective induction of B7/BB-1 on interferon-γ stimulated monocytes: A potential mechanism for amplification of T cell activation through the CD28 pathway. *Cell. Immunol.* **137**, 429–437 (1991).

245. Kuchroo, V. K. *et al.* B7-1 and B7-2 costimulatory molecules activate differentially the Th1/Th2 developmental pathways: Application to autoimmune disease therapy. *Cell* **80**, 707–718 (1995).

246. Mantovani, A. *et al.* The chemokine system in diverse forms of macrophage activation and polarization. *Trends Immunol.* **25**, 677–86 (2004).

247. Murray, P. J. *et al.* Macrophage Activation and Polarization: Nomenclature and Experimental Guidelines. *Immunity* **41**, 14–20 (2014).

248. Rabanel, J. M., Hildgen, P. & Banquy, X. Assessment of PEG on polymeric particles surface, a key step in drug carrier translation. *J. Control. Release* **185**, 71–87 (2014).

249. Maitz, M. F. *et al.* Biocompatibility assessment of silk nanoparticles: hemocompatibility and internalization by human blood cells. *Nanomedicine Nanotechnology, Biol. Med.* **13**, 2633–2642 (2017).

250. Griffin, G. K. *et al.* IL-17 and TNF-α sustain neutrophil recruitment during inflammation through synergistic effects on endothelial activation. *J. Immunol.*

188, 6287–99 (2012).

251. Bogdan, C. Nitric oxide synthase in innate and adaptive immunity: An update. *Trends Immunol.* **36**, 161–178 (2015).

252. MacMicking, J., Xie, Q. & Nathan, C. Nitric Oxide and Macrophage Function. *Annu. Rev. Immunol.* **15**, 323–350 (1997).

253. Zhang, Y. *et al.* ROS play a critical role in the differentiation of alternatively activated macrophages and the occurrence of tumor-associated macrophages. *Cell Res.* **23**, 898 (2013).

254. Van den Bossche, J., O'Neill, L. A. & Menon, D. Macrophage Immunometabolism: Where Are We (Going)? *Trends Immunol.* **38**, 395–406 (2017).

255. Rodríguez-Prados, J.-C. *et al.* Substrate fate in activated macrophages: a comparison between innate, classic, and alternative activation. *J. Immunol.* **185**, 605–14 (2010).

256. Jha, A. K. *et al.* Network Integration of Parallel Metabolic and Transcriptional Data Reveals Metabolic Modules that Regulate Macrophage Polarization. *Immunity* **42**, 419–430 (2015).

257. Ryan, D. G. & O'Neill, L. A. J. Krebs cycle rewired for macrophage and dendritic cell effector functions. *FEBS Lett.* **591**, 2992–3006 (2017).

258. Tannahill, G. M. *et al.* Succinate is an inflammatory signal that induces IL-1β through HIF-1α. *Nature* **496**, 238–242 (2013).

259. Mills, E. L. *et al.* Succinate Dehydrogenase Supports Metabolic Repurposing of Mitochondria to Drive Inflammatory Macrophages. *Cell* **167**, 457-470.e13 (2016).

260. Michelucci, A. *et al.* Immune-responsive gene 1 protein links metabolism to immunity by catalyzing itaconic acid production. *Proc. Natl. Acad. Sci. U. S. A.* **110**, 7820–5 (2013).

261. Cordes, T. *et al.* Immunoresponsive Gene 1 and Itaconate Inhibit Succinate Dehydrogenase to Modulate Intracellular Succinate Levels. *J. Biol. Chem.* **291**, 14274–84 (2016).

262. Lampropoulou, V. *et al.* Itaconate Links Inhibition of Succinate Dehydrogenase with Macrophage Metabolic Remodeling and Regulation of Inflammation. *Cell Metab.* **24**, 158–166 (2016).

263. Mills, E. L. *et al.* Itaconate is an anti-inflammatory metabolite that activates Nrf2 via alkylation of KEAP1. *Nature* **556**, 113–117 (2018).

264. Schieber, M. & Chandel, N. S. ROS function in redox signaling and oxidative stress. *Curr. Biol.* **24**, R453–R462 (2014).

265. EL Kasmi, K. C. & Stenmark, K. R. Contribution of metabolic reprogramming to macrophage plasticity and function. *Semin. Immunol.* **27**, 267–275 (2015).

266. Németh, B. *et al.* Abolition of mitochondrial substrate-level phosphorylation by itaconic acid produced by LPS-induced Irg1 expression in cells of murine macrophage lineage. *FASEB J.* **30**, 286–300 (2016).

267. Loike, J. D., Somes, M. & Silverstein, S. C. Creatine uptake, metabolism, and efflux in human monocytes and macrophages. *Am J Physiol* **251**, C128-35 (1986).

268. Marcinkiewicz, J., Grabowska, A., Bereta, J. & Stelmaszynska, T. Taurine chloramine, a product of activated neutrophils, inhibits in vitro the generation of nitric oxide and other macrophage inflammatory mediators. *J. Leukoc. Biol.* **58**, 667–674 (1995).

269. Murray, P. J. & Wynn, T. A. Protective and pathogenic functions of macrophage subsets. *Nat. Rev. Immunol.* **11**, 723–737 (2011).

270. Vonarbourg, A., Passirani, C., Saulnier, P. & Benoit, J. P. Parameters influencing the stealthiness of colloidal drug delivery systems. *Biomaterials* **27**, 4356–4373 (2006).

271. Argaw, A. *et al.* Effect of mechanical properties of hydrogel nanoparticles on macrophage cell uptake. *Soft Matter* **5**, 3984 (2009).

272. Mosesson, Y., Mills, G. B. & Yarden, Y. Derailed endocytosis: an emerging feature of cancer. *Nat. Rev. Cancer* **8**, 835–850 (2008).

273. Lu, Z., Ghosh, S., Wang, Z. & Hunter, T. Downregulation of caveolin-1 function by EGF leads to the loss of E-cadherin , increased transcriptional activity of ␣ -catenin , and enhanced tumor cell invasion. **4**, 499–515 (2003).

274. Ezratty, E. J., Bertaux, C., Marcantonio, E. E. & Gundersen, G. G. Clathrin mediates integrin endocytosis for focal adhesion disassembly in migrating cells.

J. Cell Biol. **187**, 733–747 (2009).

275. Morishige, M. *et al.* GEP100 links epidermal growth factor receptor signalling to Arf6 activation to induce breast cancer invasion. *Nat. Cell Biol.* **10**, 85–92 (2008).

276. Rizwan, A. *et al.* Breast cancer cell adhesome and degradome interact to drive metastasis. *npj Breast Cancer* **1**, 15017 (2015).

277. Reis, C. R. *et al.* Crosstalk between Akt/GSK3 signaling and dynamin-1 regulates clathrin-mediated endocytosis. *EMBO J.* **34**, 2132–2146 (2015).

278. Xiao, G.-Y., Mohanakrishnan, A. & Schmid, S. L. Role for ERK1/2-dependent activation of FCHSD2 in cancer cell-selective regulation of clathrin-mediated endocytosis. *Proc. Natl. Acad. Sci.* **115**, E9570–E9579 (2018).

279. Kim, J. A., Åberg, C., Salvati, A. & Dawson, K. A. Role of cell cycle on the cellular uptake and dilution of nanoparticles in a cell population. *Nat. Nanotechnol.* **7**, 62–68 (2011).

280. Brownlee, W. J. & Seib, F. P. Impact of the hypoxic phenotype on the uptake and efflux of nanoparticles by human breast cancer cells. *Sci. Rep.* **8**, 1–11 (2018).

281. Panzetta, V. *et al.* ECM Mechano-Sensing Regulates Cytoskeleton Assembly and Receptor-Mediated Endocytosis of Nanoparticles. *ACS Biomater. Sci. Eng.* **3**, 1586–1594 (2017).

282. O'Brien, J., Wilson, I., Orton, T. & Pognan, F. Investigation of the Alamar Blue

(resazurin) fluorescent dye for the assessment of mammalian cell cytotoxicity. *Eur. J. Biochem.* **267**, 5421–5426 (2000).

283. Kirchhausen, T., Macia, E. & Pelish, H. E. Use of Dynasore, the Small Molecule Inhibitor of Dynamin, in the Regulation of Endocytosis. *Methods Enzymol.* **438**, 77–93 (2008).

284. Cheng, Y. *et al.* Structure of the Human Transferrin Receptor-Transferrin Complex. *Cell* **116**, 565–576 (2004).

285. Macia, E. *et al.* Dynasore, a Cell-Permeable Inhibitor of Dynamin. *Dev. Cell* **10**, 839–850 (2006).

286. Al Soraj, M. *et al.* siRNA and pharmacological inhibition of endocytic pathways to characterize the differential role of macropinocytosis and the actin cytoskeleton on cellular uptake of dextran and cationic cell penetrating peptides octaarginine (R8) and HIV-Tat. *J. Control. Release* **161**, 132–141 (2012).

287. Motley, A., Bright, N. A., Seaman, M. N. J. & Robinson, M. S. Clathrin-mediated endocytosis in AP-2–depleted cells. *J. Cell Biol.* **162**, 909–918 (2003).

288. Hinrichsen, L., Harborth, J., Andrees, L., Weber, K. & Ungewickell, E. J. Effect of Clathrin Heavy Chain- and α-Adaptin-specific Small Inhibitory RNAs on Endocytic Accessory Proteins and Receptor Trafficking in HeLa Cells. *J. Biol. Chem.* **278**, 45160–45170 (2003).

289. Chiba, M., Kubota, S., Sato, K. & Monzen, S. Exosomes released from

pancreatic cancer cells enhance angiogenic activities via dynamin-dependent endocytosis in endothelial cells in vitro. *Sci. Rep.* **8**, 1–9 (2018).

290. Sasso, L., Purdie, L., Grabowska, A., Jones, A. T. & Alexander, C. Time and cell-dependent effects of endocytosis inhibitors on the internalization of biomolecule markers and nanomaterials. *J. Interdiscip. Nanomedicine* **3**, 67–81 (2018).

291. McMahon, H. T. & Boucrot, E. Membrane curvature at a glance. *J. Cell Sci.* **128**, 1065–1070 (2015).

292. Dutta, D. & Donaldson, J. G. Search for inhibitors of endocytosis: Intended specificity and unintended consequences. *Cell. Logist.* **2**, 203–208 (2012).

293. Jimah, J. R. & Hinshaw, J. E. Structural Insights into the Mechanism of Dynamin Superfamily Proteins. *Trends Cell Biol.* **29**, 257–273 (2019).

294. Preta, G., Cronin, J. G. & Sheldon, I. M. Dynasore - not just a dynamin inhibitor. *Cell Commun. Signal.* **13**, 24 (2015).

295. Royle, S. J., Bright, N. A. & Lagnado, L. Clathrin is required for the function of the mitotic spindle. *Nature* **434**, 1152–1157 (2005).

296. Kim, M. L., Sorg, I. & Arrieumerlou, C. C. Endocytosis - Independent Function of Clathrin Heavy Chain in the Control of Basal NF - kB Activation. *PLoS One* **6**, (2011).

297. Totta, P., Pesiri, V., Enari, M., Marino, M. & Acconcia, F. Clathrin Heavy Chain Interacts With Estrogen Receptor α and Modulates 17β-Estradiol

Signaling. *Mol. Endocrinol.* **29**, 739–755 (2015).

298. Boucrot, E. & Kirchhausen, T. Endosomal recycling controls plasma membrane area during mitosis. *Proc. Natl. Acad. Sci. U. S. A.* **104**, 7939–7944 (2007).

299. Raucher, D. & Sheetz, M. P. Membrane expansion increases endocytosis rate during mitosis. *J. Cell Biol.* **144**, 497–506 (1999).

300. Schweitzer, J. K., Burke, E. E., Goodson, H. V. & D'Souza-Schorey, C. Endocytosis resumes during late mitosis and is required for cytokinesis. *J. Biol. Chem.* **280**, 41628–41635 (2005).

301. Glukhova, M. A. & Streuli, C. H. How integrins control breast biology. *Curr. Opin. Cell Biol.* **25**, 633–641 (2013).

302. Spill, F., Reynolds, D. S., Kamm, R. D. & Zaman, M. H. Impact of the physical microenvironment on tumor progression and metastasis. *Curr. Opin. Biotechnol.* **40**, 41–48 (2016).

303. Wang, Y., Gong, T., Zhang, Z.-R. & Fu, Y. Matrix Stiffness Differentially Regulates Cellular Uptake Behavior of Nanoparticles in Two Breast Cancer Cell Lines. *ACS Appl. Mater. Interfaces* **9**, 25915–25928 (2017).

304. Vercauteren, D. *et al.* The Use of Inhibitors to Study Endocytic Pathways of Gene Carriers: Optimization and Pitfalls. *Mol. Ther.* **18**, 561–569 (2010).

305. Wongpinyochit, T., Totten, J. D., Johnston, B. F. & Seib, F. P. Microfluidic-assisted silk nanoparticle tuning. *Nanoscale Adv.* **1**, 873–883 (2019).

306. Kocatürk, B. & Versteeg, H. H. Orthotopic Injection of Breast Cancer Cells into the Mammary Fat Pad of Mice to Study Tumor Growth. *J. Vis. Exp* **96**, 51967 (2015).

Appendix A

Abstract accepted for oral presentation at the 2017 UKICRS symposium, Glasgow UK

SILK NANOPARTICLES ARE ENDOCYTOSED BY LIVE BREAST CANCER CELLS AND FACILITATE LYSOSOMOTROPIC DELIVERY OF AN ANTICANCER DRUG.
John D. Totten [1], Thidarat Wongpinyochit[1], F. Philipp Seib[1]
[1] Strathclyde Institute of Pharmacy and Biomedical Sciences, University of Strathclyde, 161 Cathedral Street, Glasgow, G4 0RE, UK
Background: Silk nanoparticles (SNPs) are expected to improve chemotherapeutic drug targeting to solid tumours by exploiting tumour pathophysiology, modifying the cellular pharmacokinetics of the payload and ultimately trafficking to lysosomes to trigger drug release. However, experimental proof for lysosomotropic drug delivery by SNPs in live cells is lacking and the importance of lysosomal pH and enzymes controlling drug release are currently unknown. Here, we demonstrate, in live single human breast cancer cells, the role of the lysosomal environment in determining SNP-mediated drug release.
Methods: *Bombyx mori* silk cocoons were reverse engineered and the resulting aqueous silk solution was subjected to desolvation to generate SNPs. Half of the batch was surface modified with polyethylene glycol (PEG) and surface characterization of native and PEGylated SNPs was conducted by dynamic light scattering (DLS) using a Zetasizer Nano-ZS (Malvern Instrument, U.K.). Native and PEGylated SNPs were conjugated to Alexa Fluor® 488 (AF488) (Thermo Fisher Scientific, USA) or loaded with 0.3 μg/ml doxorubicin for use in cell-based studies. MCF-7 human breast cancer cells were cultured in complete DMEM (4.5 g glucose, 110 mg sodium pyruvate, 10%v/v FBS, and 10 μg/ mL insulin) and subcultured every 2–3 days. For all analyses, cells were seeded at a density of 2×10^4 cells/cm^2 and allowed to recover for 24 h. To verify that native and PEGylated SNPs traffic to lysosomes, cells were dosed with 0.5 mg/ml AF488-conjugated particles for 5 h in the presence of 50 nM Lysotracker® Red (Thermo Fisher Scientific, USA). Live confocal microscopy was conducted immediately afterwards on a Leica TCS-SP5 confocal laser scanning microscope (Leica Microsystems GmbH, Germany) to verify lysosomal localisation. Changes in total cell-associated fluorescence of cells were measured by flow cytometry using a BD FACSCanto (Becton Dickinson, USA) immediately after dosing. Lysosomotropic drug delivery was assessed by inhibiting lysosomal acidification or enzymatic degradation with 10 mM ammonium chloride (NH_4Cl) (Sigma-Aldrich, U.S.A) or 10 mM leupeptin (Sigma-Aldrich, U.S.A) and dosing cells for 5 h with doxorubicin loaded native or PEGylated SNPs. A combination inhibition was also conducted. Confocal microscopy was used to verify nuclear translocation of doxorubicin to the cell nucleus and quantify differences in doxorubicin-associated nuclear fluorescence following inhibition of lysosomal acidification and enzymatic degradation.
Results: Native SNPs were of uniform particle size (98.49 ± 3.7 nm; 0.095 polydispersity) and had a negative surface charge (-42.60 ± 0.72 mV). PEGylation resulted in an increase in particle size (105.30 ± 3.6 nm; 0.087 polydispersity) and reduced the negative charge (−36.77 ± 0.80). MCF-7 cells endocytosed and trafficked drug-loaded native and PEGylated SNPs to lysosomes, with subsequent drug release from the respective carriers and nuclear translocation within 5 h of dosing. A combination of low pH and enzymatic degradation facilitated drug release from SNPs; perturbation of the acidic lysosomal pH and inhibition of serine, cysteine and threonine proteases resulted in 42% and 33% reductions in nuclear-associated drug accumulation from native and PEGylated SNPs, respectively.
Conclusions: This study demonstrates the importance of lysosomal activity for anticancer drug release from SNPs, thereby providing direct evidence for lysosomotropic drug delivery in live single cells.

Appendix B

Abstract accepted for poster presentation at the 2018 ISPT conference in Valencia, Spain.

SILK NANOPARTICLES: LYSOSOMOTROPIC DRUG DELIVERY AND METABOLIC REPROGRAMMING AT THE TUMOUR MICROENVIRONMENT.

John D. Totten[1], Thidarat Wongpinyochit[1], Raquel Saborano[2], Iola Duarte[2], F. Philipp Seib[1]
[1] Strathclyde Institute of Pharmacy and Biomedical Sciences, University of Strathclyde, 161 Cathedral Street, Glasgow, G4 0RE, UK. [2] CICECO – Aveiro Institute of Materials, Department of Chemistry, University of Aveiro, 3810-193 Aveiro, Portugal.

INTRODUCTION

Therapeutic targeting of the tumour microenvironment with nanoparticles is appealing but requires a wider biological assessment. For example, nanomedicines designed for intracellular drug release are able to overcome drug resistance mechanisms but are thus dependent on endocytic uptake and correct intracellular routing to achieve the desired pharmacological effect.[1] Furthermore, nanoparticles are internalised by cancer-associated cells that can in turn regulate tumour growth. However, the interactions between nanoparticles and non-tumour cells are often overlooked. Silk is a promising biopolymer for drug delivery because it can be processed into nanoparticles to stabilise and protect therapeutic payloads.[70] In addition, proteolysis of the silk carrier is less likely to disrupt lysosomal function during intracellular trafficking.[68] Therefore the aim of the present study was to examine (i) the impact of lysosomal enzymes on drug release from silk nanoparticles (SNPs) and (ii) the phenotypic and metabolomic responses of tumour-associated macrophages towards SNPs.

RESULTS AND DISCUSSION

Native and PEGylated SNPs were of uniform particle size (98.49 ± 3.7 nm and 105.30 ± 3.6 nm, respectively) and negative surface charge (-42.60 ± 0.72 mV and −36.77 ± 0.80, respectively). Both human breast epithelial cells (MCF-7) and macrophages (RAW264.7) endocytosed and trafficked drug-loaded native and PEGylated SNPs to lysosomes. Lysosomotropic anticancer drug delivery in MCF-7 cells was determined by measuring drug-associated fluorescence within the target site (i.e. nucleus) of single cells. Perturbation of lysosomal acidity and inhibition of lysosomal serine, cysteine and threonine proteases resulted in 42% and 33% reductions in nuclear-associated drug accumulation from native and PEGylated SNPs, respectively.[190] Next, downstream phenotypic and metabolic effects of SNP endocytosis and degradation were measured in macrophages. Macrophages displayed an increased expression of M1-like phenotype including elevated TNF-α and nitric oxide release. This was accompanied by a metabolic shift that included increased glycolytic activity, an altered tricarboxylic acid cycle and reduced ATP generation. Both phenotypic and metabolic changes were found to be significantly milder when macrophages were treated with PEGylated SNPs than native SNPs. In summary, we demonstrate that SNPs (i) mediate lysosomotropic anticancer delivery in metastatic breast cancer cells and (ii) drive phenotypic shifts in macrophages to a more M1-like state which are accompanied by metabolomic reprogramming.

REFERENCES

1. Duncan, R. & Richardson, S. C. W. Endocytosis and intracellular trafficking as gateways for nanomedicine delivery: Opportunities and challenges. Mol. Pharm. 9, 2380–2402 (2012).
2. Wongpinyochit, T., Johnston, B. F. & Seib, F. P. Manufacture and Drug Delivery Applications of Silk Nanoparticles. J. Vis. Exp. e54669–e54669 (2016). doi:10.3791/54669
3. Seib, F. P. Silk nanoparticles—an emerging anticancer nanomedicine. AIMS Bioeng. 4, 239–258 (2017).
4. Totten, J. D., Wongpinyochit, T. & Seib, F. P. Silk nanoparticles: proof of lysosomotropic anticancer drug delivery at single-cell resolution. J. Drug Target. 25, 865-872 (2017).

Appendix C

Abstract accepted for poster presentation at the 2019 Bio-nanomaterials conference in Glasgow, UK.

Attenuation of macrophage activation state with silk nanoparticles.

John D. Totten,a* Thidarat Wongpinyochit, Joana Carrolab, Iola F. Duarteb, F. Philipp Seiba*

a SIPBS, University of Strathclyde, 161 Cathedral Street, Glasgow, G4 0RE, UK.
b CICECO – Aveiro Institute of Materials, University of Aveiro, 3810-193 Aveiro, Portugal.
Corresponding author email: philipp.seib@strath.ac.uk

Abstract
Silk nanoparticles are emerging as promising nanomedicines for anticancer treatment1 and can be readily PEGylated to improve colloidal stability and tune degradation and drug release profiles.2 We recently revealed that unmodified silk nanoparticles can drive metabolic reprogramming of macrophages3. However, the extent of these interactions have yet to be fully elucidated. Here, we used a combination of *in vitro* assays and nuclear magnetic resonance (NMR)-based metabolomics to examine the inflammatory phenotype and metabolic profiles of macrophages following exposure to unmodified or PEGylated silk nanoparticles. Unmodified silk fibroin nanoparticles induced upregulation of inflammatory mediators such as cytokines, nitric oxide release and antioxidant activity. This was accompanied by changes to their metabolomic profiles that were consistent with a proinflammatory state, including increased glycolysis and reprogramming of the tricarboxylic acid cycle and creatine kinase/phosphocreatine pathway. By contrast, milder changes to macrophage activation state were observed following exposure to PEGylated silk nanoparticles, suggesting that the immunomodulation was a PEGylation-dependent process. This could be especially useful in the context of anticancer drug delivery, where silk nanoparticles could not only act as carriers for chemotherapeutics, but also synergistically attenuate tumour-associated macrophages towards a more tumoricidal state.

References
1. Totten, J. D.; Wongpinyochit, T.; Seib, F. P. Silk Nanoparticles: Proof of Lysosomotropic Anticancer Drug Delivery at Single-Cell Resolution. J. Drug Target. 2017, 25 (9–10), 865–872.
2. Wongpinyochit, T.; Johnston, B. F.; Seib, F. P. Degradation Behavior of Silk Nanoparticles - Enzyme Responsiveness. ACS Biomater. Sci. Eng. 2018, 4 (3), 942–951.
3. Saborano, R. et al. Metabolic Reprogramming of Macrophages Exposed to Silk, Poly(Lactic-Co-Glycolic Acid), and Silica Nanoparticles. Adv. Healthc. Mater. 2017, 6 (14), 1601240.